# Short-range Forecasting Research

## GLOBAL PRECIPITATION CLIMATOLOGY PROJECT
## ALGORITHM INTERCOMPARISON PROJECT - 2
## REPORT No. 1

## GPCP-AIP/2 - ATLAS: METEOSAT DATA

by

G.L. Liberti

July 1992

Meteorological Office
London Road
Bracknell
Berkshire
RG12 2SZ
United Kingdom

# GPCP-AIP/2 - ATLAS: METEOSAT DATA.

*G.L.Liberti**
Meteorological Office,Bracknell, UK

30 th July 1992

## Introduction

As part of the Global Precipitation Climatology Project - Algorithm Intercomparison Project - 2 (GPCP-AIP/2) (WMO, 1989) data from the three channels (Infrared ($10.5 - 12.5\mu$m) [IR], Visible ($0.5 - 0.9\mu$m) [VIS] and Water Vapour ($5.7 - 7.1\mu$m) [WV]) Meteosat radiometer were collected on a hourly basis, for the period $1^{st}$ February to $9^{th}$ April 1991, covering the area shown in Figure 10.
Statistical analyses were carried out on the data set in order to:
- test the quality of the data;
- study the statistical properties of the data;
- help select interesting cases from the point of view of estimating precipitation;
- compare with similar analyses of data sets from other instruments during the GPCP-AIP/2 Campaign.
This report shows the results of such an analyses.
Apart from a very few seriously contaminated images, all the imagery constituting the data set as distributed to the GPCP-AIP/2 participants have been analysed. Some more rigorous criteria discriminating low quality data can be suggested (see Section 3) but have not been applied at this stage, to give users maximum flexibility to process the data.

The data origin and preprocessing are described in Section 1.
Section 2 describes the analyses applied to the data set.
In Section 3 some comments on the data set are reported.

## 1 Data Origin and Preprocessing

Most of Meteosat imagery data were obtained in real-time during the campaign using the UK Meteorological Office's dedicated satellite image processing system, Autosat-2 (Allam et al., 1990). Additional imagery data from ESOC and the UK Met. Office were required to improve the availability of the imagery especially during the first part of the campaign. Nevertheless $\sim$ 87% of the imagery are from Autosat-2; these can be easily identified by the presence of bands of "missing data" values (see below).
The preprocessing (Navigation, Calibration, Rescaling) for both Autosat-2 and imagery from other sources are described below.
The final products are in the form of digital imagery of 300 lines x 360 pixels. The pixel size is 5x5 Km, whereas the original resolution was approximately 8x5 km and 4x2.5 km respectively for IR and VIS in the southern part of the image.
The digitization interval is 0.3937 Albedo % for VIS data and 0.433 K for IR and WV data.

### 1.1 Preprocessing: Data from Autosat-2

#### 1.1.1 Navigation

In general, Autosat-2 produces images on predefined areas in specified map projections, usually polar stereographic, using a nearest-neighbour method. However, for the AIP-2, PDUS products were originally

*EUMETSAT Research Fellow

produced on an area which was incorrectly defined, and not quite a true rectangle on a standard polar stereographic projection. Knowing the exact definitions of both the old (incorrect) and new (correct) areas, post processing was carried out on all images to correct for this error. This is the cause of the bands containing "missing data" values.
Having corrected for the above error, the navigation of the PDUS data supplied by Autosat-2 was found to be acceptable.

### 1.1.2 Calibration

The general method employed on Autosat-2 to convert the PDUS IR and WV channels digital counts into brightness temperatures was as follows:

$$R_i = (C_i - S_i) \cdot M$$

where

$R_i$ is the radiance in the particular channel
$C_i$ is the instrument count in that channel
$S_i$ is the space count
$M$ is the MIEC coefficient

The relevant space count and MIEC calibration coefficient were extracted from the PDUS data stream. The temperature corresponding to this radiance was extracted from the relevant lookup table (published by ESOC). For further details, please refer to the Meteosat calibration reports published by ESOC.

For visible data, an albedo ($A$) was calculated for each image pixel using the expression (see Section 3 for ERROR in the expression):

$$A = \left( \frac{c \cdot f \cdot \sec\phi \cdot 2 \cdot \pi}{S} \right) \cdot 100$$

where

$c$ is the raw visible count;
$\sec\phi$ is the secant of the solar zenith angle;
$S = 1395 Wm^{-2}$ is the extraterrestrial solar constant (UK Met. Office - "Forecaster's Handbook");
$f = 1.0$ $\mathrm{Wm^{-2}\ sr^{-1}\ count^{-1}}$ is an empirical calibration factor, derived from the Meteosat-4 calibration campaign (Kriebel and Amman, 1991). Note that this value is consistent with that determined for cloud, in the campaign; other surfaces were found to have different values.

If the solar zenith angle $\phi$ was greater than $88^o$ for a given pixel, it was set as "missing data".
Once the product value (temperature or albedo) was determined for a particular pixel, a linear scaling was then applied to obtain a pixel value in the range 0→254 (corresponding to a temperature range of 198-308 K or albedo range of 0-100%).

## 1.2 Preprocessing: Data from other sources

Due to various problems during the acquisition period, (including data, hardware, software and communications problems) a number of the expected images were not archived. Where possible, gaps in the data set have been filled in using data from the following sources:
Darmstadt (ESA) archive;
FRONTIERS (i. e. UK Met. Office) satellite archive.

PDUS data from both ESA and FRONTIERS were received as uncalibrated space-view data and so had to be both calibrated and navigated to replicate the processing performed by Autosat-2.

### 1.2.1 Navigation

Navigation of the space-view data to the required polar stereographic image on the AIP-2 area was carried out using a version of the Autosat-2 navigation programmes to ensure compatibility between the products generated in the two modes of operation. The vertices of the products were defined correctly; the adjustment process specified in 1.1.1 was not, therefore, needed.

### 1.2.2 Calibration

1. ESA infrared and water-vapour data and FRONTIERS water-vapour data.
   These data were calibrated using the same basic method as used by Autosat-2. The MIEC coefficients and space-count values were extracted from the relevant Meteosat calibration report.
2. ESA and FRONTIERS visible data.
   These data were converted to albedo value using an off-line version of the standard Autosat-2 method.
3. FRONTIERS infrared.
   These data were already calibrated to temperature by the FRONTIERS PDUS receiving system using the standard method outlined above. A simple linear rescaling was employed to provide pixel values in the range 0→254 (corresponding to a temperature range of 198→308K) as required to replicate the processing performed by Autosat-2.

### 1.2.3 Image validation

Lengthy case studies were carried out to validate both the calibration and navigation of the ESA and FRONTIERS images relative to those produced by Autosat-2. The calibration was found to be satisfactory in both cases, thereby ensuring that the complete dataset is internally consistent. It was discovered that there were small systematic navigation shifts between both Autosat-2/FRONTIERS and Autosat-2/ESA image comparisons. Empirical corrections were derived by shifting images to fit the nominal coastline and applied to correct for these shifts.

## 2 Results Summary

In *Tab.1* is summarized the amount of data used for the analyses. During the campaign, the satellite was subject to the spring eclipse (from $26^{th}$ February throughout the rest of the campaign) (see Meteosat-4 Cal. Rep., issues 9-10). During most of the eclipse, the radiometer was in stand-by mode for slots 47, 48, 01, and 02 resulting in the loss of imagery for these slots.

For each channel and each image, the following products have been produced:

- Number of pixels analysed [N];

- Minimum [min] and maximum [MAX] value;

- Mean:

$$\bar{x} = \frac{\sum_{i=1}^{N} x_i}{N}$$

- Standard Deviation:

$$s_2 = \sqrt{\frac{\sum_{i=1}^{N} (x_i - \bar{x})^2}{N-1}}$$

- Coefficient of Skewness:

$$s_3 = \frac{\sum_{i=1}^{N} (x_i - \bar{x})^3}{(N-1) \cdot s_2^3}$$

- Coefficient of Kurtosis:

$$s_4 = \frac{\sum_{i=1}^{N}(x_i - \bar{x})^4}{(N-1)\cdot s_2^4} - 3$$

- Frequency distribution for classes as specified in *Tab.2*;

Although the distributions are expected to be bi- or tri-modal and hence not normal, the coefficient of Skewness and Kurtosis were computed and reported as parameters contributing to the description of the distribution.
For each month the results are shown in form of summary panels (*Fig.1-9*)

Referring to *Fig.1-9*, each summary panel contains the following information:
FRAME A: Time series of the number of images available for each day;
FRAME B: Time series of the percentage of pixels of the full image containing useful data;
FRAME C: Time series of the frequency histogram where the contour lines correspond to [1] 1%, [2] 10%, [3] 25%, [4] 50% for the classes reported in *Tab.2*;
FRAME D: Time series of the coefficient of Kurtosis;
FRAME E: Time series of the coefficient of Skewness;
FRAME F: Time series of the Standard Deviation;
FRAME G: Time series of the mean, minimum and maximum values;
FRAME H: Cumulative histogram for the classes reported in *Table 2*;
FRAME I: Frequency distribution [%] of values for the coefficient of Kurtosis;
FRAME J: Frequency distribution [%] of values for the coefficient of Skewness;
FRAME K: Frequency distribution [%] of values for the Standard Deviation;
FRAME L: Frequency distribution [%] of values for mean (continuous line) minimum and maximum (dashed lines).
In the April panels *Fig.3,6,9*, the column of plots on the extreme right represents the same as panels H to L except for the whole period.
The axis limits, interval and unit of measurement are reported in *Table 3*.

For each time series of statistical parameters computed from the images, some basic statistics (minimum and maximum value, mean, Standard Deviation, Skewness and Kurtosis) have been also calculated. The results are shown in (*Table 4.a-c.*) for each month as well as for the whole period (ALL).

Because of the importance of the spatial and temporal distribution of cloud systems, the position of areas of brightness temperature $T < 253K$ in the IR images has been reported in the form of a contour line for all the images available (*Fig.11*). This value has been chosen as it is often used as a threshold for possibly precipitating clouds (see for example Negri et al., 1984 or Adler and Negri, 1984).
*Fig.10* shows coastlines and the time of reference to help navigate and temporally locate the images of *Fig.11*.

# 3 Discussion of problems

## 3.1 Infrared and Water vapour

Whereas for the IR and WV channels, the original counts are linearly proportional to the radiance detected, the final products are instead linearly proportional to brightness temperature; this implies a differences between the original sensitivity and the final one. *Fig.12.A* shows the correspondence between digital count and brightness temperature for the original IR and WV compared with that for the GPCP-AIP/2 products. *Fig.12.B* shows the difference in K between each digital level for original IR and WV and GPCP-AIP/2 products.
Because of the form of the Planck blackbody function, the colder end of the temperature scale of the products has a lower inherent sensitivity and therefore not all levels are expected to be occupied in the final arrangement. For the warmer end ($T_{IR} > 295K, T_{WV} > 225K$) the original sensitivity is degraded: due to the value of the threshold such an effect should be relevant only for the WV data.

This effect can be noticed in the distribution of digital levels for the IR for which some of the levels remain unpopulated as shown in *Fig.13.A-B* in which examples of single level histograms for IR and WV imagery for the 25 March 1991 are reported.
Due to the preprocessing procedures, the occupancy of digital levels in the IR and WV imagery for Autosat-2 was different from that for other-sources imagery. In particular, the Autosat-2 imagery have the expected continuous distribution while that from the other sources shows unoccupied levels (see *Fig.13* where the image for 21:00 is not from Autosat-2). This problem, particularly evident in the WV imagery can, for example, appear as discontinuities when applying a threshold technique.

The original WV brightness temperature are distributed on a much narrow range (maximum value $\approx 270K$) the range used to rescaled (198-308 K) reduce the dynamics of the signal reducing the information for T>240 K. Nevertheless the information for cloud studies purposes should be preserved.

For the WV during the last ten days of the campaign, the imagery following the eclipse (3:00) show a bias of few degrees (3-5 K) (see *Fig.9.G* and is therefore not reliable in terms of absolute value.

## 3.2 Visible

IN THE FORMULA USED FOR COMPUTATION OF ALBEDO, THE FACTOR 2 IS SUPERFLUOUS.

IN THE HEADER OF THE "NO-AUTOSAT" IMAGES, THE MINIMUM AND MAXIMUM VALUES FOR THE PRODUCTS ARE INVERTED. THE DATA PROCESSED FOR THIS REPORT WERE CORRECTED FOR THIS ERROR.

Three distinct processes are involved in the computation of Albedo values from radiometric counts:
a) the conversion from count to radiance;
b) computation of flux from radiance;
c) the computation of the Albedo.

For the METEOSAT VIS channel, neither an in-flight calibration nor a pre-flight calibration (as for the NOAA series) are available, and therefore a vicarious calibration is needed to convert counts into radiance. Although previous studies (Koepke 1983, Rieland 1988) described different procedures to convert Meteosat VIS counts into radiance, their nature depending upon the platform, at the time of the Campaign the only procedure available to calibrate Meteosat-4 VIS counts was that suggested by Kriebel and Amman (1991). The value chosen (1.00) is very close to the one suggested for clouds (0.99) and less than any other calibration factor for other surface types. Therefore, an underestimation of the Albedo can be expected for surfaces other than clouds, especially the sea surface where the calibration factor should be 1.40. The given accuracy using the proper surface type factor is $\pm 5\%$ but the validity of the calibration factors has not been tested on different climate regimes.
The space count $c_o$ value is assumed 0 while a typical value can be 5 (see Brisson et al. 1991).

Because of the bandwidth of the METEOSAT VIS channel ($0.5 - 0.9\mu$m), the value of the solar constant $S$ needed to compute the albedo is different from the broadband value used. According to Thekaekara and Drummond (1971) (see also Pinty and Szejwach 1985, Marullo et al. 1987) the solar constant in the METEOSAT VIS range is 65% of the value of the broadband solar constant, assuming a rectangular spectral response, consistent with Kriebel's calibration.

The intensity correction factor to account for the earth's elliptic orbit ranges from 1.029 (1 Feb.) to 0.997 (9 Apr.) accounting for a difference of 3% in the value used as solar constant. The effect on the GPCP-AIP/2 albedo data set is a upward trend with time.

The assumption of lambertian surface reflectivity, used to convert the radiance measurement into flux, has been used because *correct* procedures that take into account the real bidirectional reflectance properties of the reflecting surface are complex and require for additional information that is not easily available (see Kriebel 1977). Empirical procedures have been also developed (see for example Cherna et al. 1985) but

not widely tested. Such an assumption can be responsible for large errors in the final estimate especially for low satellite or solar zenith angles.

Because no atmospheric correction has been applied, the final value corresponds to an estimate of planetary albedo. Such an estimate can be considered to be close to the surface albedo in case of clouds but can account up to 30% error for low albedo surface types (see for example Chen and Ohring 1984, Nacke 1991).
The solar zenith angle threshold ($\phi > 88^o \Rightarrow sec\phi = 28.7$) used to distinguish "dark" from "light" pixels appears to be too high. For such an angle, each count, using the formula given, correspond to an albedo of 13 %; typical space-count value of 5 corresponds to 65 % Albedo. As a result a much stronger diurnal cycle than expected can be observed in the data (*Fig. 4-6*). For this reason and also because of the lambertian surface assumption it is suggested that the images/pixels with very low sun elevations should be used cautiously.

As a consequence of the above, it may be noticed that, although the original counts are generally distributed in a smaller range, the final distribution is almost uniform (see *Fig.4-6.H*), with the consequence of creating a false sensitivity/information related to the solar zenith angle value.

The absolute value of the albedo is therefore not reliable. Imagery near midday (10:00-15:00) may be used to follow relative temporal changes. It is recommended that early morning and late afternoon imagery be used with caution.
If a physical value of the albedo is needed, for example to apply a previously developed algorithm or to compare with radiative transfer model results, several corrections can be suggested:

1. Taking into account the two major sources of error (the factor 2 and the solar constant) a *theoretical* correction factor can be computed as follow.

   If the lambertian hypothesis is kept and the intensity correction factor to account for the earth's elliptic orbit is set to one the "correct" formula can be written as:

   $$A^* = \left( \frac{(c - c_o) \cdot f \cdot \sec\phi \cdot \pi}{S_M} \right) \cdot 100$$

   where: $c_o = 5$ is the space count and $S_M = 0.65 \cdot S$ is the solar constant in the METEOSAT spectral range.

   By comparing with the formula used to process the data set the following equation relating the "correct" ($A^*$) and the "incorrect" estimate of the albedo ($A$) can be used:

   $$A^* = \frac{A}{0.65 \cdot 2} - \left( \frac{c_o \cdot f \cdot \sec\phi \cdot \pi}{S_M} \right) \cdot 100 = 0.76 \cdot A - 1.73 \cdot \sec\phi$$

   An average value of $\sec\phi$ have been computed over the period of the campaign for $9:00 < time < 16:00$ over the area, for such a period the variation inside the specified time interval are small. As a result a value of $\sec\phi = 2.07$ can be applied to the previous formula to give an approximate correction formula valid for the specified time interval:

   $$A^* = 0.76 \cdot A - 3.58$$

2. Using "simultaneous" measurements of Albedo from the channel 1 of the AVHRR ($0.58 - 0.68\mu m$) as a reference value, an *empirical* correction factor can be computed.

   The average values for AVHRR Channel 1 albedo images during the GPCP-AIP/2 (Liberti, 1992) have been compared with METEOSAT Visible image that was closest in time. A linear regression fit of the form:

   $$A^* = a \cdot A + b$$

has been applied to the data set.

*Fig.14* shows the scatterplot of the points and the linear regression lines.

In *Fig.14.A* all the data are included [a=0.487, b=14.7, r=0.305, n = 215 [1] ].

Because the coverage of the AVHRR images inside the GPCP-AIP/2 frame is variable, a selection criterion of considering only AVHRR images having a coverage greater than 90% has been applied. Applying this criterion to compare AVHRR channel 4 with METEOSAT IR, the correlation coefficient increased to 0.991 from the value 0.838 obtained considering all the data. *Fig.14.B* shows the results [ a=0.728, b=-5.61, r=0.787, n=77]

The data set obtained applying the coverage threshold criterion has been divided into two subsets representing approximately high ($time \leq 9:00$ or $time \geq 16:00$) and low ($9:00 < time < 16:00$) solar zenith angle; the results are shown respectively in *Fig.14.C* [a=0.897 b=-10.0 r=0.826, n=29] and *Fig.14.D* [a=0.758 b=-10.0 r=0.946 n=48].

Histograms of the ratio between collocated AVHRR channel 1 albedo estimates and those for METEOSAT have also been produced for an independent set of high solar zenith angle imagery (June 1992) and show good agreement with the correspondent linear regression coefficients.

One problem arising from such a procedure is that the AVHRR values used are already an indirect estimate of the albedo and may contain inherent errors. Also the two visible channels have different bandwidths.

3. Climatological values of 10% for the sea, 30% for the land and 60% for the cloud (see Kondratiev, 1973) have been compared with the expected peaks in the cumulative histograms for the GPCP-AIP/2 data set (*Fig.4-6.H*). The result are plotted in *fig.14.D* as circles.

Considering the independent approaches of the three correction procedures described, the results show a good agreement. While the climatological data cannot be used to obtain any quantitative correction formula, but just to check the consistency of the other two methods, the correction formulae obtained "theoretically" and comparing with AVHRR data are in near perfect agreement for the slope coefficient while there is a difference of 6.5 Albedo % in the intercept value. The effect of the use of one formula rather than the other is therefore a bias due to the difference in the intercept value; such a difference would be more important for surface with low albedo than for clouds. However in retrieving the theoretical correction formula, the value used for the conversion factor is the one suggested for clouds and, as discussed before, will result in an underestimate for low albedo surfaces.

A very detailed discussion on the problems connected to the determination of surface albedo from METEOSAT VIS data can be found in Nacke (1991).

The effects of remapping on a nearest-neighbour basis as well as the non-uniform original resolution in the S-N direction should be taken into consideration when applying spatially based algorithms (see for Example Wu et al, 1985, Adler and Negri 1988).

*****

The author is grateful to Dr.J.Foot for his help in producing this report, to J.S.Armstrong and Miss J.Ace for his help in editing it and to R.Allam, U.DeSilva, G.Holpin, Miss P.Brown and D.Offiler for their technical assistance.

## REFERENCES

Adler, R.F. and A.J.Negri, 1988. A satellite infrared technique to estimate tropical convective and stratiform rainfall. J. of Appl. Meteor., vol. 27, no.1, 30-51.

Allam, R.J., P.Dibben, G.Holpin, F.Smith and A.P.Standley, 1990. The use of satellite imagery products for operational meteorology. Proceedings of the $5^{th}$ Conference on satellite meteorology and oceanography, held in London, 3rd-7th September 1990, 401-403. Published by the American Meteorological Society.

[1] r= correlation coefficient, n = number of images

Brisson, A., P.Le Borgne and Marsouin, 1991. Relative Calibration of the Meteosat Visible Radiometers. Proceedings of the $8^{th}$ Meteosat Scientific User Meeting. EUM P 08. 39-43.

Chen, T.S. and G.Ohring, 1984. On the relationship between clear sky planetary albedo and surface albedo. J. Atmos. Sci., 41. 156-158.

Cherna, E.V., A.Bellon, G.L.Austin and A.Kilambi, 1985. An objective technique for the delineation and extrapolation of thunderstorms from GOES satellite data. J. Geophys. Res., Vol.90, no.D4. 6203-6210.

Nacke G. 1991. Surface albedo derived from METEOSAT imagery with an application to Africa. J. Geophys. Res., Vol.96, no.D10. 18581-18601.

Koepke, P., 1982. Vicarious calibration in the solar spectral range by means of calculated radiances and its application to Meteosat. Appl. Opt., 21. 2845-2854.

Kondratiev, K.Ya., 1973. Radiation characteristics of the atmosphere and the earth's surface. Amerind Publishing Co. Pvt. Ltd. Ppgg 580.

Kriebel, K.T., 1977. Reflection properties of vegetated surfaces: tables of measured spectral biconical reflectance factors. Wiss. Mitt. 29, Meteorol. Inst., Munich, Germany.

Kriebel, K.T. and V.Amman, 1991. Absolute Calibration of the Meteosat-4 VIS-Channel. Proceedings of the $8^{th}$ Meteosat Scientific User Meeting. EUM P 08. 33-38.

Liberti G.L., 1992. GPCP-AIP/2 - Atlas: AVHRR data. GPCP-AIP/2 Report n.2.

Marullo, S., G.Dalu and A.Viola, 1987. Incident short-wave radiation at the surface from Meteosat Data. Il Nuovo Cimento. 10C, no.1. 77-90.

Meteosat-4 Calibration Report, Jan-Mar 1991, Issue 9, published by ESOC.

Meteosat-4 Calibration Report, Apr-Jun 1991, Issue 10, published by ESOC.

Negri A.J., R.F.Adler and P.J.Wetzel, 1984. Rain estimation from satellite: an examination of the Griffith-Woodley technique. J. of Clim. and Appl. Meteor. vol.23, 102-116.

Pinty, B. and G.Szejwach, 1985. A new technique for inferring surface albedo from satellite observations. J. Clim. Appl. Meteorol., 24, 741-750.

Rieland M., 1989. Diurnal variation of earth radiation budget components derived from Meteosat data. IRS '88: Current problems in atmospheric radiation. A. Deepak Publishing. 217-220.

Thekaekara, M.P. and A.J.Drummond, 1971. Standard values for the solar constant and its spectral components. Nature. 226. 6-9.

W.M.O./T.D., 1989. The Global Precipitation Climatology Project. Report of the $4^{th}$ session of the international working group on data management. WMO/TD No. 356. Bristol, U.K., 26-28 July 1989.

Wu, R., J.A.Weinman and R.T.Chin, 1985. Determination of rainfall rates from GOES satellite images by a pattern recognition technique. J. Atmos. Oceanic Technol., 2, 314-330.

# TABLES

1. DATA STATISTICS:

   (A) number of images analysed;
   (B) % of expected number of images (assuming 24 for IR and WV and 14 for VIS) (in parenthesis the value taking into account the eclipse);
   (C) number of pixels analysed;
   (D) % of pixels analysed with respect to the full frame for the images analysed.

| | Period | A | B | C | D |
|---|---|---|---|---|---|
| I | Feb | 627 | 93.3 (93.7) | 66219912 | 97.8 |
| R | Mar | 669 | 89.9 (98.1) | 70375389 | 97.4 |
| | Apr | 198 | 91.7 (100.) | 20806351 | 97.3 |
| | All | 1494 | 91.5 (96.4) | 157401652 | 97.6 |
| V | Feb | 314 | 80.1 | 29616076 | 87.3 |
| I | Mar | 399 | 91.9 | 37129325 | 86.2 |
| S | Apr | 126 | 100.0 | 11780489 | 86.6 |
| | All | 839 | 88.1 | 78525890 | 86.7 |
| W | Feb | 654 | 97.3 (97.8) | 69133076 | 97.9 |
| V | Mar | 673 | 90.5 (98.7) | 70801398 | 97.4 |
| | Apr | 195 | 90.3 (98.5) | 20482351 | 97.3 |
| | All | 1522 | 93.3 (98.3) | 160416825 | 97.7 |

2. HISTOGRAM CLASSES [Frame H, Fig. 1-9]:

| class | IR [K] | VIS [%] | WV [K] |
|---|---|---|---|
| 1 | $198 \leq T < 200$ | $0 \leq A < 5$ | $198 \leq T < 200$ |
| 2 | $200 \leq T < 205$ | $5 \leq A < 10$ | $200 \leq T < 205$ |
| 3 | $205 \leq T < 210$ | $10 \leq A < 15$ | $205 \leq T < 210$ |
| 4 | $210 \leq T < 215$ | $15 \leq A < 20$ | $210 \leq T < 215$ |
| 5 | $215 \leq T < 220$ | $20 \leq A < 25$ | $215 \leq T < 220$ |
| 6 | $220 \leq T < 225$ | $25 \leq A < 30$ | $220 \leq T < 225$ |
| 7 | $225 \leq T < 230$ | $30 \leq A < 35$ | $225 \leq T < 230$ |
| 8 | $230 \leq T < 235$ | $35 \leq A < 40$ | $230 \leq T < 235$ |
| 9 | $235 \leq T < 240$ | $40 \leq A < 45$ | $235 \leq T < 240$ |
| 10 | $240 \leq T < 245$ | $45 \leq A < 50$ | $240 \leq T < 245$ |
| 11 | $245 \leq T < 250$ | $50 \leq A < 55$ | $245 \leq T < 250$ |
| 12 | $250 \leq T < 255$ | $55 \leq A < 60$ | $250 \leq T < 255$ |
| 13 | $255 \leq T < 260$ | $60 \leq A < 65$ | $255 \leq T < 260$ |
| 14 | $260 \leq T < 265$ | $65 \leq A < 70$ | $260 \leq T < 265$ |
| 15 | $265 \leq T < 270$ | $70 \leq A < 75$ | $265 \leq T < 270$ |
| 16 | $270 \leq T < 275$ | $75 \leq A < 80$ | $270 \leq T < 275$ |
| 17 | $275 \leq T < 280$ | $80 \leq A < 85$ | $275 \leq T < 280$ |
| 18 | $280 \leq T < 285$ | $85 \leq A < 90$ | $280 \leq T < 285$ |
| 19 | $285 \leq T < 290$ | $90 \leq A < 95$ | $285 \leq T < 290$ |
| 20 | $290 \leq T < 295$ | $95 \leq A \leq 100$ | $290 \leq T < 295$ |
| 21 | $295 \leq T < 300$ | | $295 \leq T < 300$ |
| 22 | $300 \leq T < 305$ | | $300 \leq T < 305$ |
| 23 | $305 \leq T \leq 308$ | | $305 \geq T \leq 308$ |

3. PLOT SCALE AND MARKS:

FR: Reference frame;
Xm: Minimum value for the X-axis;
XM: Maximum value for the X-axis;
DX: Tick mark distance for the X-axis;
UX: Unit for the X-axis;
Ym: Minimum value for the Y-axis;
YM: Maximum value for the Y-axis;
DY: Tick mark distance for the Y-axis;
UY: Unit for the Y-axis;

METEOSAT-IR [Fig. 1-3]

| FR | Xm | XM | DX | UX | Ym | YM | DY | UY |
|---|---|---|---|---|---|---|---|---|
| A | 1 | * | 1 | DAY | 0 | 25 | 5 | IMAGES |
| B | 1 | * | 1 | DAY | 80 | 101 | 5 | PIXELS % OF THE FULL FRAME |
| C | 1 | * | 1 | DAY | 198 | 308 | 10 | K |
| D | 1 | * | 1 | DAY | -2 | 6 | 1 | |
| E | 1 | * | 1 | DAY | -2.5 | 1 | 0.5 | |
| F | 1 | * | 1 | DAY | 0.0 | 30 | 5.0 | K |
| G | 1 | * | 1 | DAY | 198 | 308 | 10 | K |
| H | 0 | 40 | 5 | % of total | 198 | 308 | 10 | K |
| I | 0 | 30 | 5 | % of total | -2 | 6 | 1 | |
| J | 0 | 30 | 5 | % of total | -2.5 | 1 | 0.5 | |
| K | 0 | 30 | 5 | % of total | 0.0 | 30 | 5.0 | K |
| L | 0 | 30 | 5 | % of total | 198 | 308 | 10 | K |

METEOSAT-VIS [Fig. 4-6]

| FR | Xm | XM | DX | UX | Ym | YM | DY | UY |
|---|---|---|---|---|---|---|---|---|
| A | 1 | * | 1 | DAY | 0 | 25 | 5 | IMAGES |
| B | 1 | * | 1 | DAY | 10 | 101 | 10 | PIXELS % OF THE FULL FRAME |
| C | 1 | * | 1 | DAY | 0 | 100 | 10 | ALBEDO % |
| D | 1 | * | 1 | DAY | -2 | 6 | 1 | |
| E | 1 | * | 1 | DAY | -2.5 | 1 | 0.5 | |
| F | 1 | * | 1 | DAY | 0.0 | 30 | 5.0 | ALBEDO % |
| G | 1 | * | 1 | DAY | 0 | 100 | 10 | ALBEDO % |
| H | 0 | 40 | 5 | % of total | 0 | 100 | 10 | ALBEDO % |
| I | 0 | 30 | 5 | % of total | -2 | 6 | 1 | |
| J | 0 | 30 | 5 | % of total | -2.5 | 1 | 0.5 | |
| K | 0 | 30 | 5 | % of total | 0.0 | 30 | 5.0 | ALBEDO % |
| L | 0 | 30 | 5 | % of total | 0 | 100 | 10 | ALBEDO % |

METEOSAT-WV [Fig. 7-9]

| FR | Xm | XM | DX | UX | Ym | YM | DY | UY |
|---|---|---|---|---|---|---|---|---|
| A | 1 | * | 1 | DAY | 0 | 25 | 5 | IMAGES |
| B | 1 | * | 1 | DAY | 80 | 101 | 5 | PIXELS % OF THE FULL FRAME |
| C | 1 | * | 1 | DAY | 198 | 308 | 10 | K |
| D | 1 | * | 1 | DAY | -2 | 6 | 1 | |
| E | 1 | * | 1 | DAY | -2.5 | 1 | 0.5 | |
| F | 1 | * | 1 | DAY | 0.0 | 30 | 5.0 | K |
| G | 1 | * | 1 | DAY | 198 | 308 | 10 | K |
| H | 0 | 40 | 5 | % of total | 198 | 308 | 10 | K |
| I | 0 | 30 | 5 | % of total | -2 | 6 | 1 | |
| J | 0 | 30 | 5 | % of total | -2.5 | 1 | 0.5 | |
| K | 0 | 30 | 5 | % of total | 0.0 | 30 | 5.0 | K |
| L | 0 | 30 | 5 | % of total | 198 | 308 | 10 | K |

*: end of the month

## 4. STATISTIC OF THE STATISTICS

| *METEOSAT-IR* | | | | | | | |
|---|---|---|---|---|---|---|---|
| | Variable | Statistics of the variable | | | | | |
| | | AV | $S_2$ | $S_3$ | $S_4$ | min | MAX |
| F | AV [K] | 261.87 | 4.54 | -0.18 | 0.00 | 249.49 | 274.20 |
| E | min [K] | 220.34 | 6.33 | -0.19 | 2.39 | 198.00 | 240.44 |
| B | MAX [K] | 285.56 | 6.12 | 2.65 | 6.27 | 280.72 | 308.00 |
| | $S_2$ [K] | 11.81 | 2.43 | 0.61 | 0.28 | 7.02 | 19.09 |
| | $S_3$ | -0.74 | 0.44 | -0.29 | -0.62 | -1.89 | 0.23 |
| | $S_4$ | 0.54 | 1.21 | 1.34 | 1.90 | -1.17 | 5.31 |
| M | AV [K] | 259.31 | 8.99 | -0.05 | -0.85 | 240.94 | 278.24 |
| A | min [K] | 214.26 | 7.29 | -0.10 | 0.01 | 198.00 | 238.71 |
| R | MAX [K] | 288.74 | 7.60 | 1.51 | 1.16 | 280.28 | 308.00 |
| | $S_2$ [K] | 16.64 | 4.72 | 0.63 | 0.36 | 7.22 | 30.93 |
| | $S_3$ | -0.64 | 0.56 | -0.04 | -0.70 | -2.23 | 0.53 |
| | $S_4$ | -0.14 | 1.35 | 1.60 | 3.29 | -1.87 | 6.39 |
| A | AV [K] | 266.05 | 4.45 | 0.09 | -1.09 | 258.20 | 274.67 |
| P | min [K] | 219.50 | 7.96 | -0.87 | 0.81 | 198.00 | 233.94 |
| R | MAX [K] | 290.66 | 7.85 | 1.06 | -0.11 | 282.02 | 308.00 |
| | $S_2$ [K] | 14.35 | 3.80 | 0.37 | -0.29 | 8.40 | 24.83 |
| | $S_3$ | -0.81 | 0.32 | -0.42 | 0.11 | -1.79 | -0.06 |
| | $S_4$ | 0.02 | 1.04 | 1.53 | 3.74 | -1.44 | 5.02 |
| A | AV [K] | 261.28 | 7.23 | -0.46 | 0.05 | 240.94 | 278.24 |
| L | min [K] | 217.51 | 7.59 | -0.32 | 0.49 | 198.00 | 240.44 |
| L | MAX [K] | 287.66 | 7.30 | 1.74 | 1.99 | 280.28 | 308.00 |
| | $S_2$ [K] | 14.31 | 4.41 | 1.01 | 1.14 | 7.02 | 30.93 |
| | $S_3$ | -0.70 | 0.49 | 0.00 | -0.37 | -2.23 | 0.53 |
| | $S_4$ | 0.17 | 1.29 | 1.32 | 2.33 | -1.87 | 6.39 |

| *METEOSAT-VIS* | | | | | | | |
|---|---|---|---|---|---|---|---|
| | Variable | Statistics of the variable | | | | | |
| | | AV | $S_2$ | $S_3$ | $S_4$ | min | MAX |
| F | AV [A%] | 57.43 | 13.15 | -1.36 | 3.99 | 4.99 | 96.56 |
| E | min [A%] | 14.22 | 8.85 | 2.54 | 16.87 | 0.00 | 77.95 |
| B | MAX [A%] | 100.00 | 0.00 | 0.00 | 0.00 | 100.00 | 100.00 |
| | $S_2$ [A%] | 21.72 | 6.17 | 1.44 | 3.74 | 7.40 | 45.16 |
| | $S_3$ | 0.04 | 0.69 | 2.17 | 10.92 | -2.73 | 4.16 |
| | $S_4$ | -0.47 | 1.77 | 6.50 | 51.94 | -1.83 | 16.92 |
| M | AV [A%] | 59.86 | 14.02 | -0.31 | 2.38 | 2.73 | 100.00 |
| A | min [A%] | 15.91 | 11.43 | 2.89 | 12.53 | 0.00 | 96.06 |
| R | MAX [A%] | 99.97 | 0.32 | -13.53 | 194.20 | 94.88 | 100.00 |
| | $S_2$ [A%] | 20.83 | 4.38 | -1.01 | 2.77 | 0.12 | 30.77 |
| | $S_3$ | -0.21 | 1.73 | -11.97 | 195.36 | -29.04 | 5.80 |
| | $S_4$ | 2.09 | 43.09 | 19.24 | 375.25 | -1.60 | 850.86 |
| A | AV [A%] | 53.43 | 14.28 | 1.91 | 3.26 | 37.72 | 99.94 |
| P | min [A%] | 15.86 | 14.30 | 2.81 | 7.99 | 0.00 | 87.01 |
| R | MAX [A%] | 99.98 | 0.18 | -11.05 | 120.02 | 98.03 | 100.00 |
| | $S_2$ [A%] | 21.96 | 5.13 | -2.19 | 4.94 | 0.66 | 27.58 |
| | $S_3$ | -0.03 | 1.47 | -6.48 | 48.82 | -12.94 | 1.09 |
| | $S_4$ | 1.28 | 18.02 | 9.88 | 101.12 | -1.56 | 193.58 |
| A | AV [A%] | 57.99 | 13.90 | -0.28 | 2.52 | 2.73 | 100.00 |
| L | min [A%] | 15.27 | 11.06 | 2.96 | 13.39 | 0.00 | 96.06 |
| L | MAX [A%] | 99.99 | 0.23 | -17.91 | 350.08 | 94.88 | 100.00 |
| | $S_2$ [A%] | 21.33 | 5.24 | 0.36 | 4.51 | 0.12 | 45.16 |
| | $S_3$ | -0.09 | 1.39 | -12.11 | 235.60 | -29.04 | 5.80 |
| | $S_4$ | 1.01 | 30.54 | 26.07 | 714.28 | -1.83 | 850.86 |

| *METEOSAT-WV* | | | | | | | |
|---|---|---|---|---|---|---|---|
| | Variable | Statistics of the variable | | | | | |
| | | AV | $S_2$ | $S_3$ | $S_4$ | min | MAX |
| F | AV [K] | 237.54 | 1.89 | -0.36 | 0.00 | 231.53 | 241.63 |
| E | min [K] | 219.98 | 5.20 | -1.55 | 5.04 | 198.00 | 230.91 |
| B | MAX [K] | 250.51 | 4.74 | 1.72 | 2.99 | 243.04 | 268.16 |
| | $S_2$ [K] | 4.59 | 0.94 | 0.69 | 0.02 | 3.01 | 7.44 |
| | $S_3$ | -0.17 | 0.38 | 0.55 | 1.19 | -1.16 | 1.75 |
| | $S_4$ | -0.01 | 0.91 | 5.36 | 57.47 | -1.03 | 12.22 |
| M | AV [K] | 235.95 | 3.37 | -0.40 | -0.91 | 228.80 | 241.42 |
| A | min [K] | 214.45 | 6.82 | -0.59 | -0.18 | 198.00 | 228.31 |
| R | MAX [K] | 252.50 | 5.12 | 1.12 | 1.27 | 242.61 | 268.16 |
| | $S_2$ [K] | 6.21 | 1.96 | 1.38 | 1.95 | 2.92 | 13.91 |
| | $S_3$ | -0.31 | 0.39 | -0.57 | 0.07 | -1.43 | 0.66 |
| | $S_4$ | -0.26 | 0.70 | 0.98 | 1.13 | -1.46 | 2.66 |
| A | AV [K] | 238.09 | 1.79 | -0.65 | 0.39 | 232.13 | 241.58 |
| P | min [K] | 219.98 | 6.23 | -0.92 | 0.93 | 198.00 | 230.05 |
| R | MAX [K] | 251.74 | 3.81 | 2.74 | 7.53 | 246.50 | 268.16 |
| | $S_2$ [K] | 4.74 | 0.98 | 0.48 | -0.49 | 3.08 | 7.17 |
| | $S_3$ | -0.22 | 0.34 | -0.80 | 1.07 | -1.34 | 0.41 |
| | $S_4$ | -0.16 | 0.66 | 2.21 | 6.42 | -1.06 | 2.96 |
| A | AV [K] | 236.91 | 2.78 | -0.86 | 0.29 | 228.80 | 241.63 |
| L | min [K] | 217.54 | 6.68 | -0.93 | 0.83 | 198.00 | 230.91 |
| L | MAX [K] | 251.55 | 4.89 | 1.44 | 2.14 | 242.61 | 268.16 |
| | $S_2$ [K] | 5.33 | 1.68 | 1.78 | 4.37 | 2.92 | 13.91 |
| | $S_3$ | -0.24 | 0.38 | -0.13 | 0.96 | -1.43 | 1.75 |
| | $S_4$ | -0.14 | 0.80 | 3.96 | 44.43 | -1.46 | 12.22 |

## LIST OF FIGURES

Fig 1 METEOSAT-IR, FEB: SUMMARY

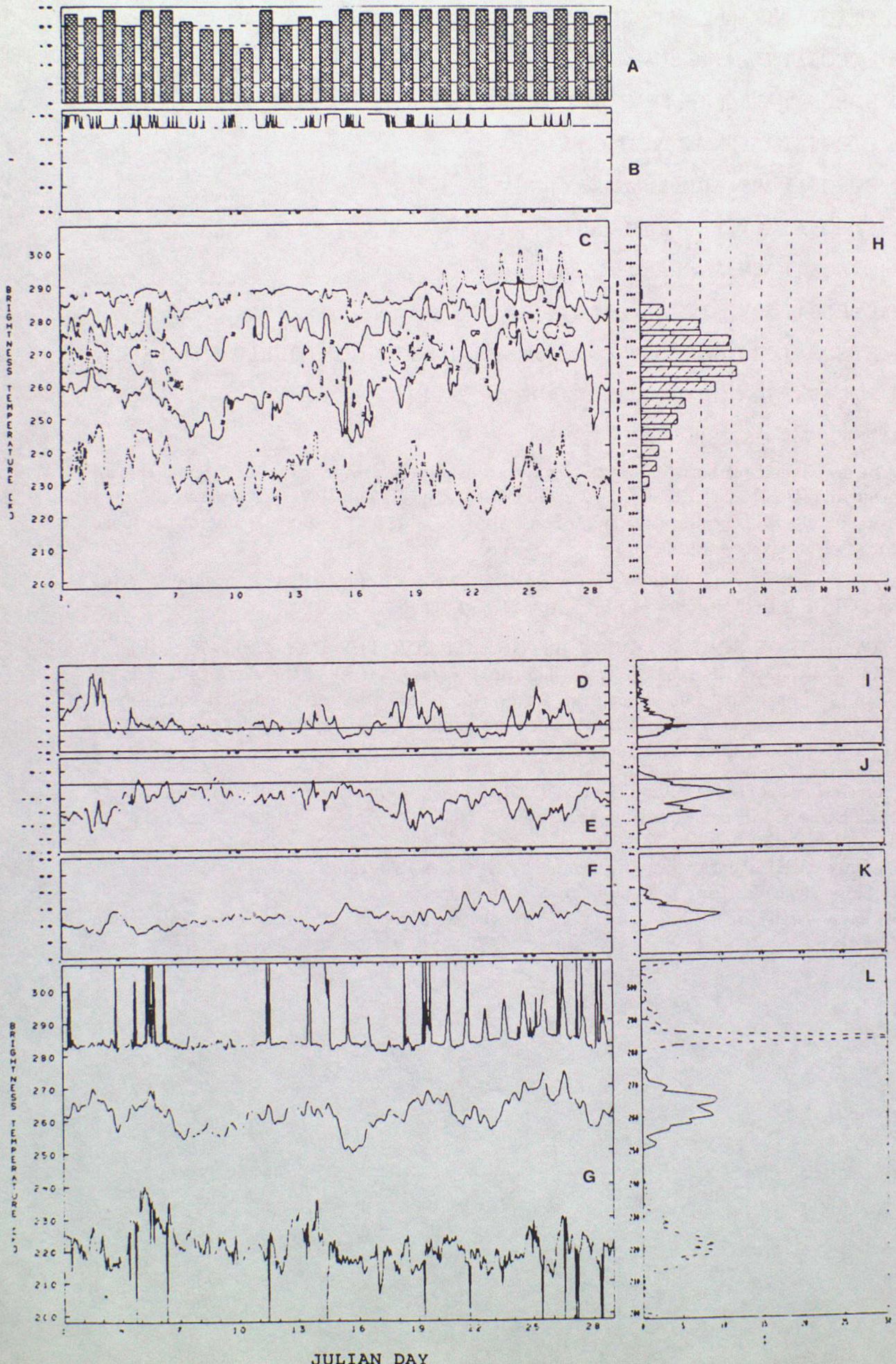

Fig 2 METEOSAT-IR, MAR: SUMMARY

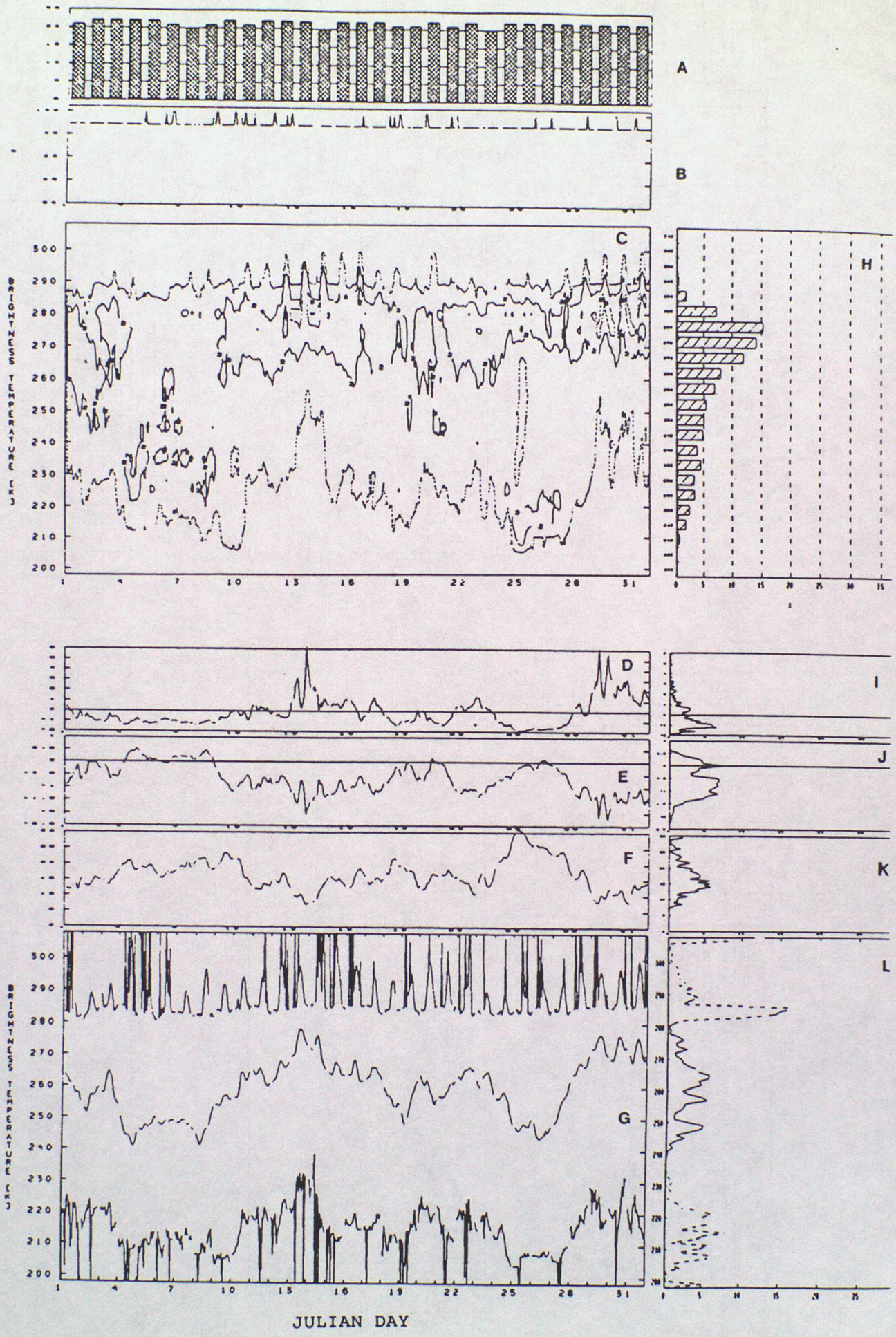

Fig 3 METEOSAT-IR, APR: SUMMARY+CUM

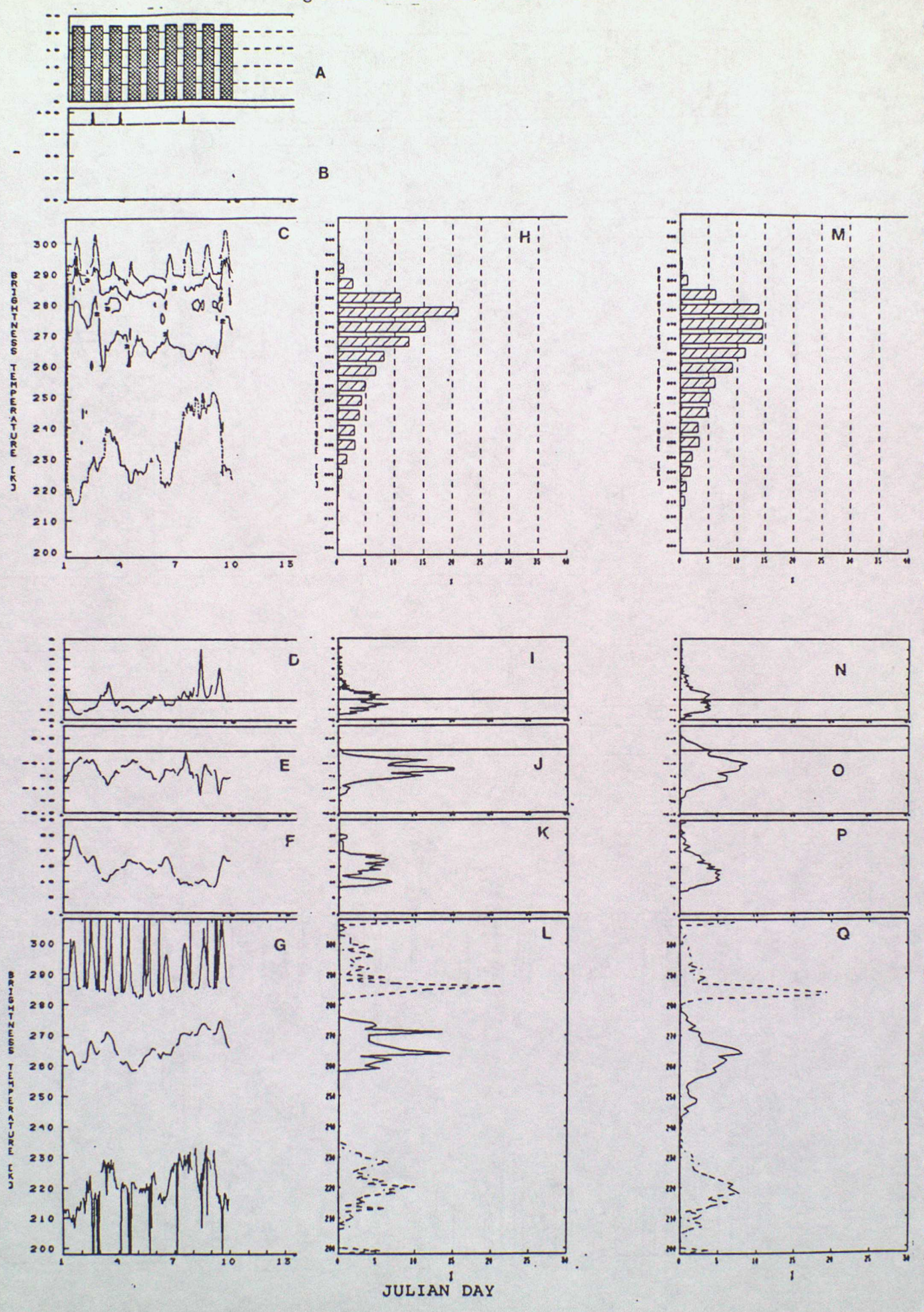

Fig 4 METEOSAT-VIS, FEB: SUMMARY

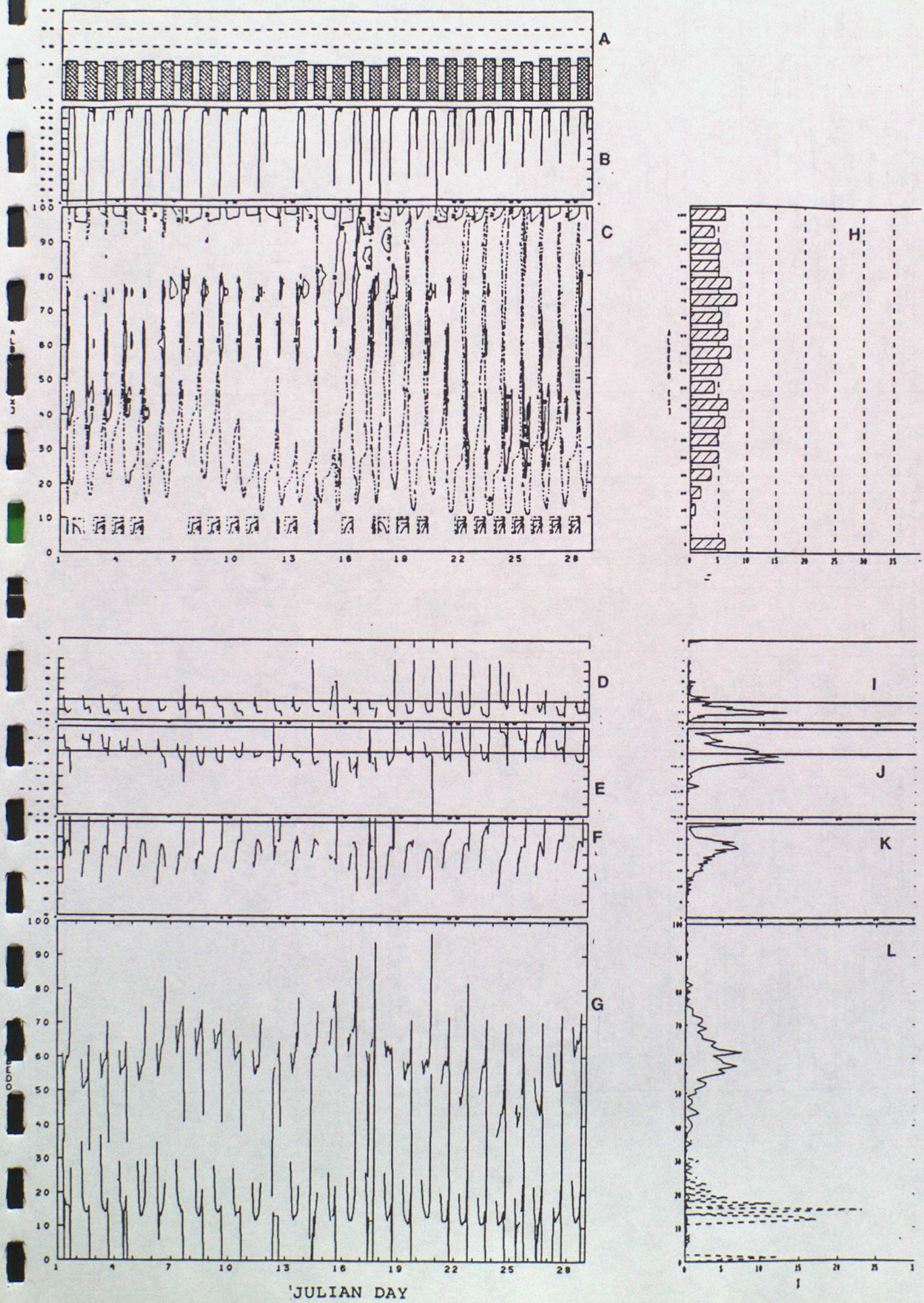

Fig 5 METEOSAT-VIS, MAR: SUMMARY

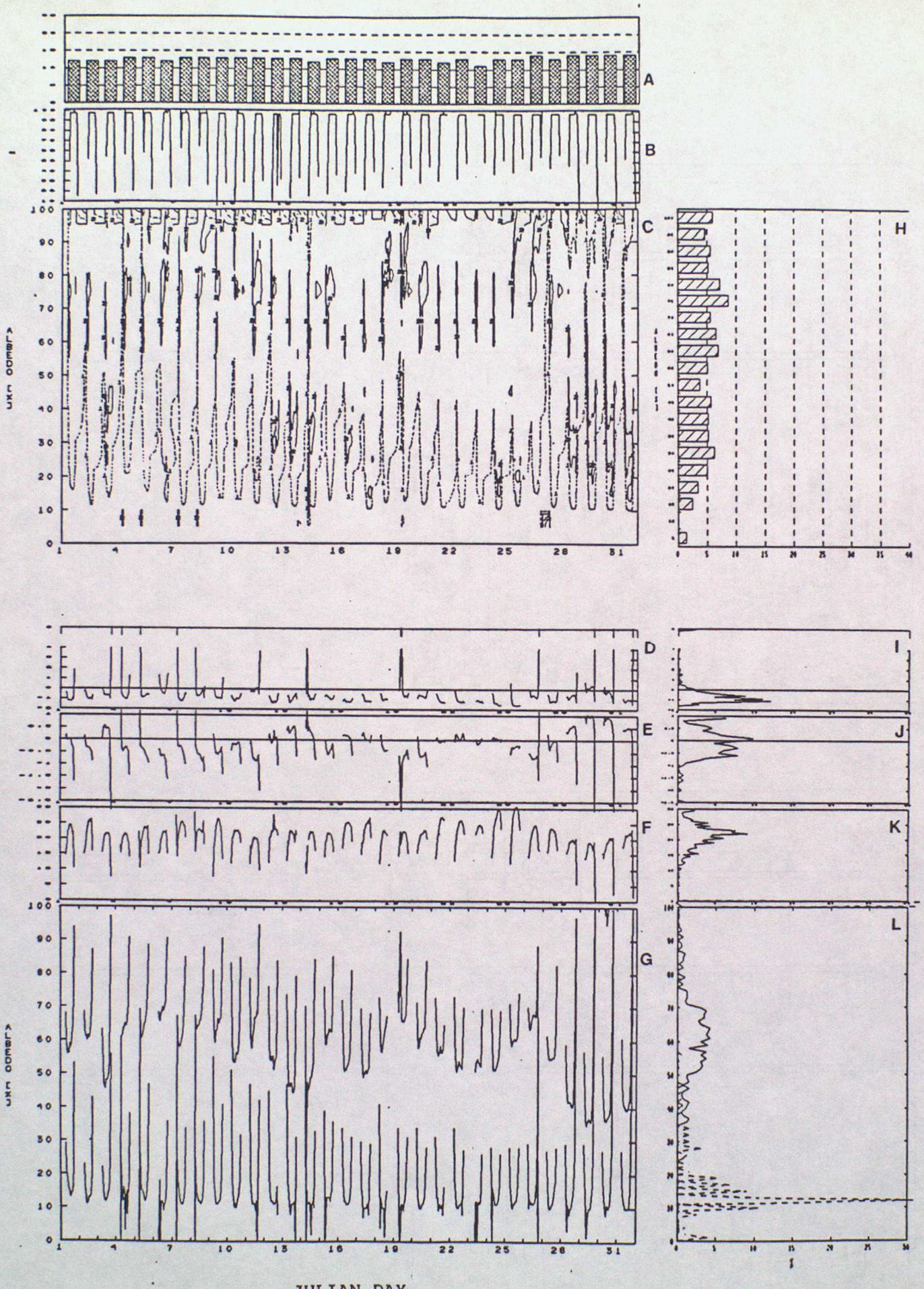

Fig 6 METEOSAT-VIS, APR: SUMMARY+CUM

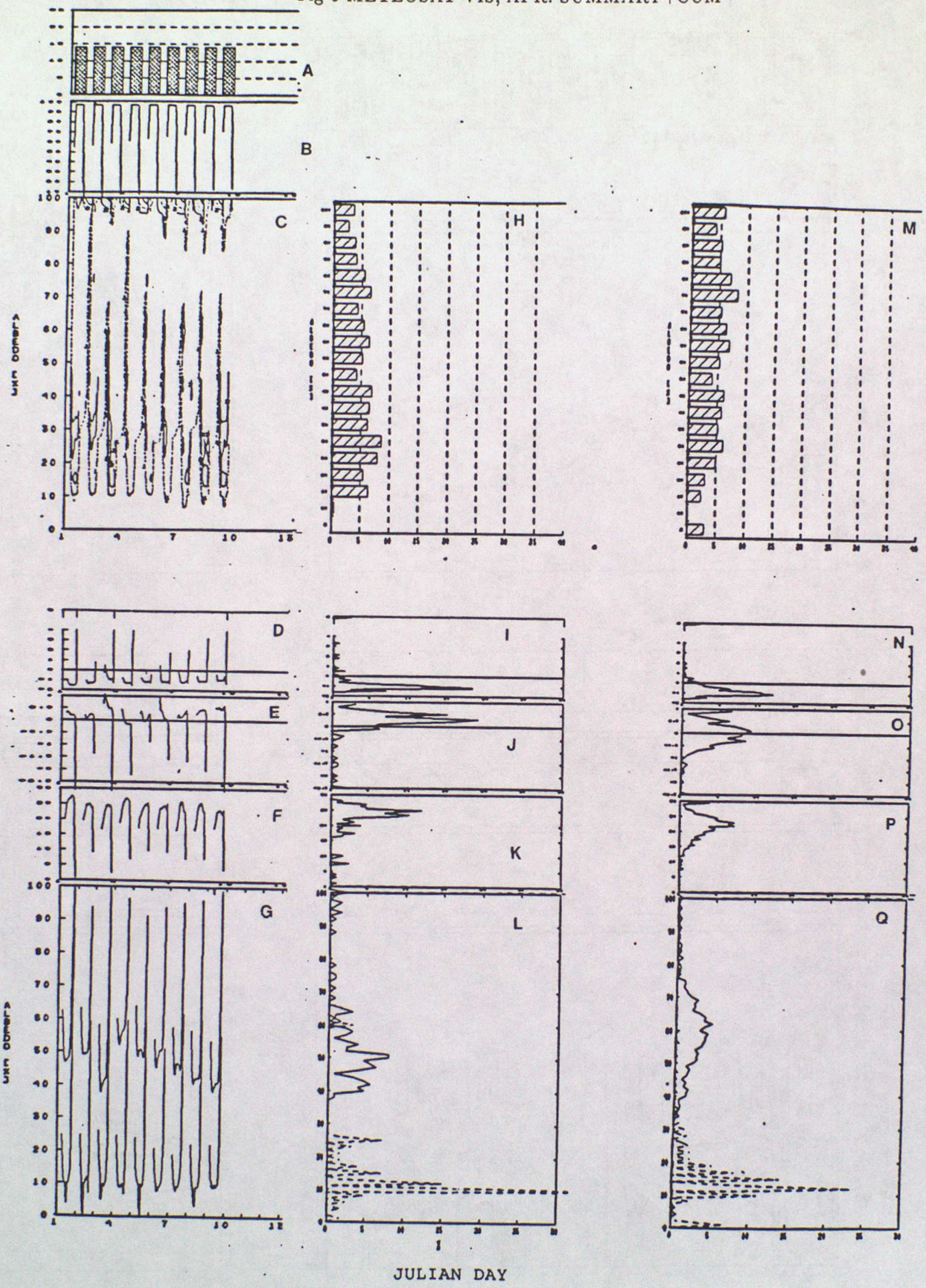

Fig 7 METEOSAT-WV, FEB: SUMMARY

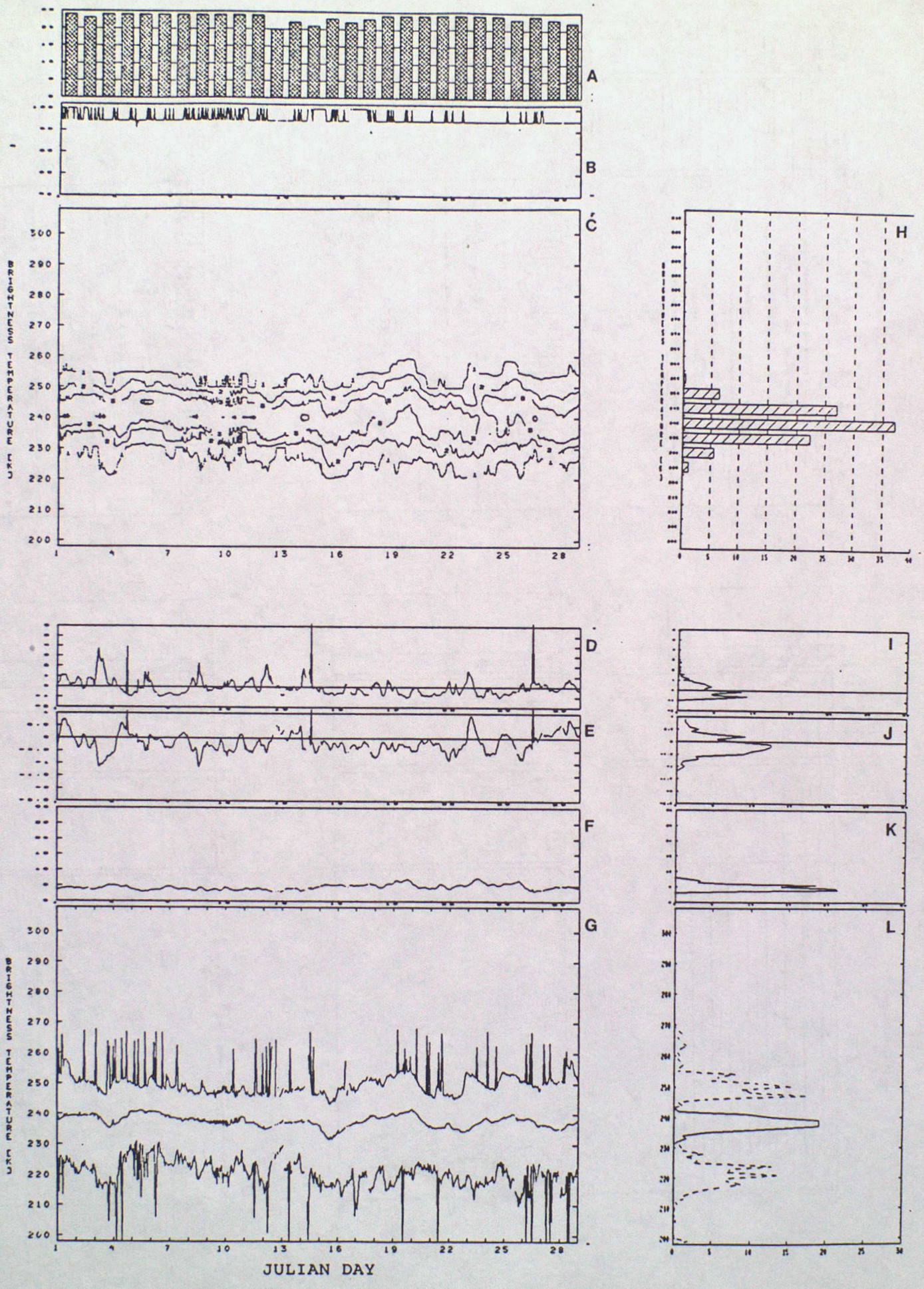

Fig 8 METEOSAT-WV, MAR: SUMMARY

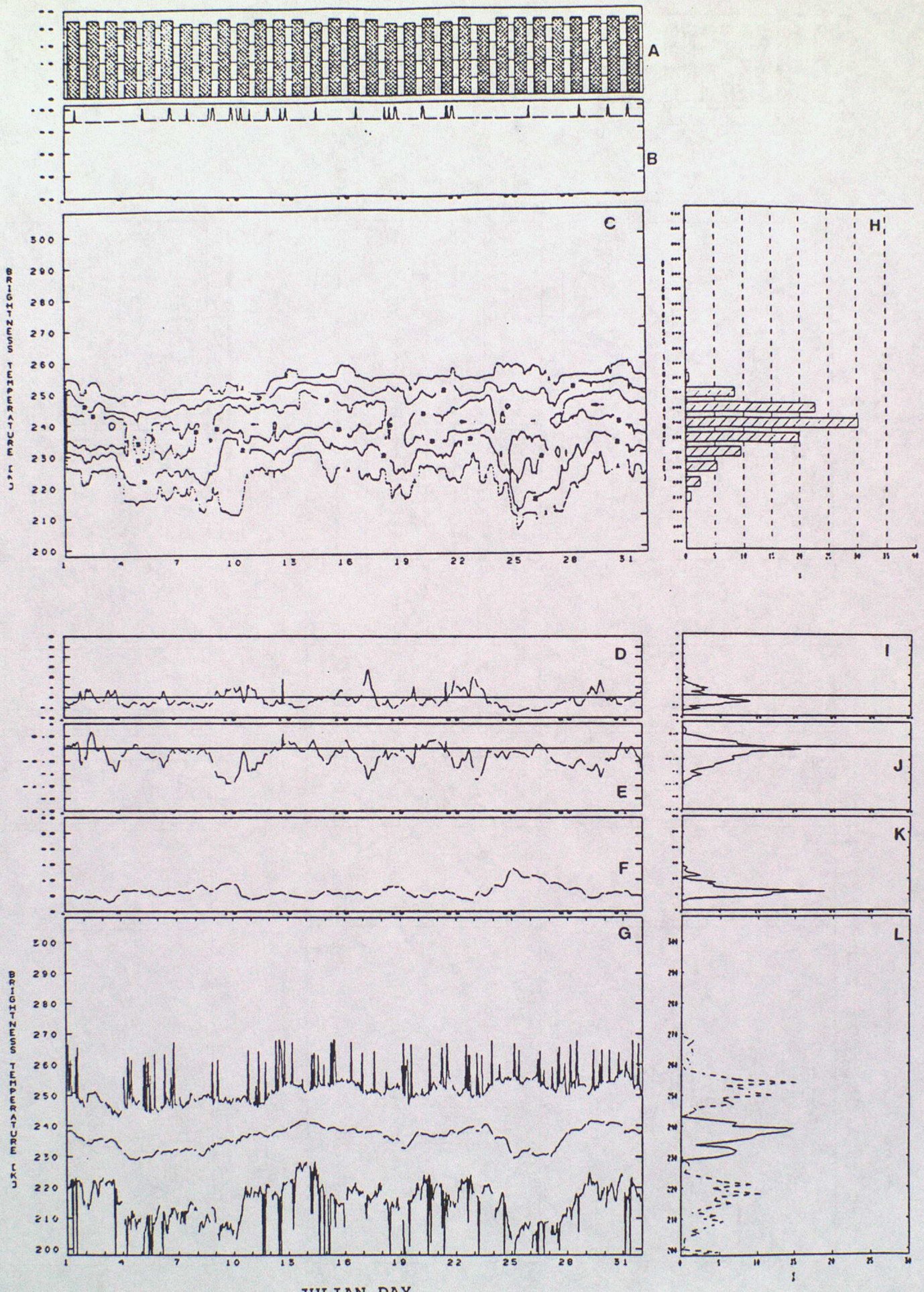

Fig 9 METEOSAT-WV, APR: SUMMARY+CUM

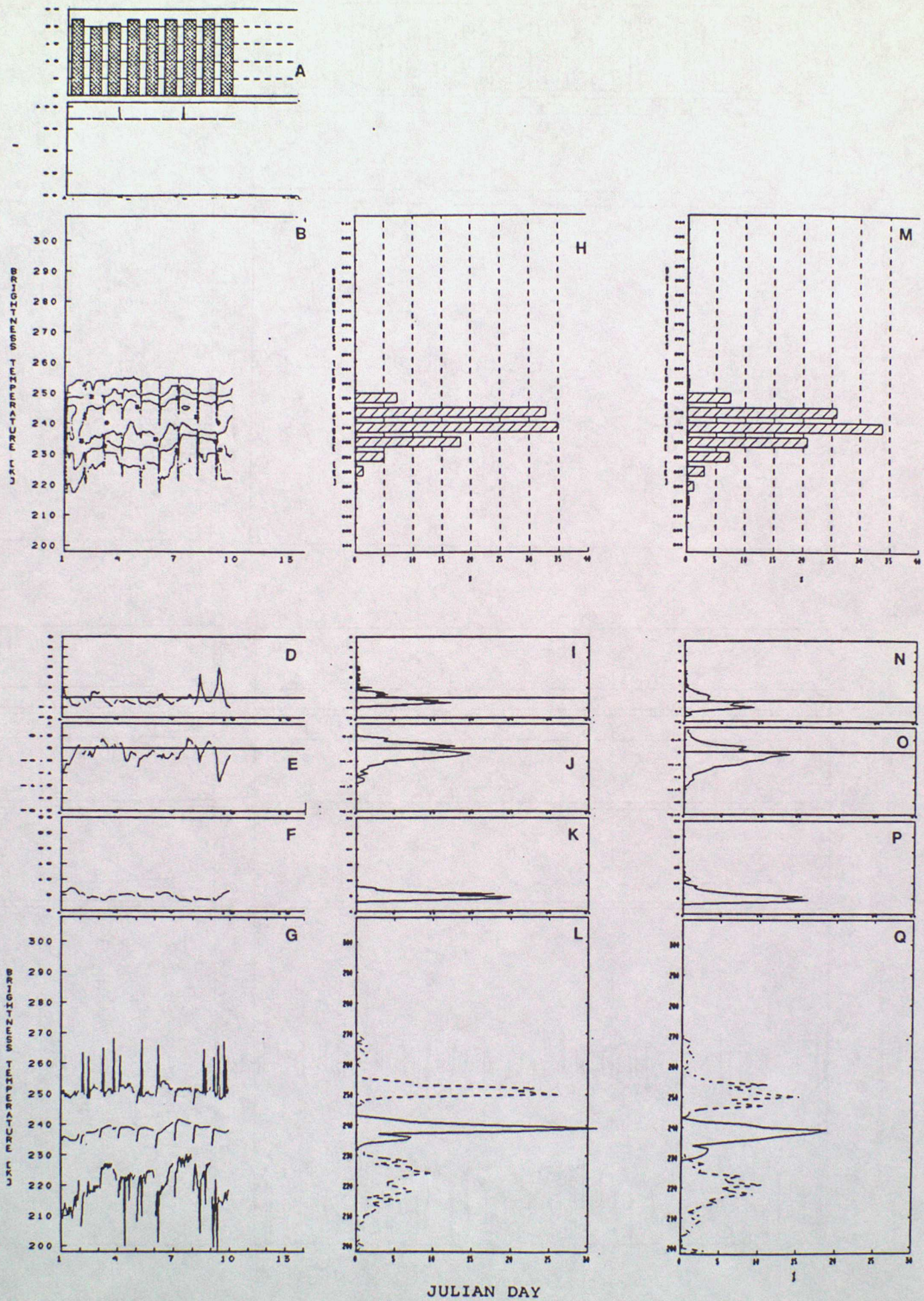

# KEY

**The time sequence of charts shown in figures 10 and 11 is given below**

**The numbers denote the hour 00,01....23 etc**

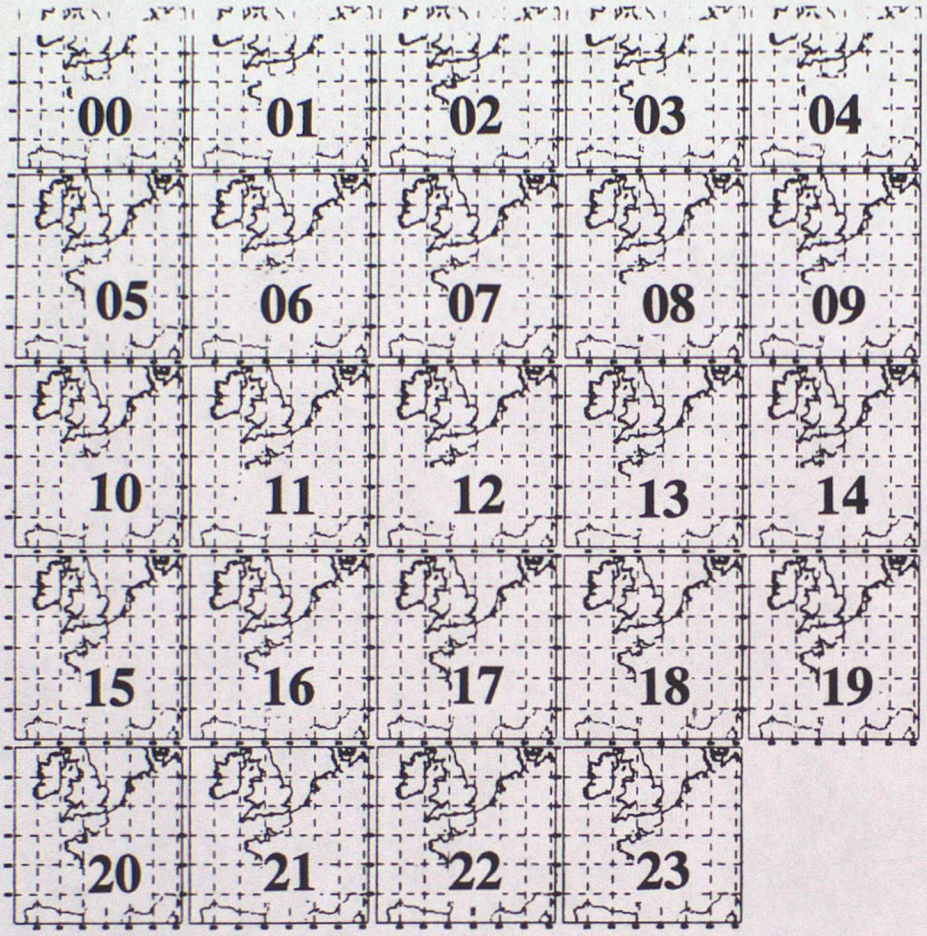


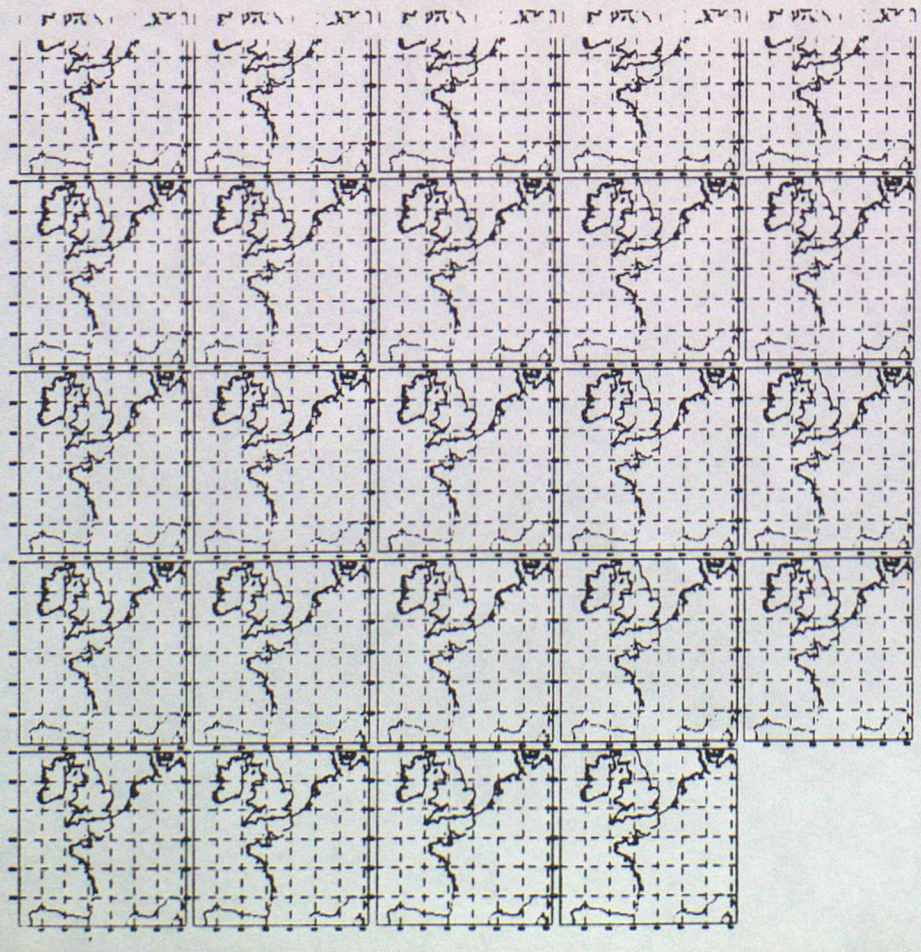

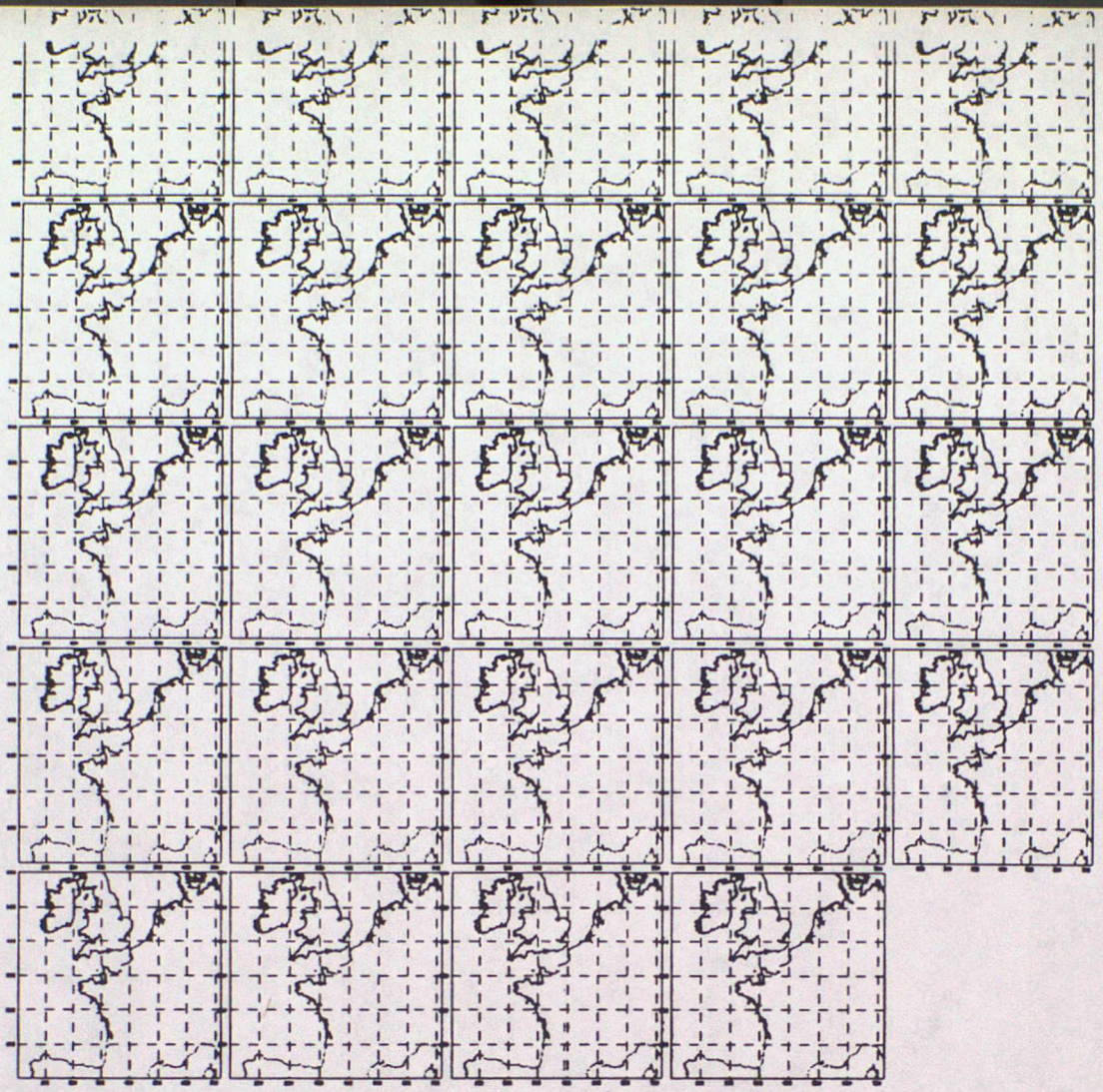

Fig 10 METEOSAT-IR GEOGRAPHICAL BOUNDARIES FOR CONTOURLINE MAPS

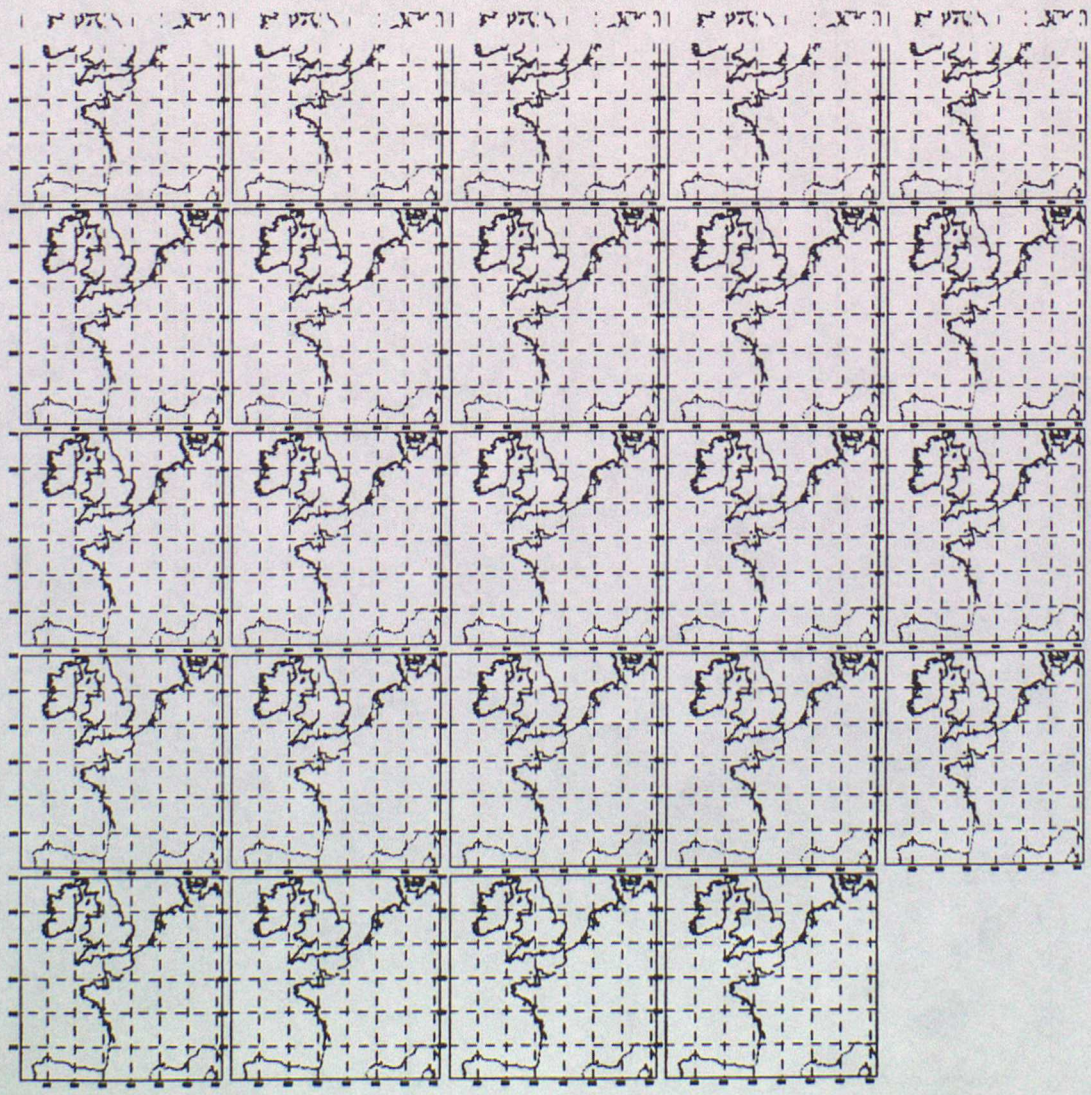

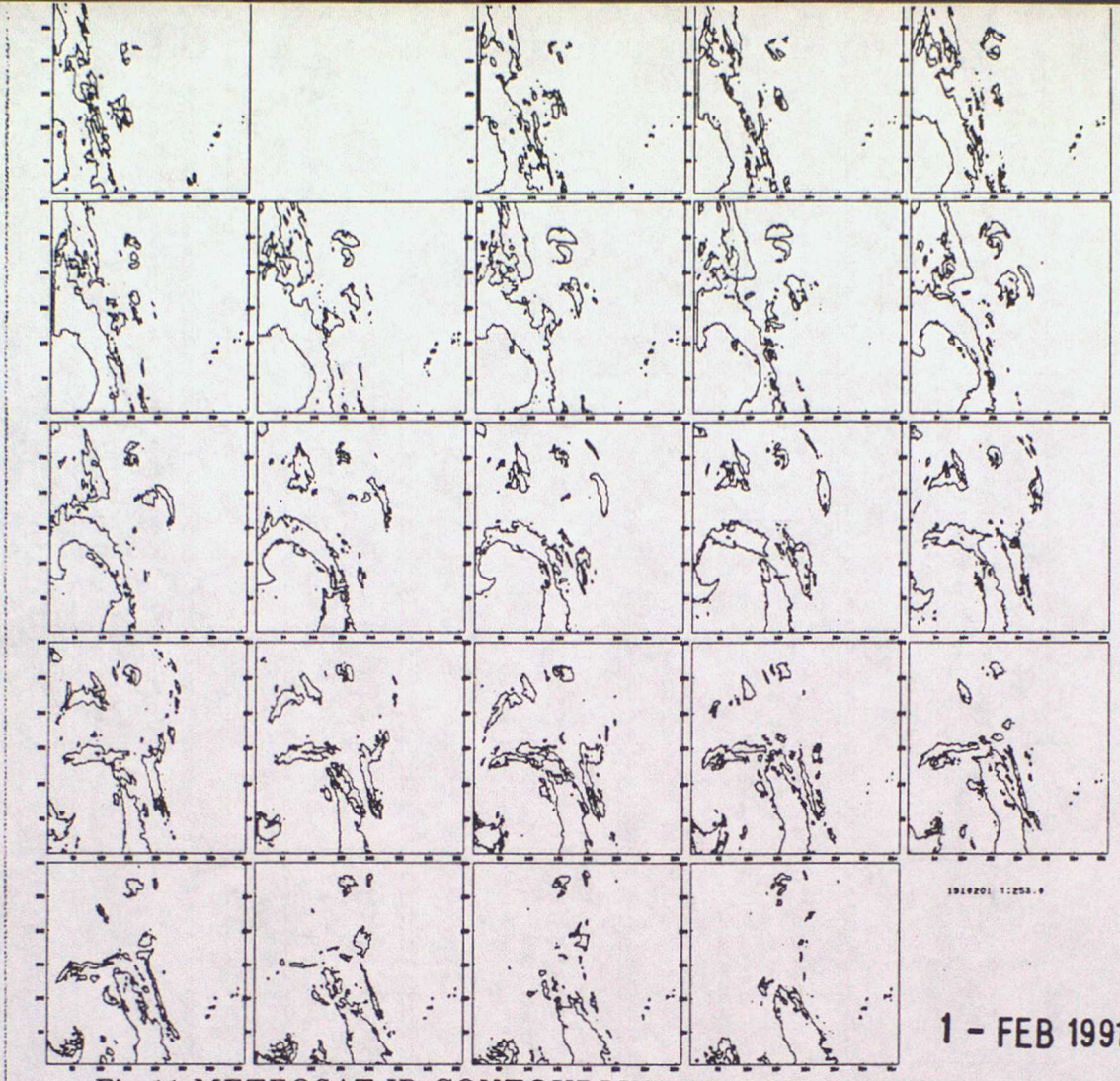


1 - FEB 1991

Fig 11 METEOSAT-IR CONTOURLINE MAPS T <253 K

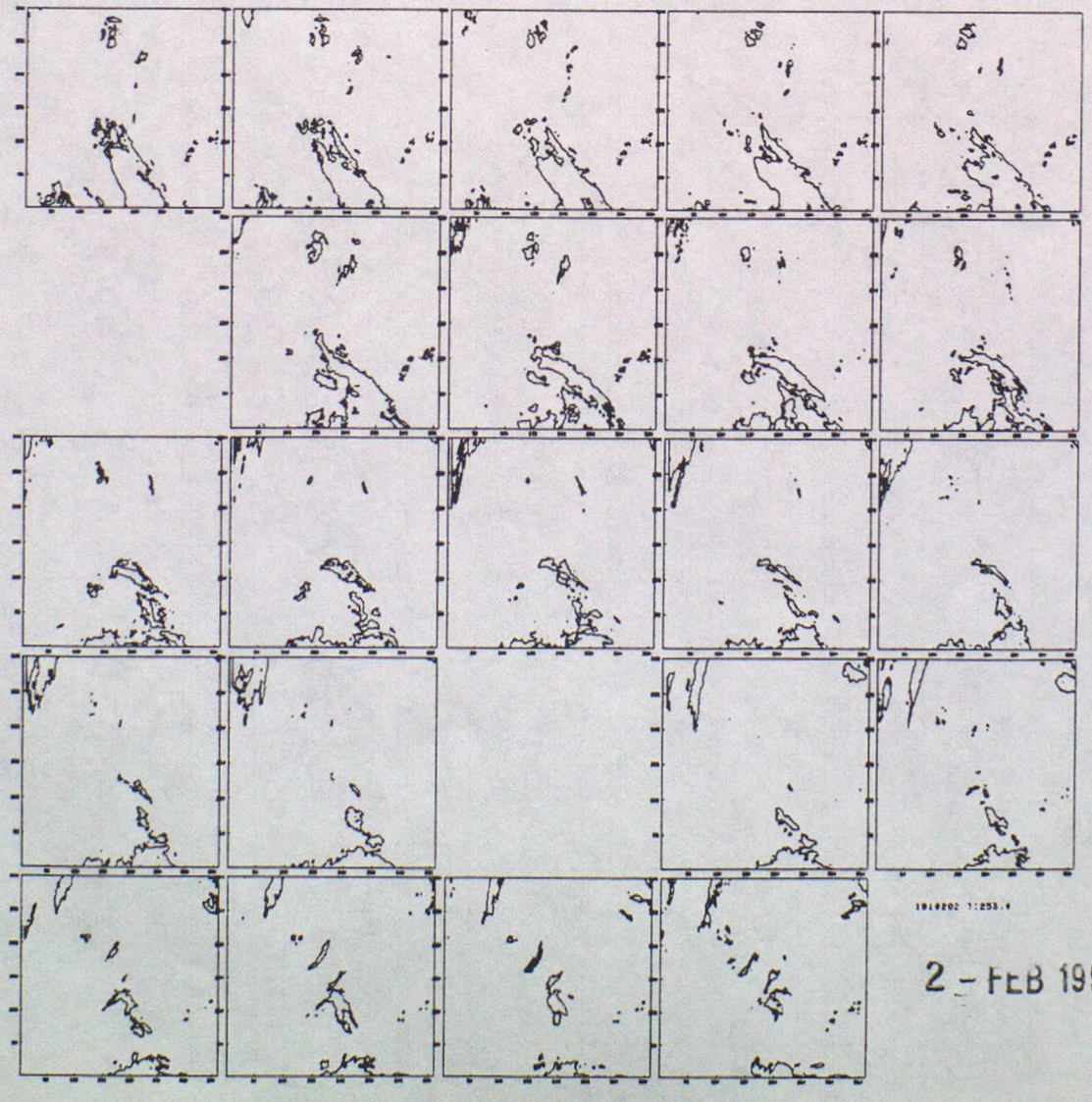


2 - FEB 1991

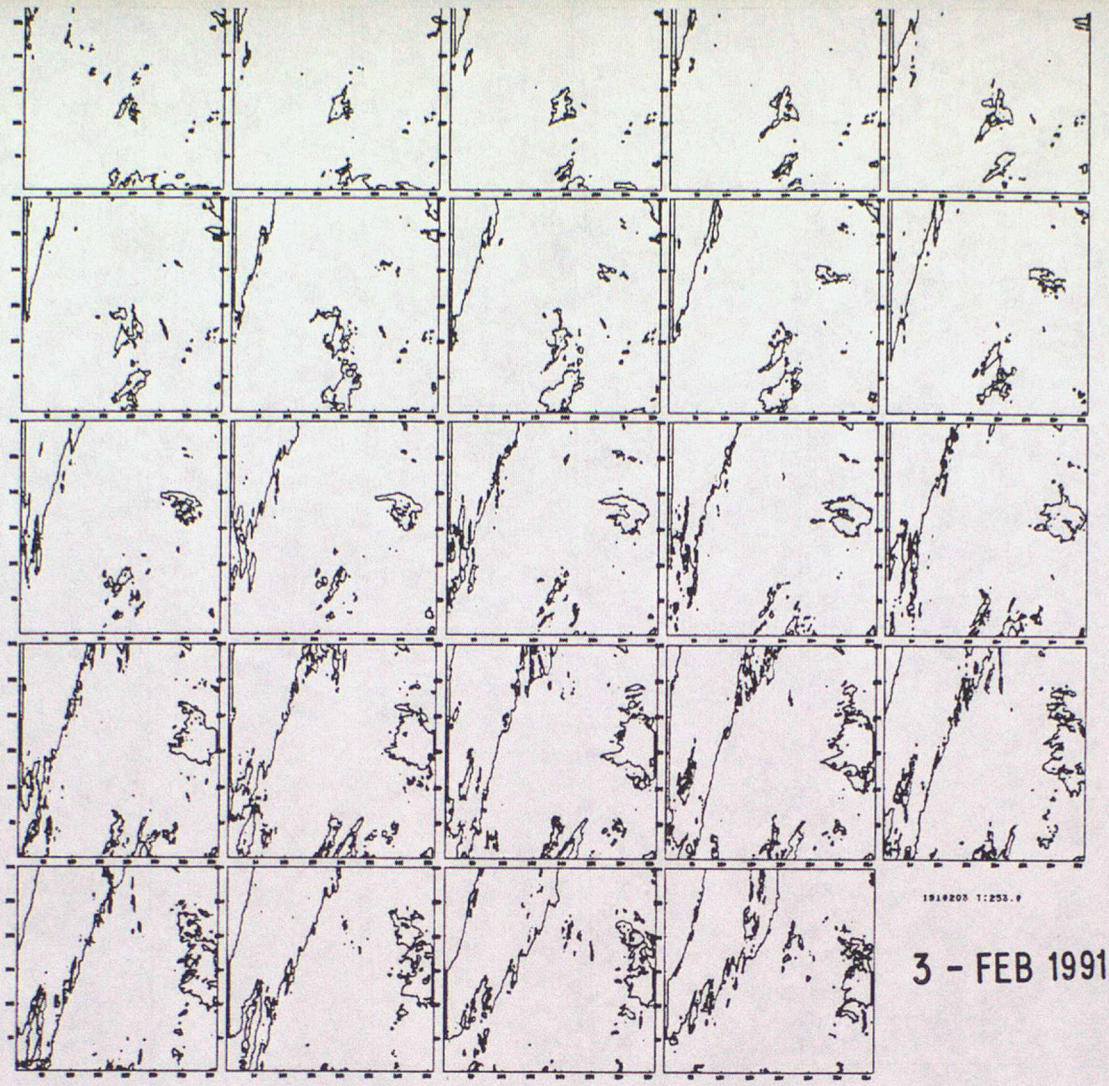


**Fig 11 Continued**

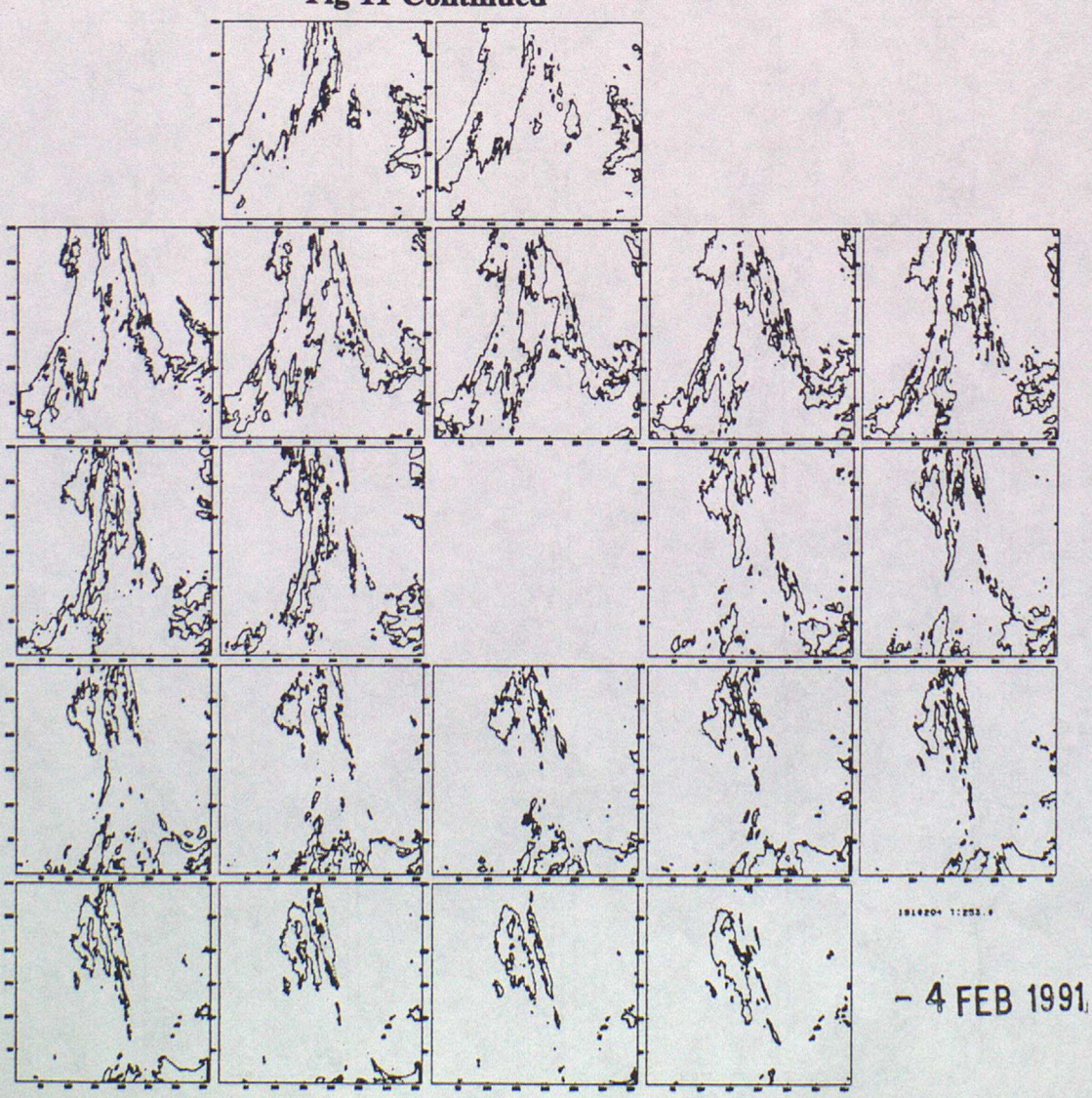

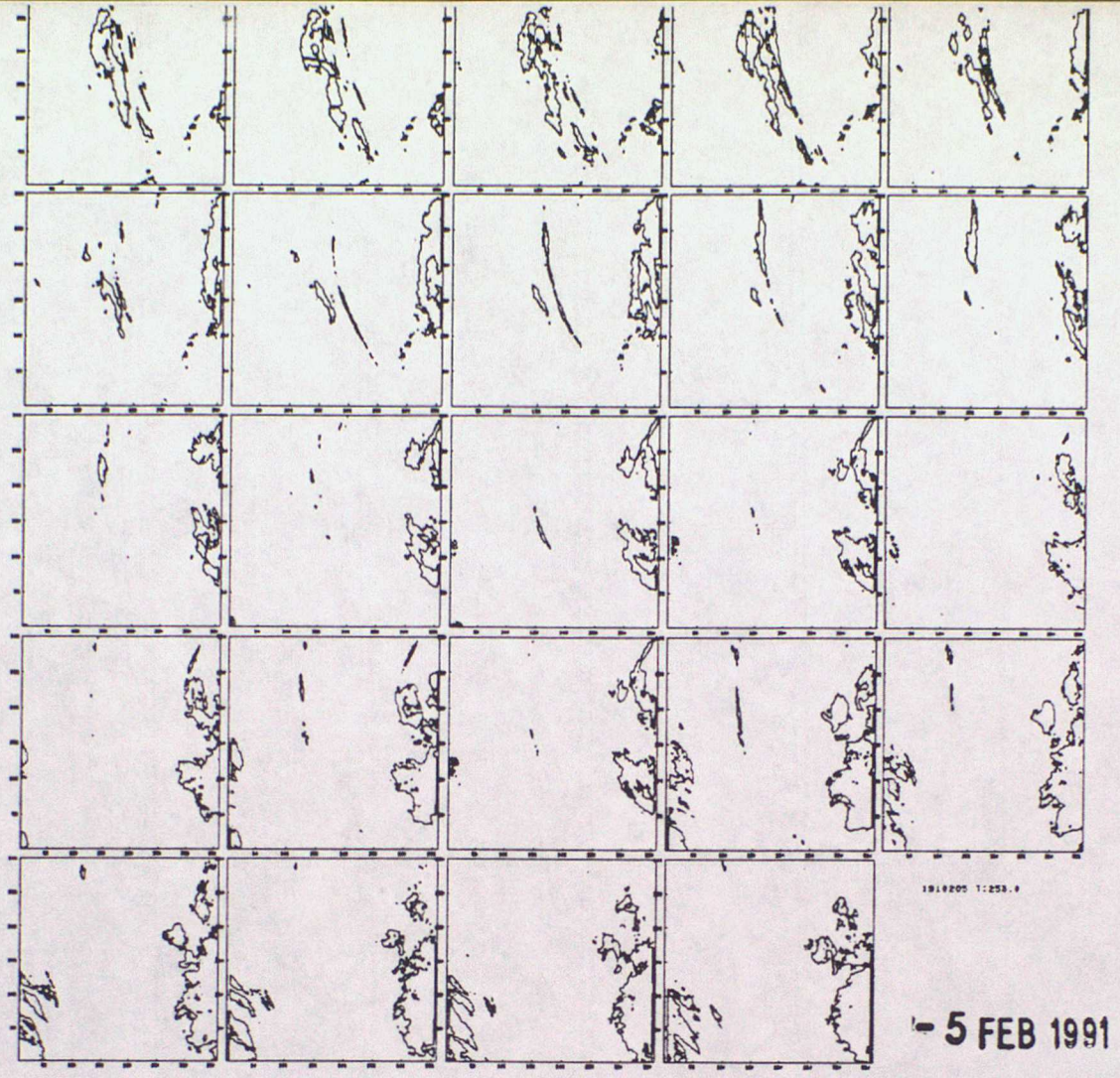


**Fig 11 Continued**

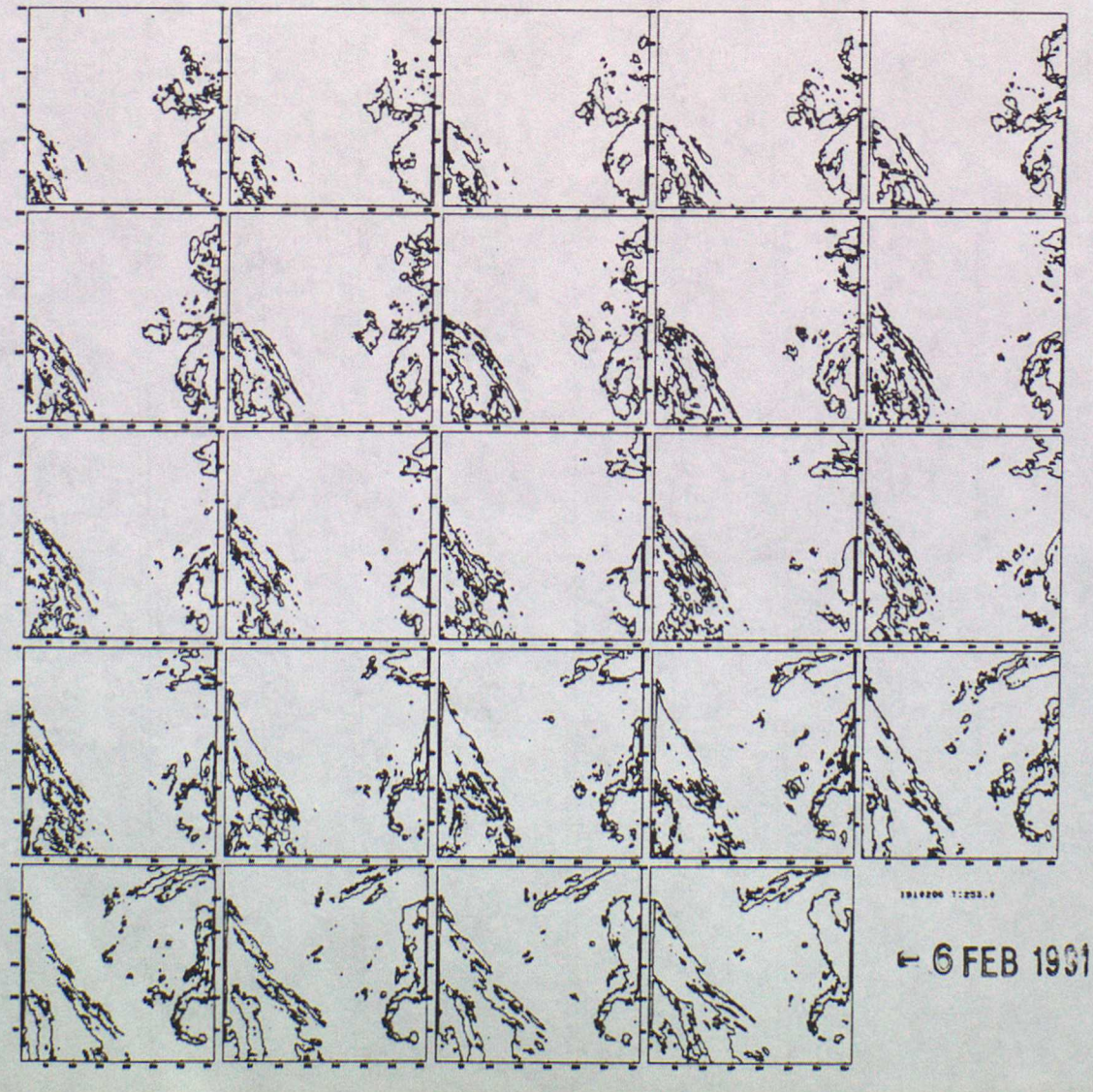

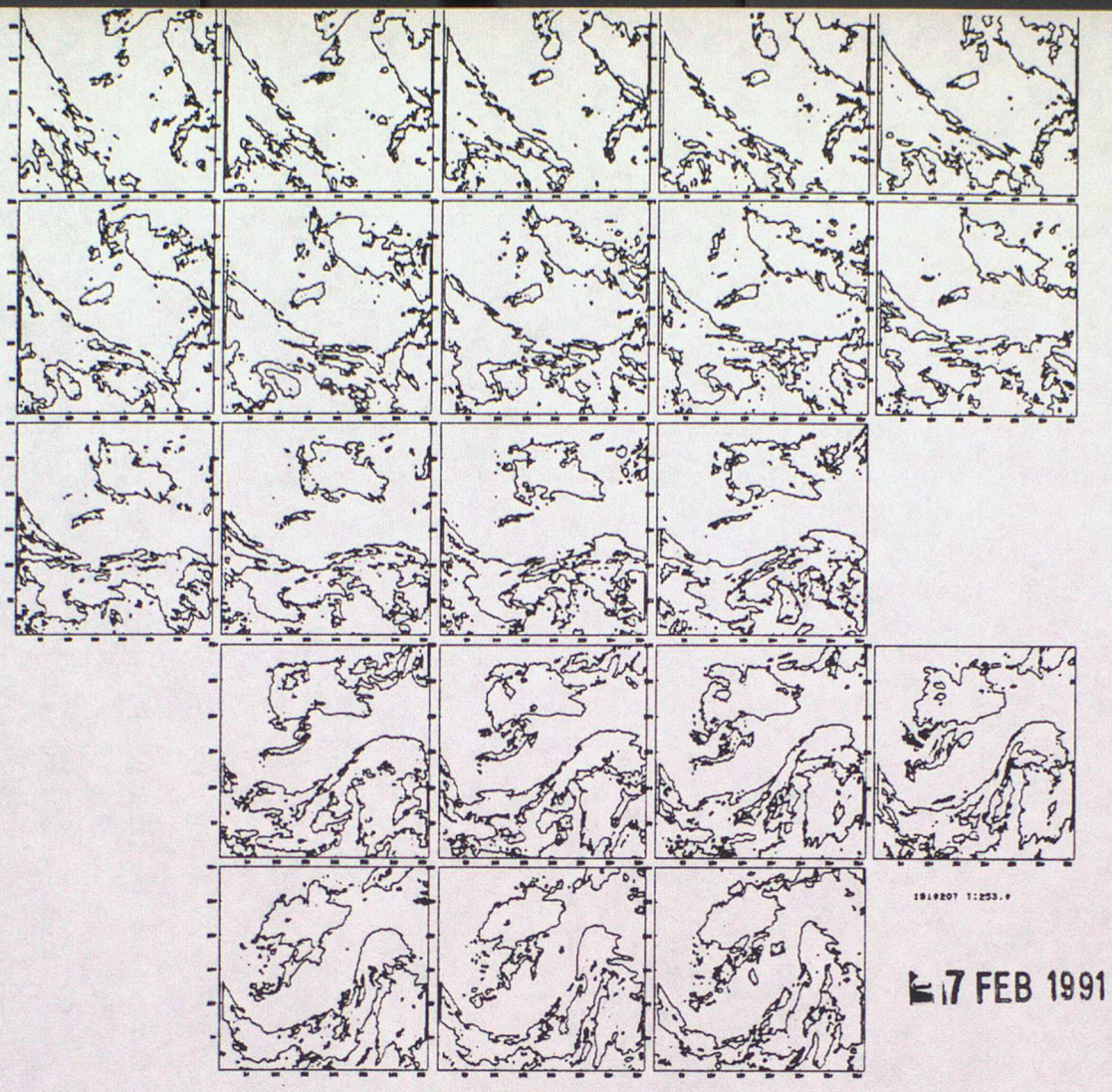


**Fig 11 Continued**

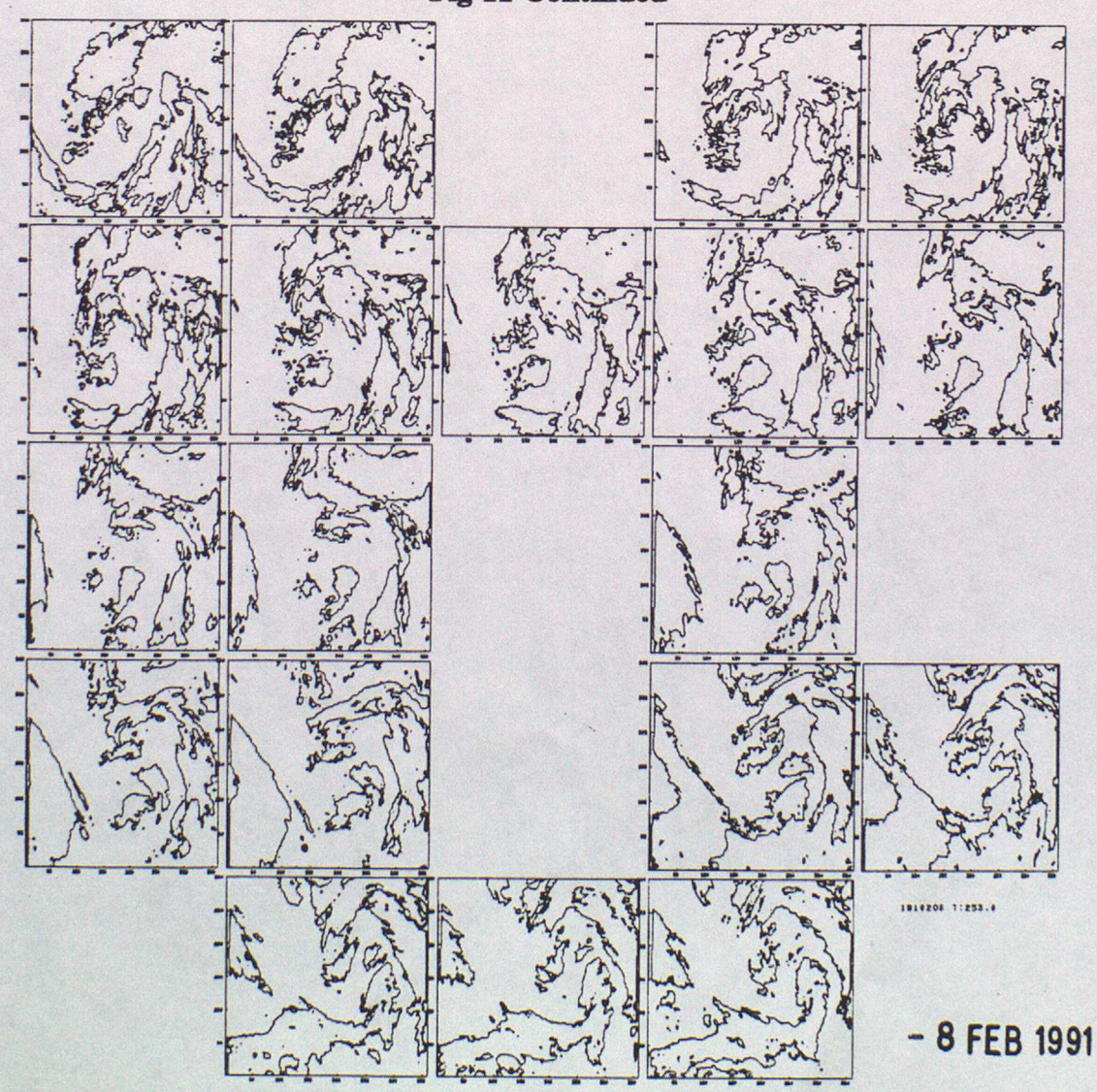

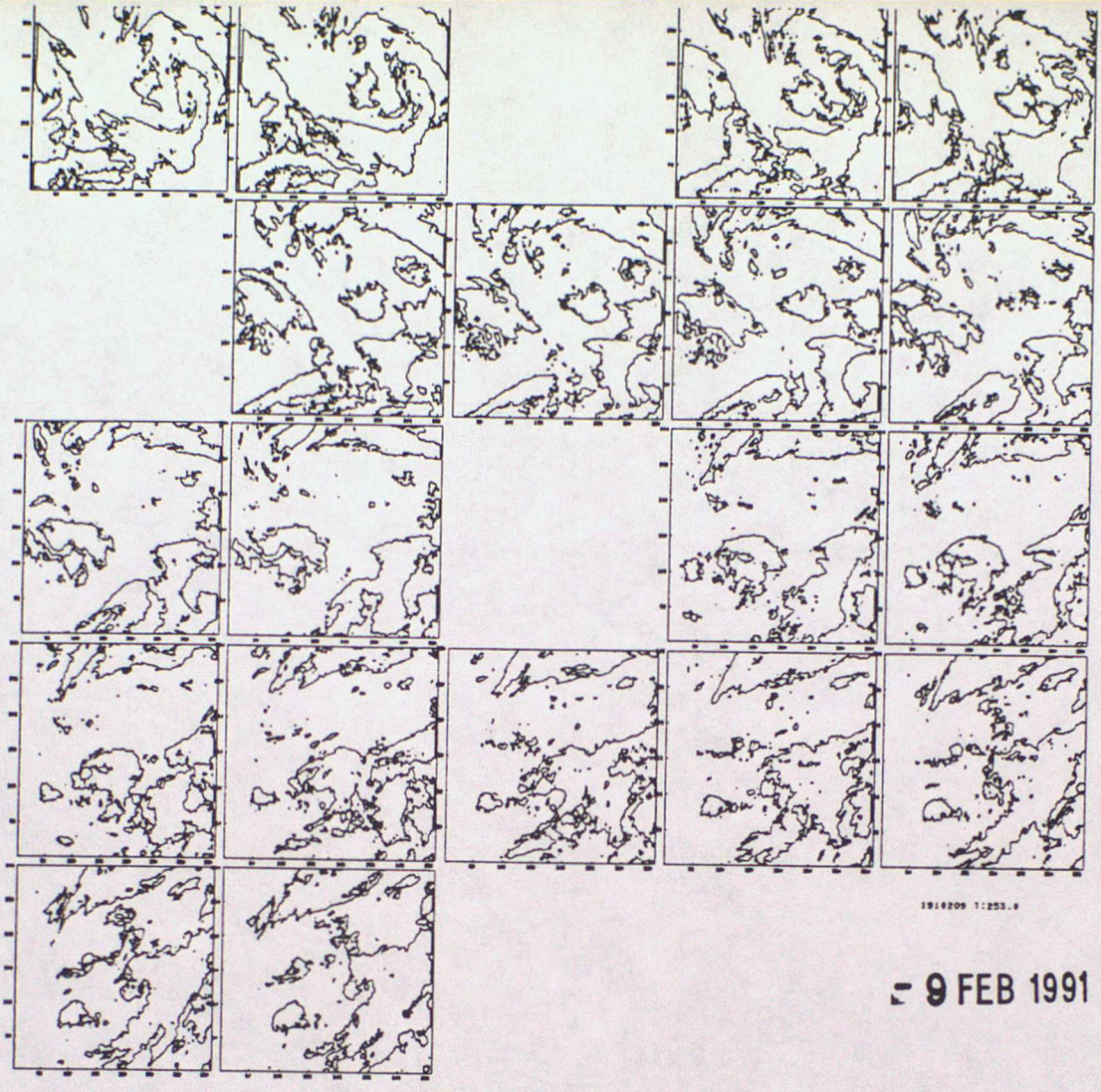


**Fig 11 Continued**

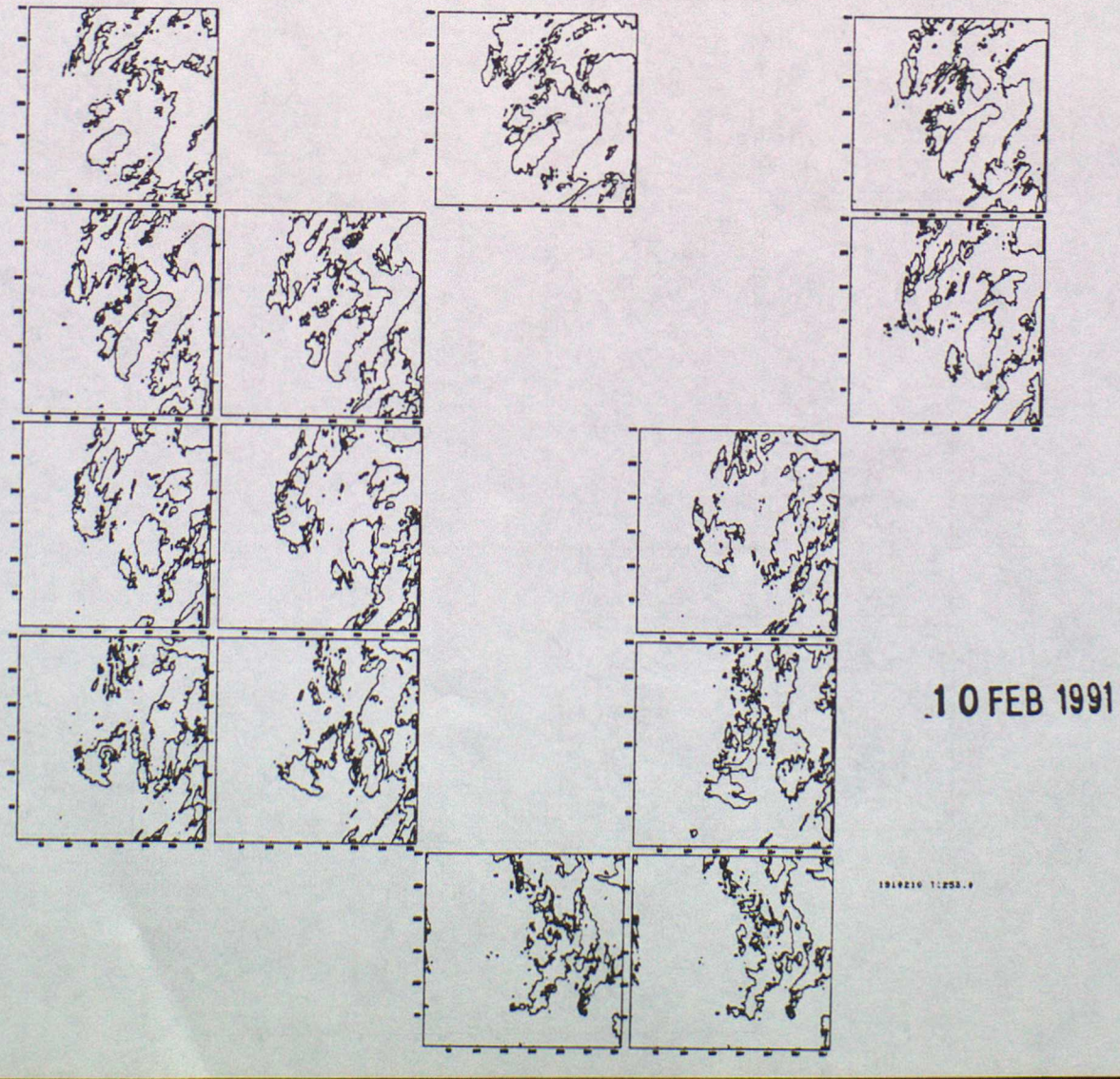

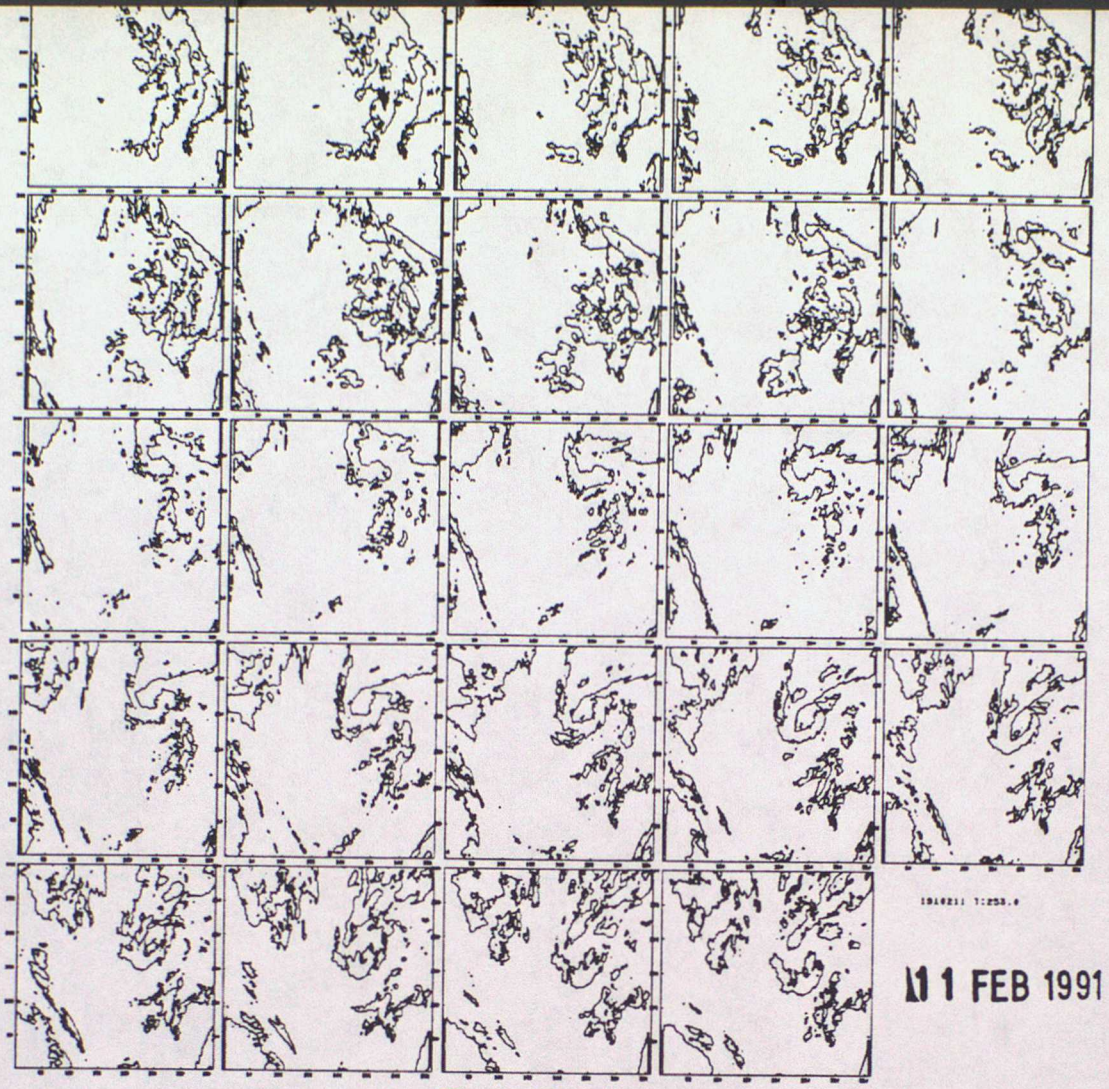


**Fig 11 Continued**

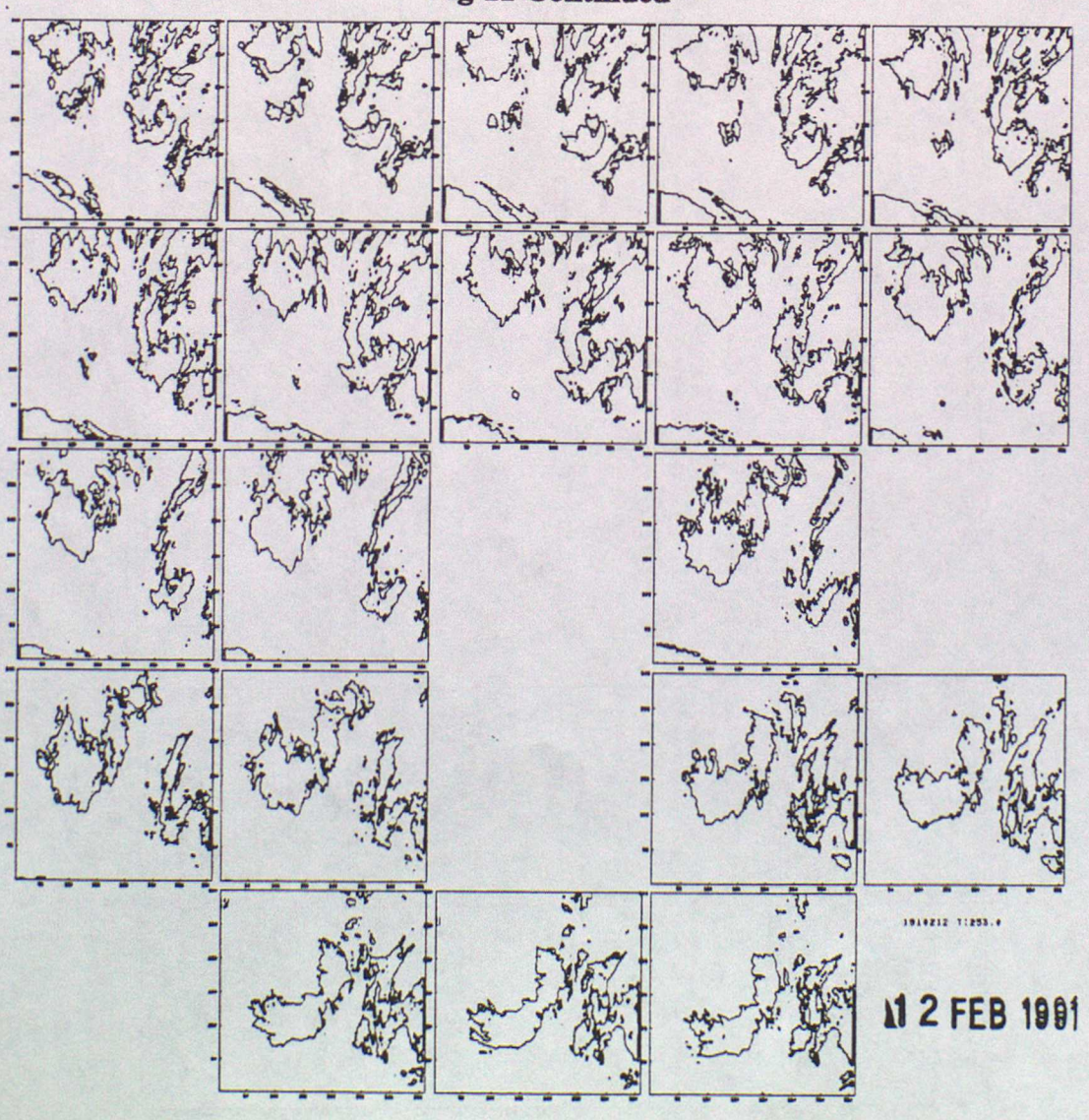

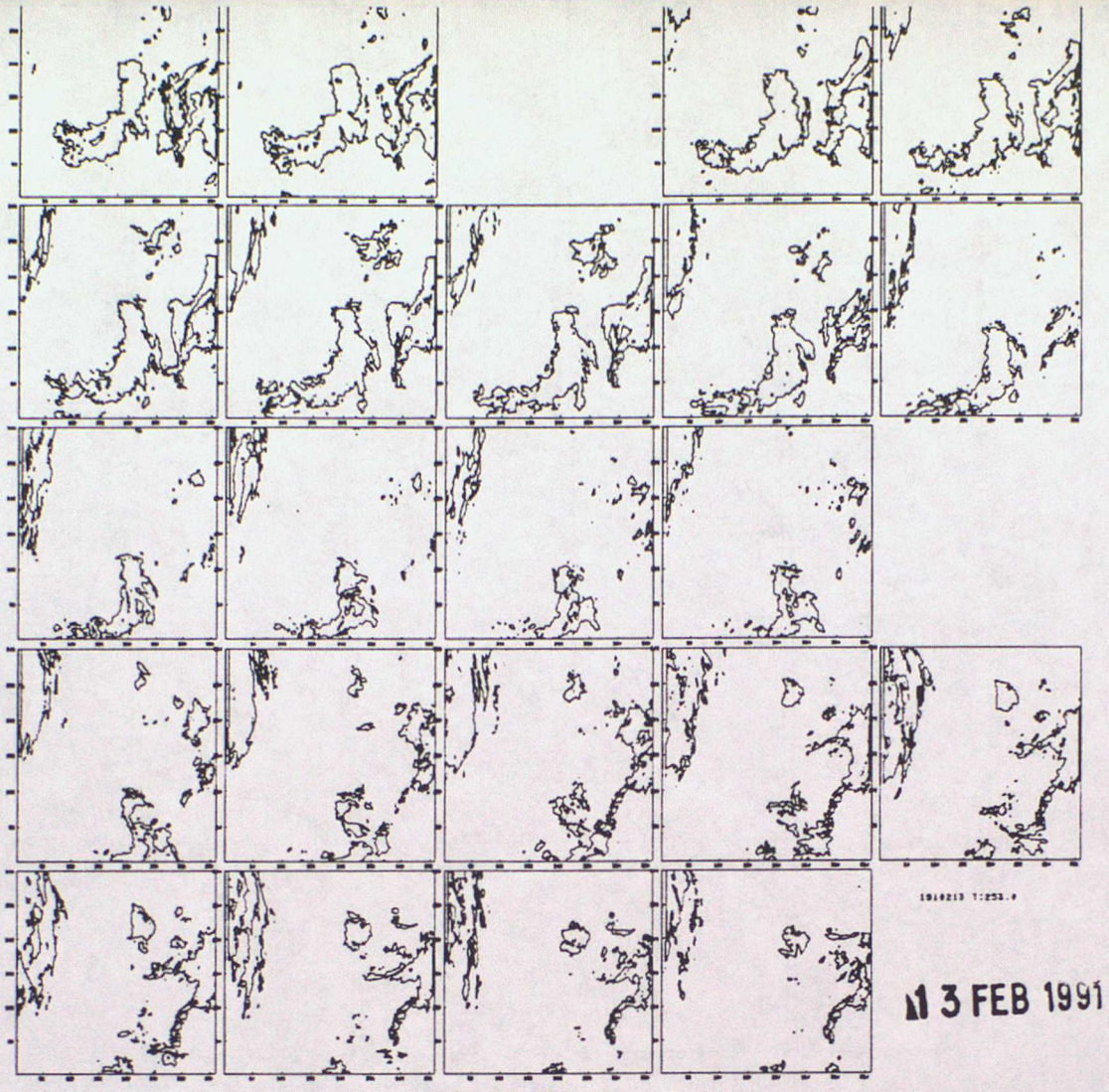


**Fig 11 Continued**

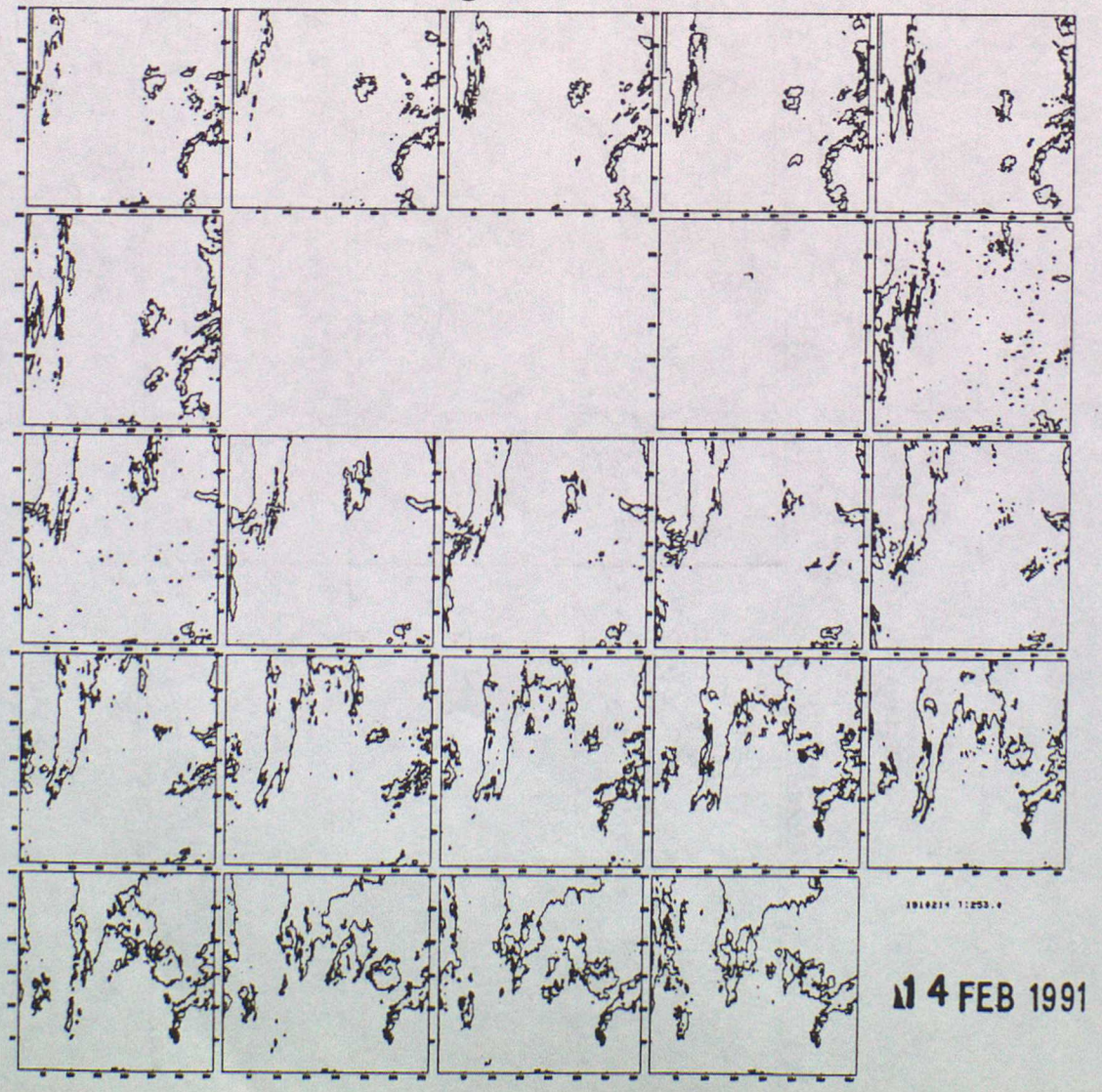

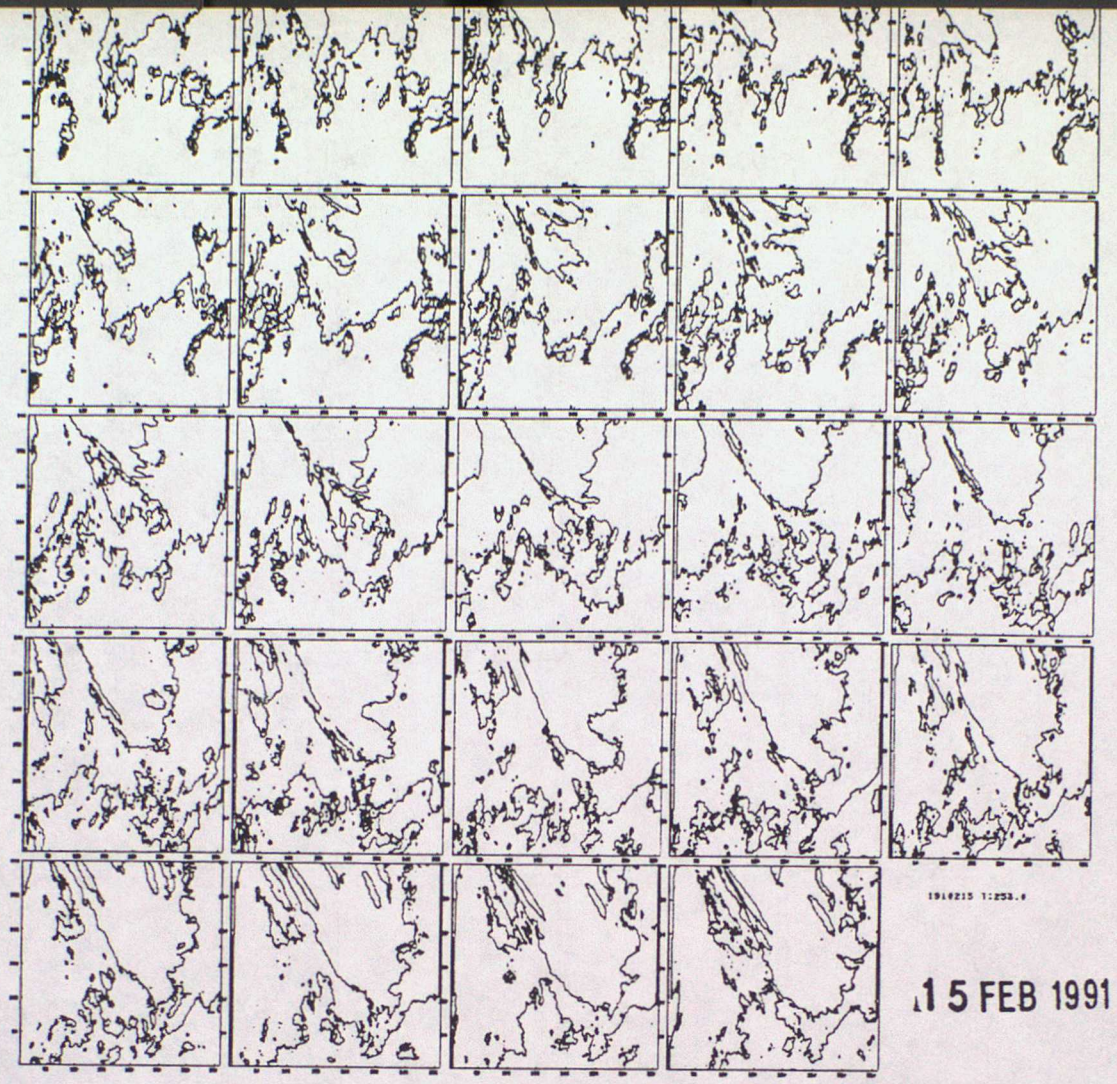


**Fig 11 Continued**

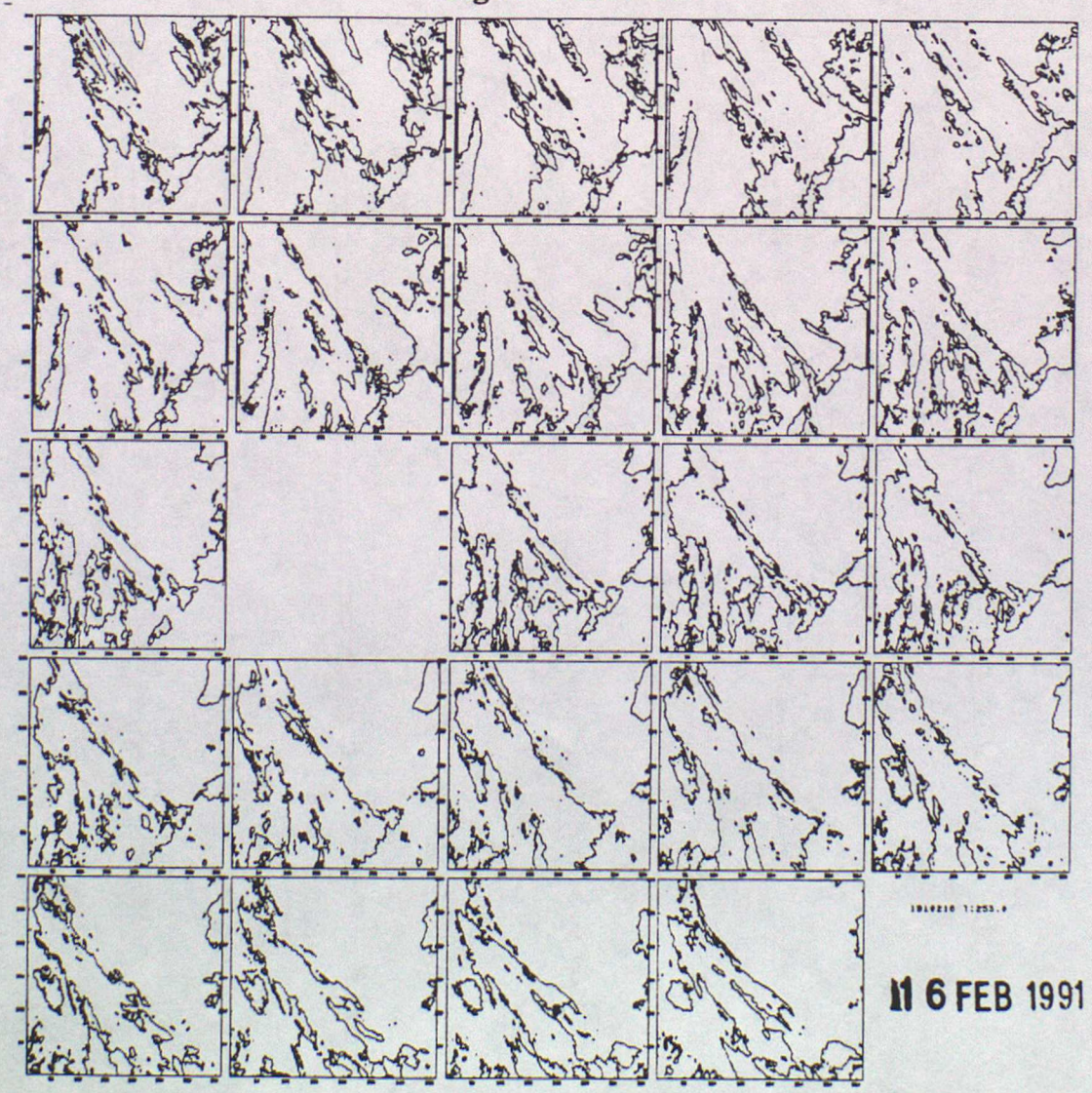

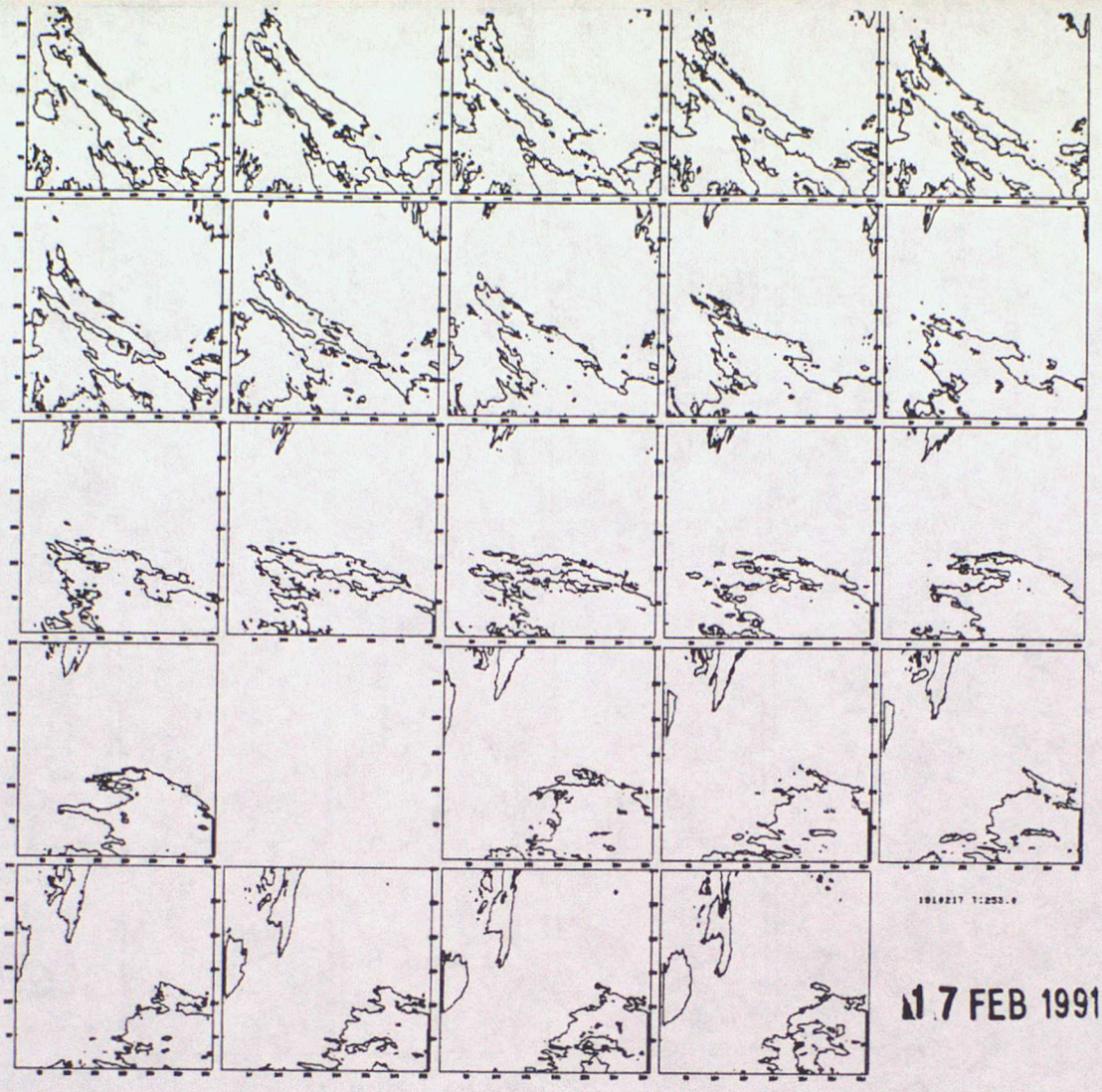


**Fig 11 Continued**

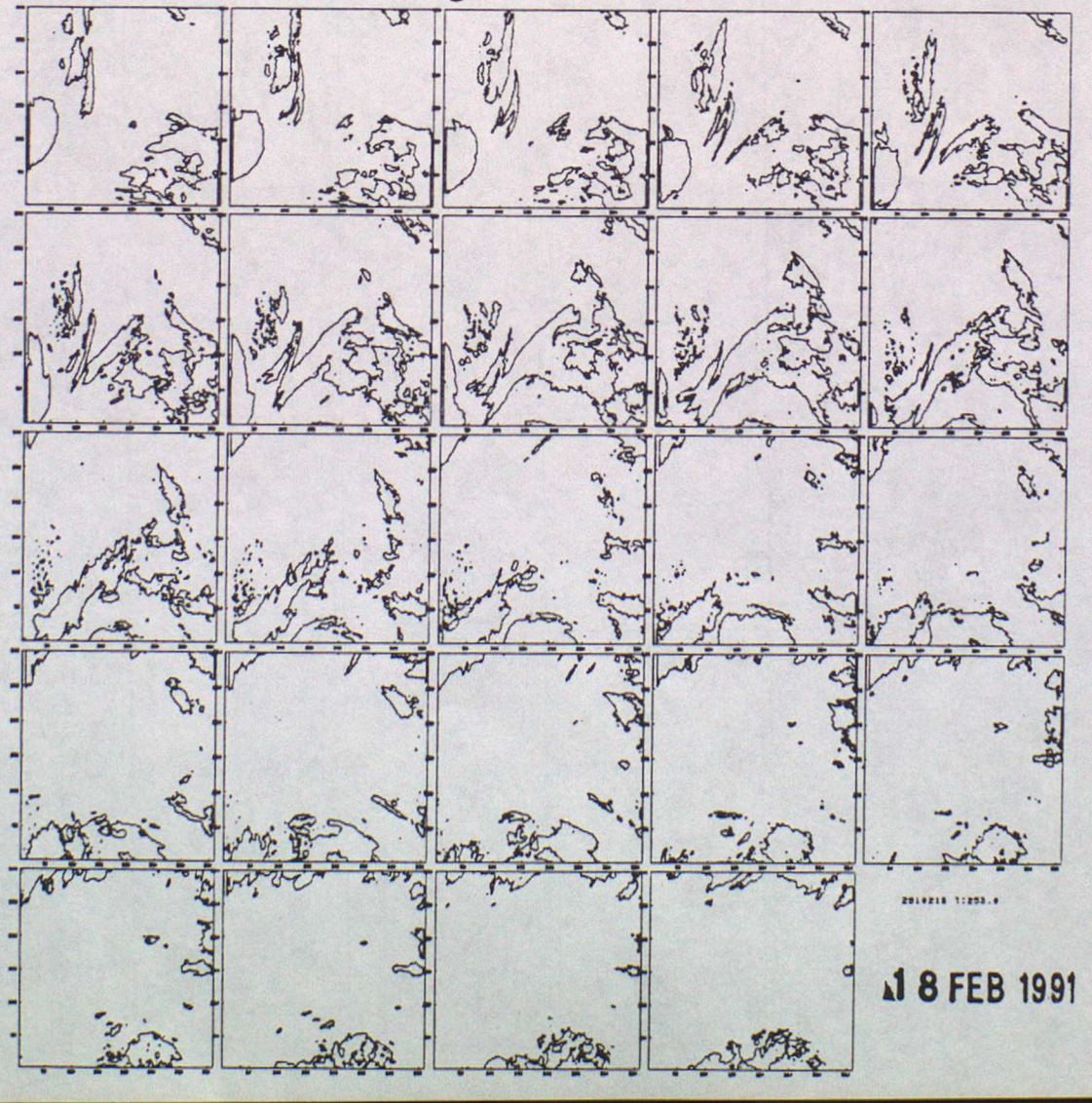

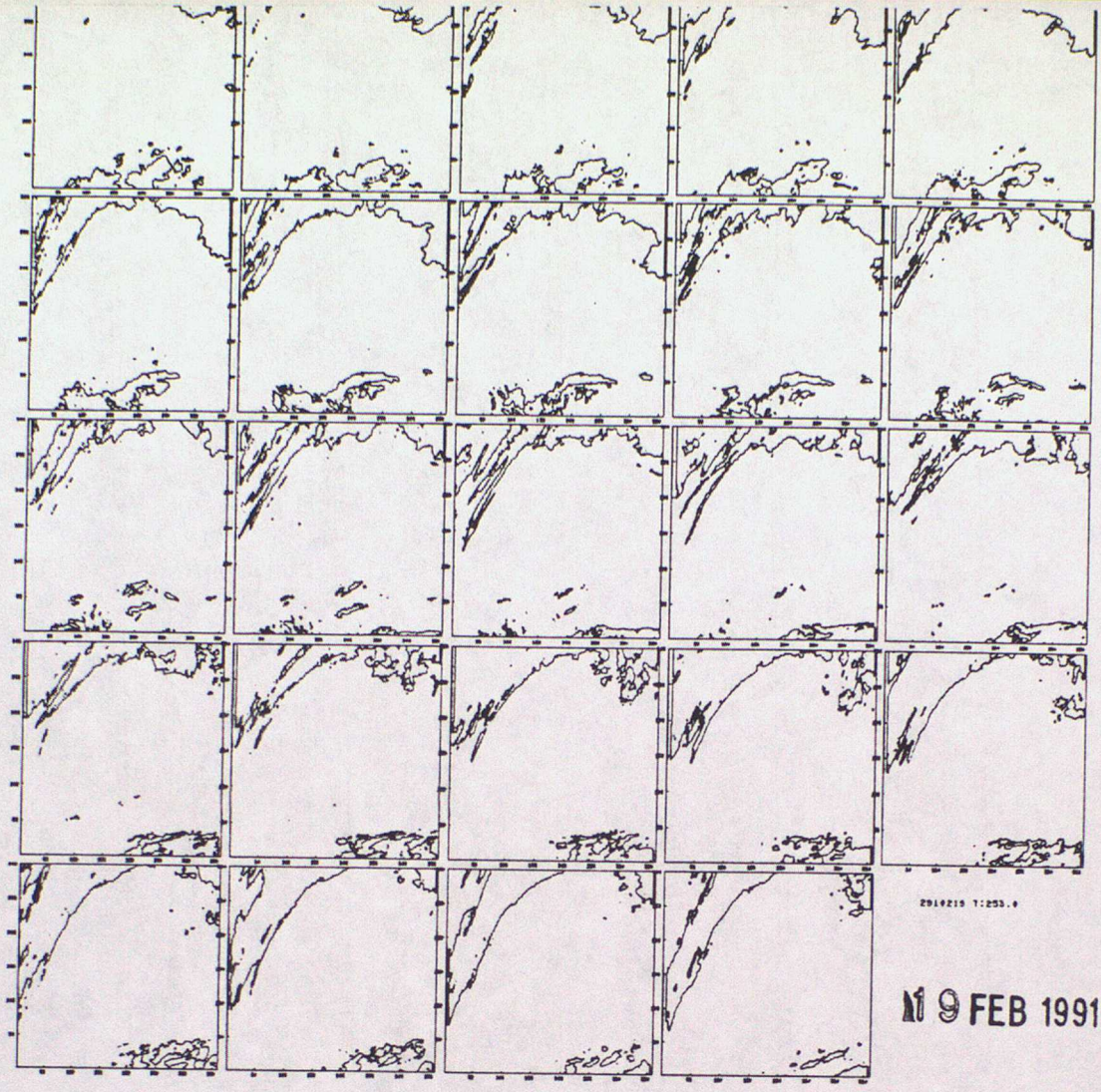


**Fig 11 Continued**

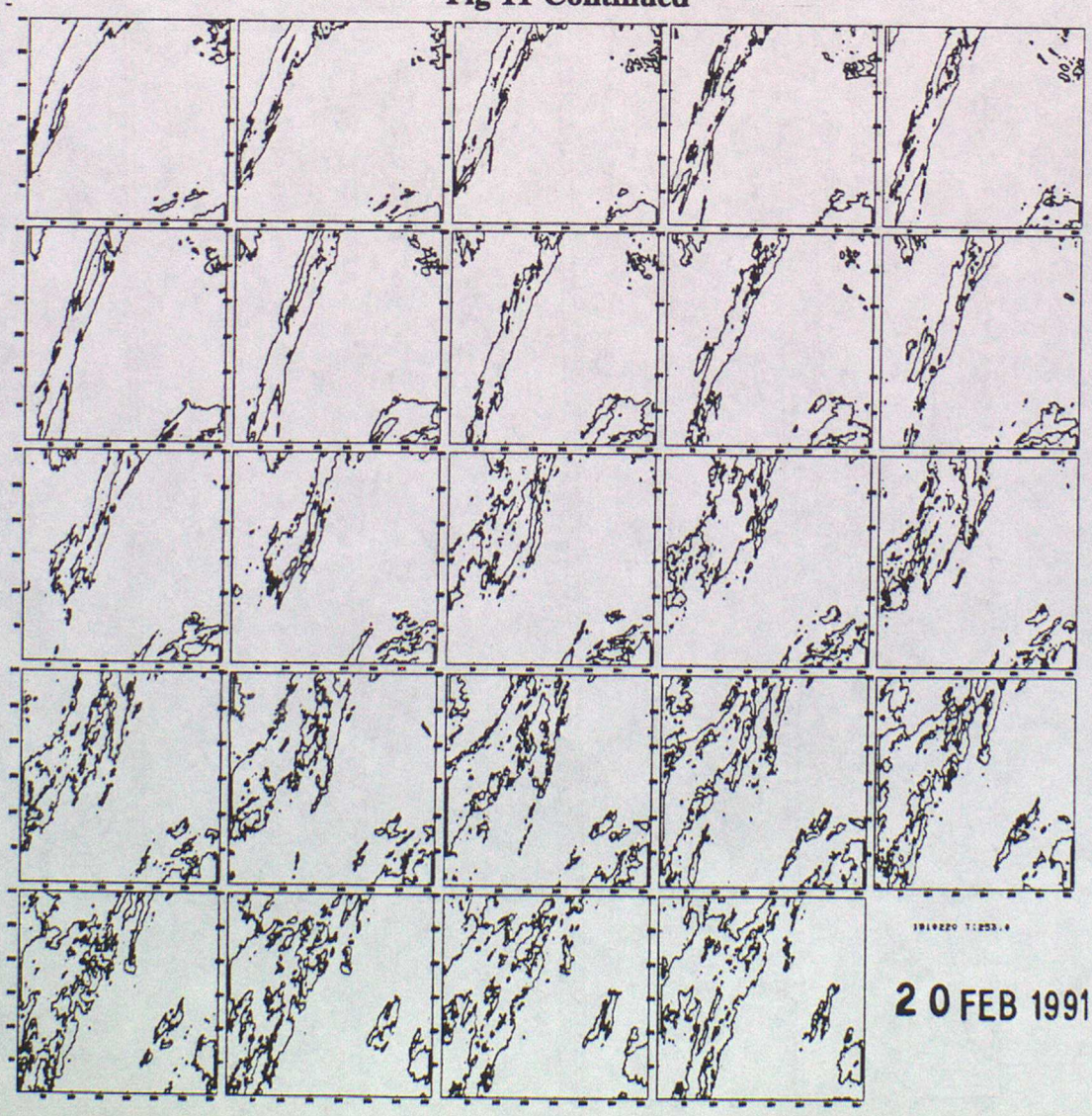

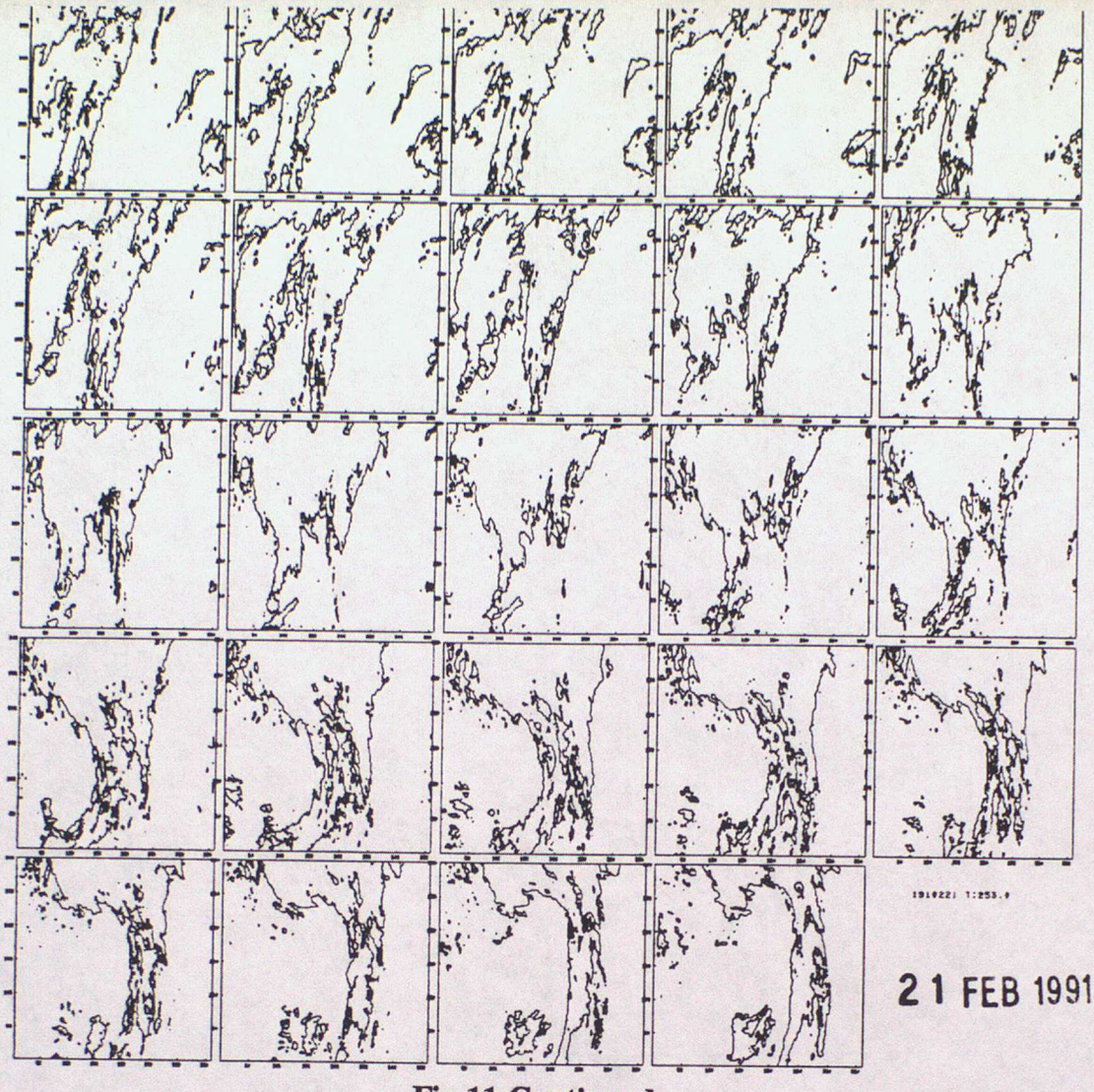


**Fig 11 Continued**

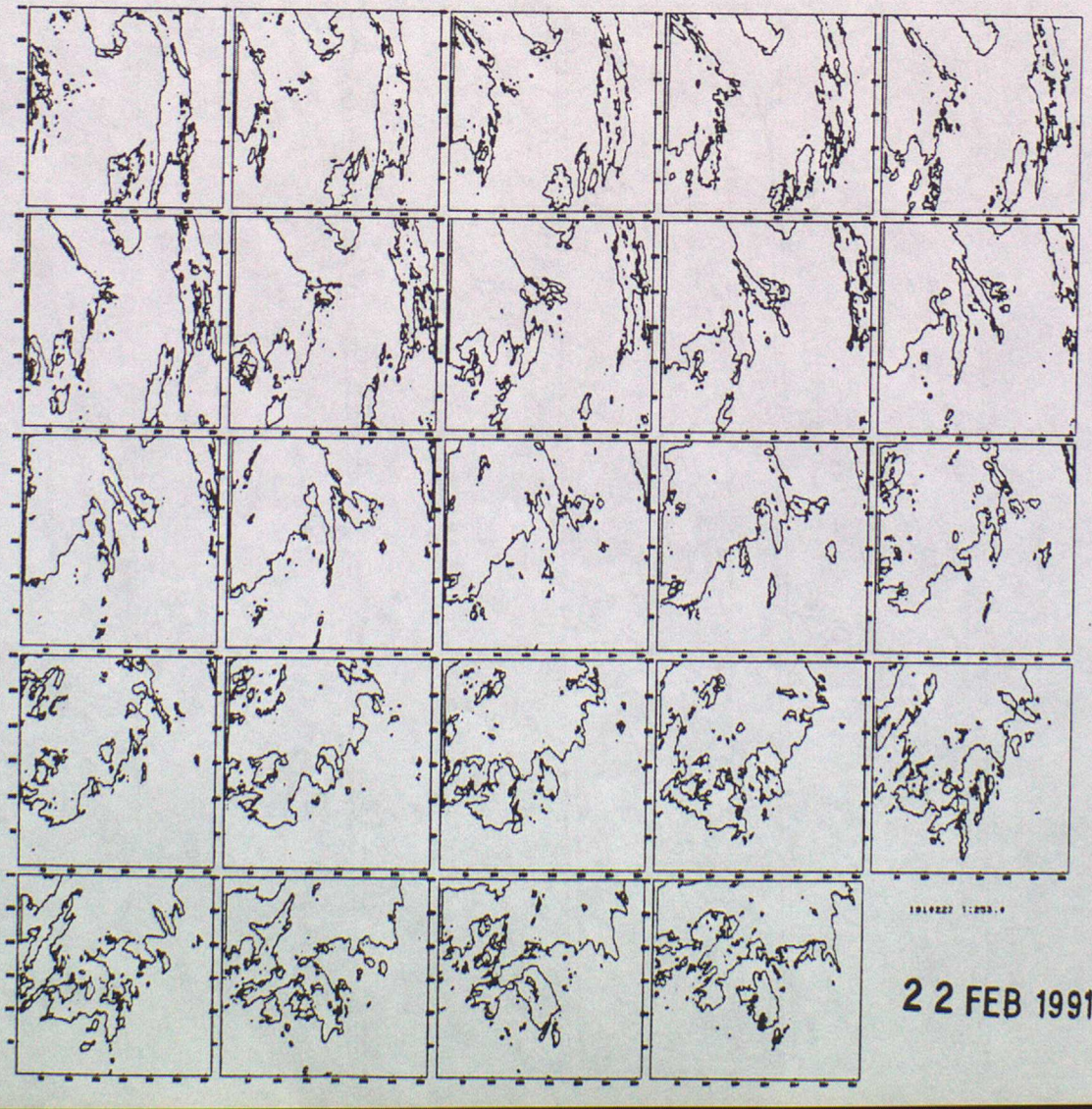

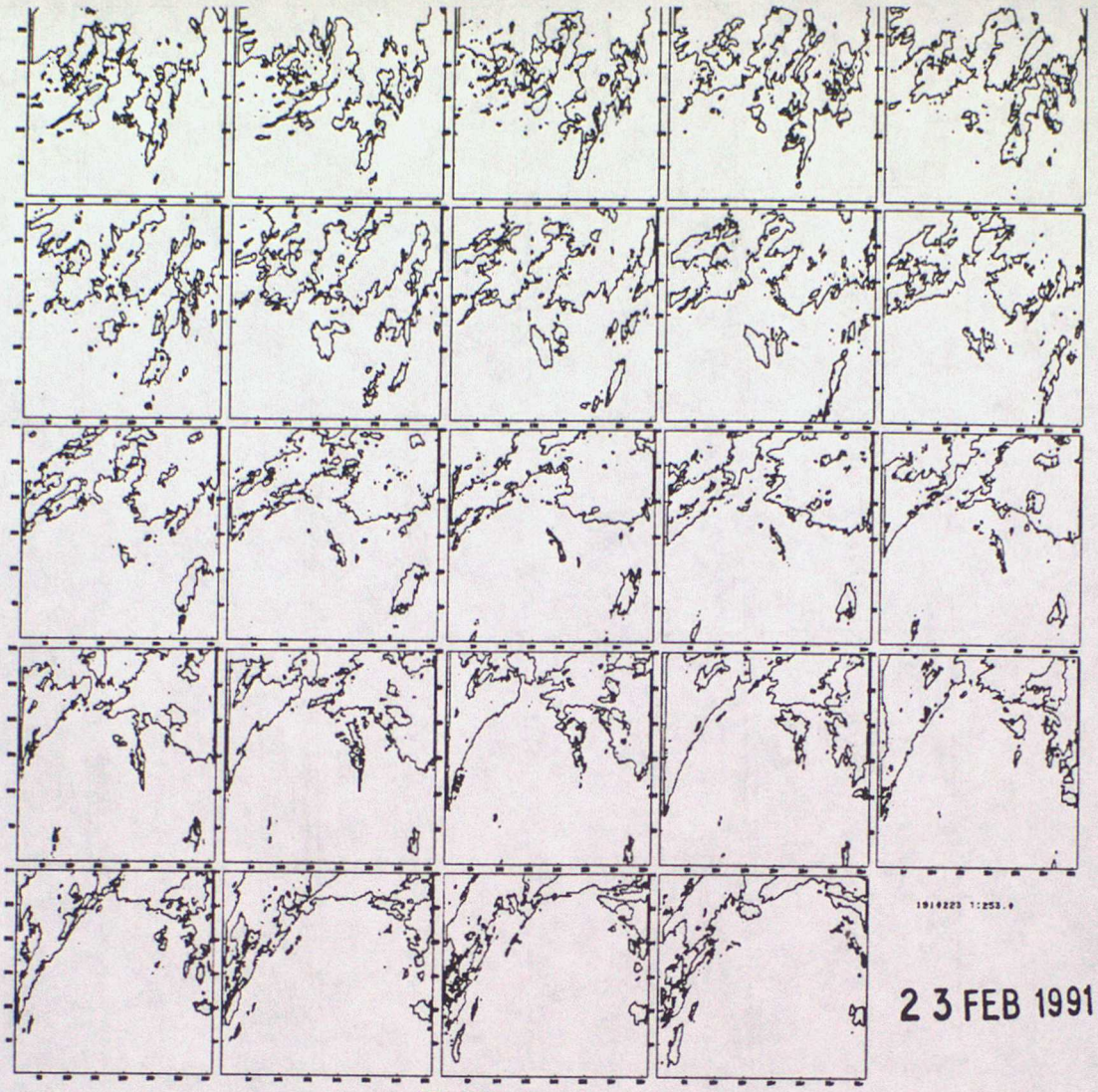


**Fig 11 Continued**

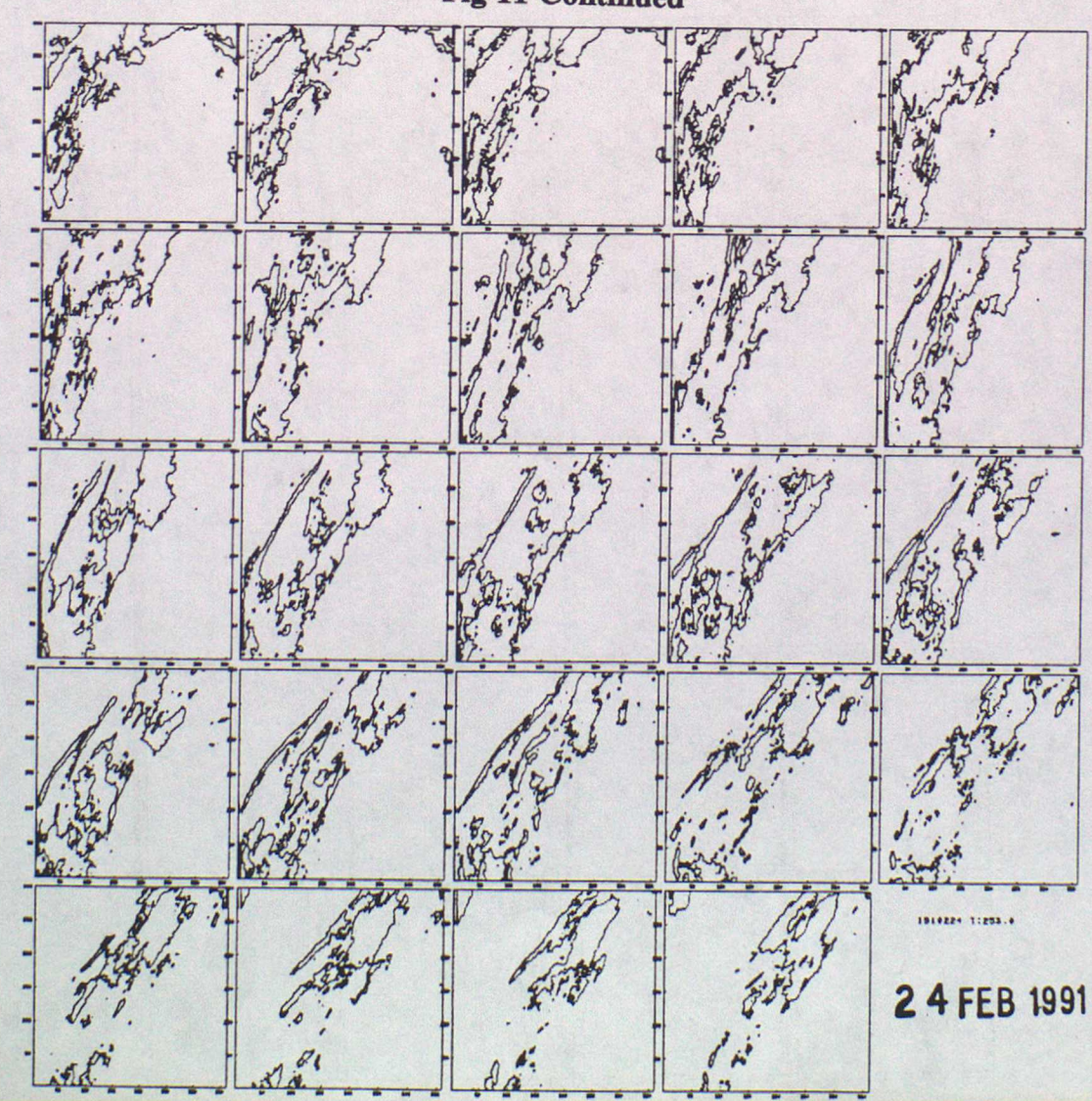

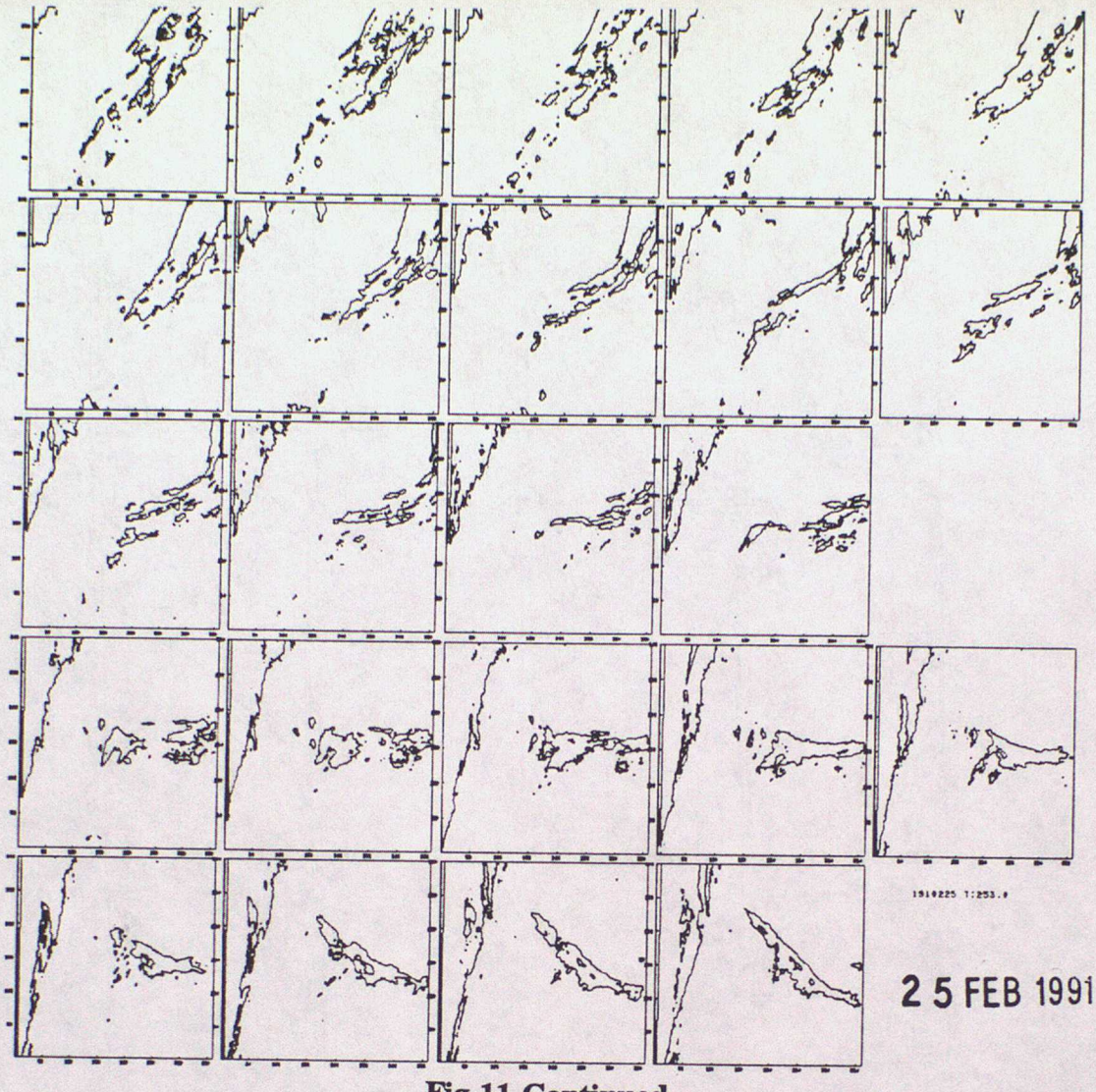


**Fig 11 Continued**

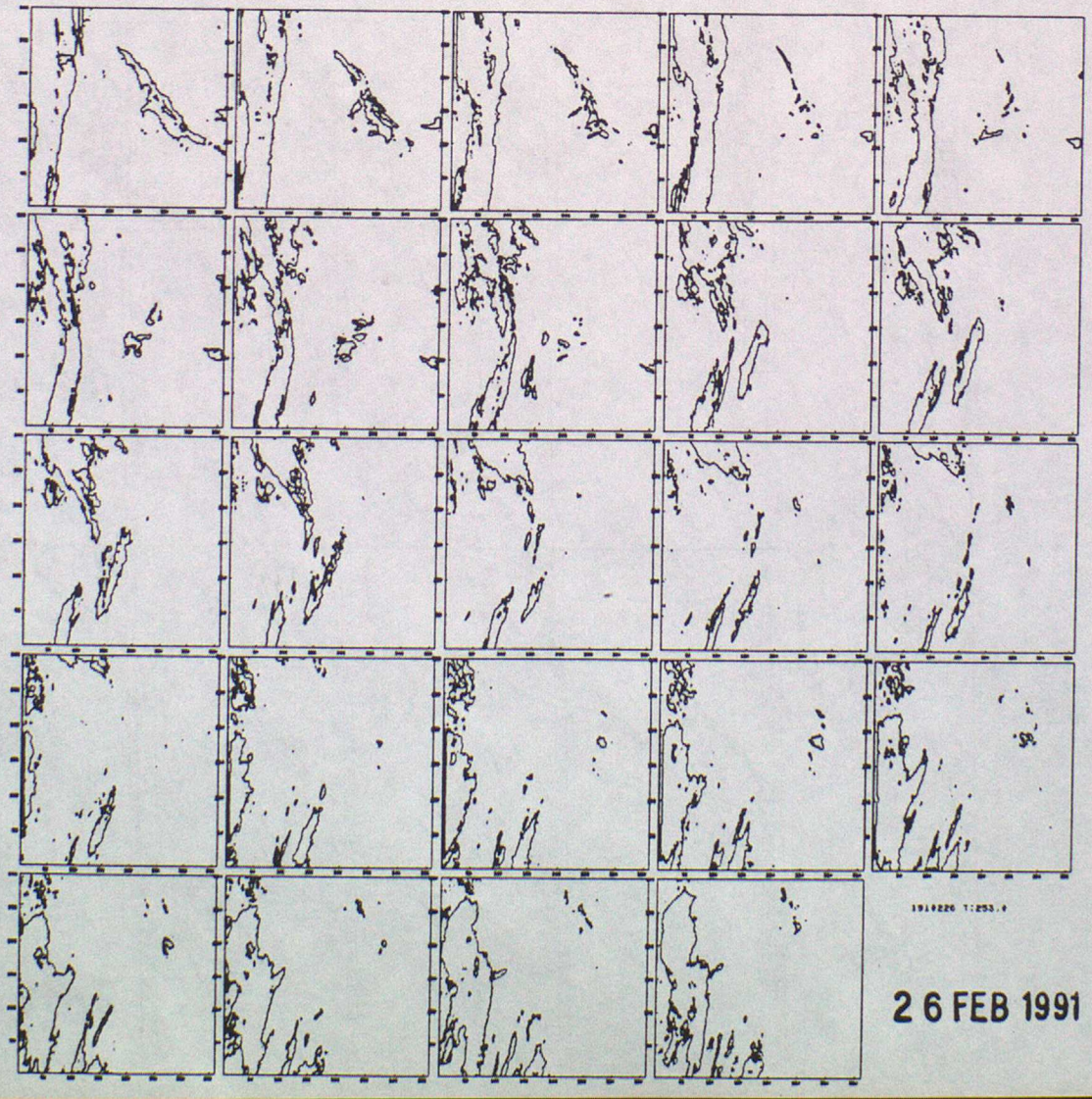

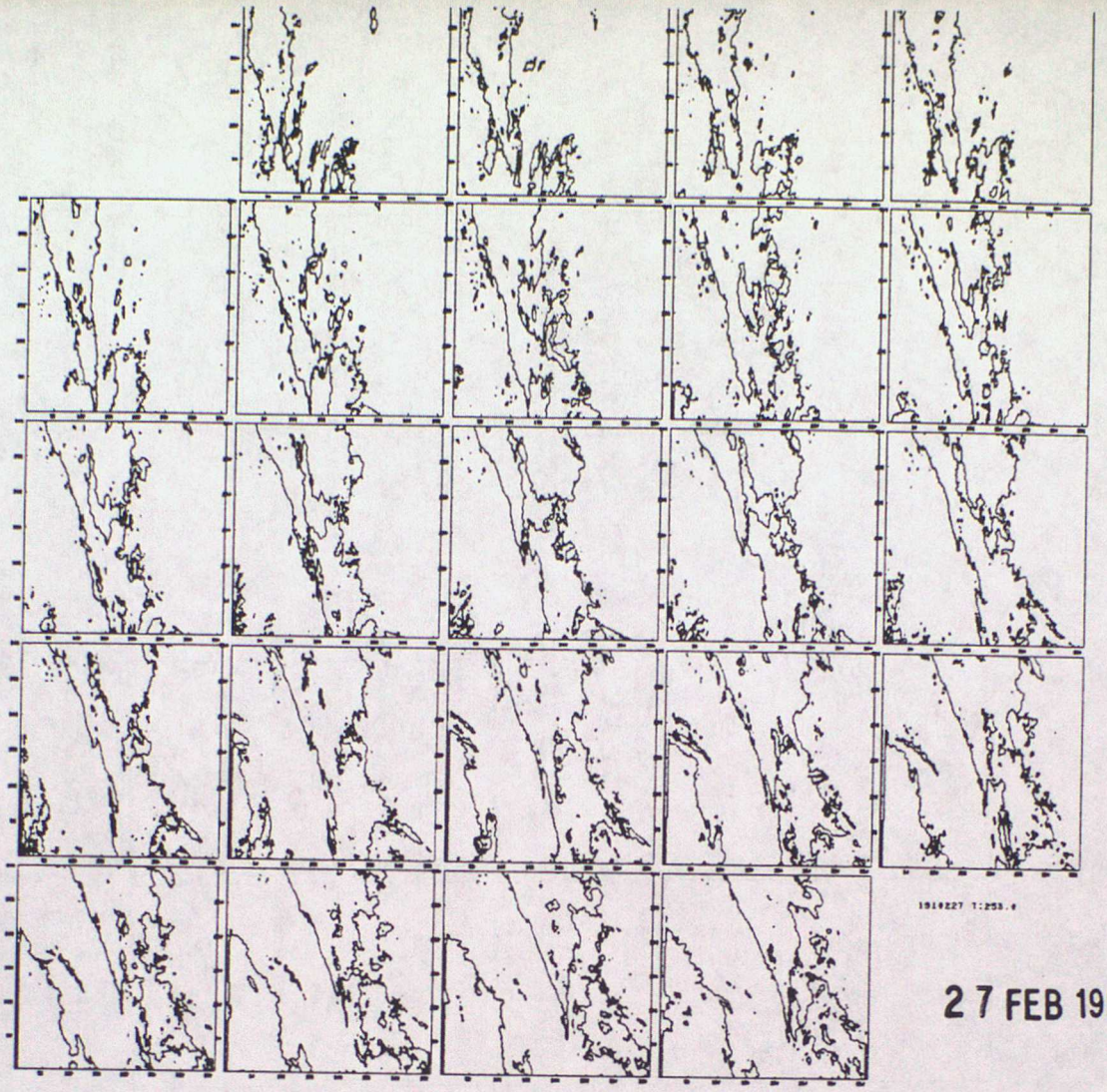


**Fig 11 Continued**

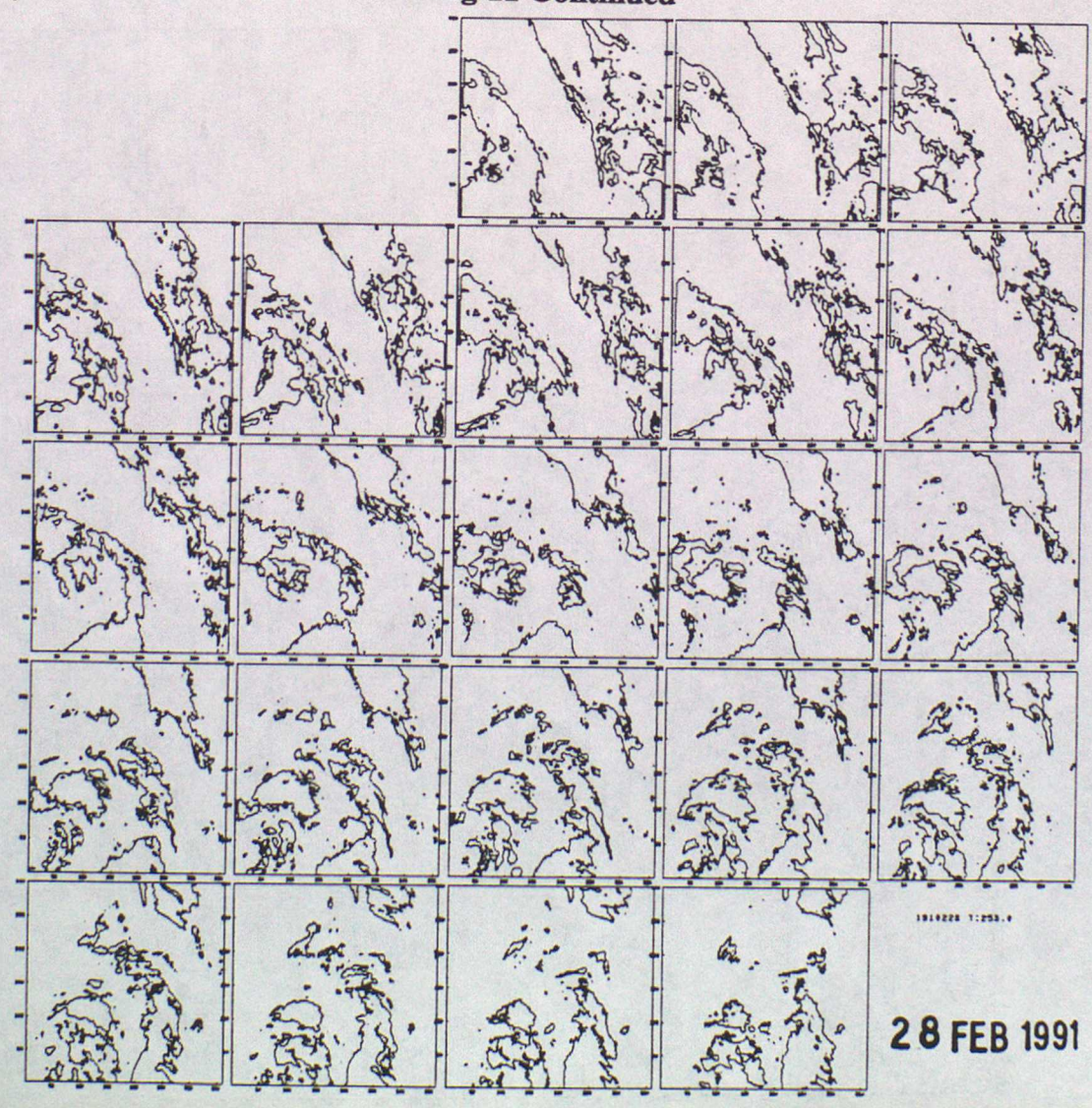

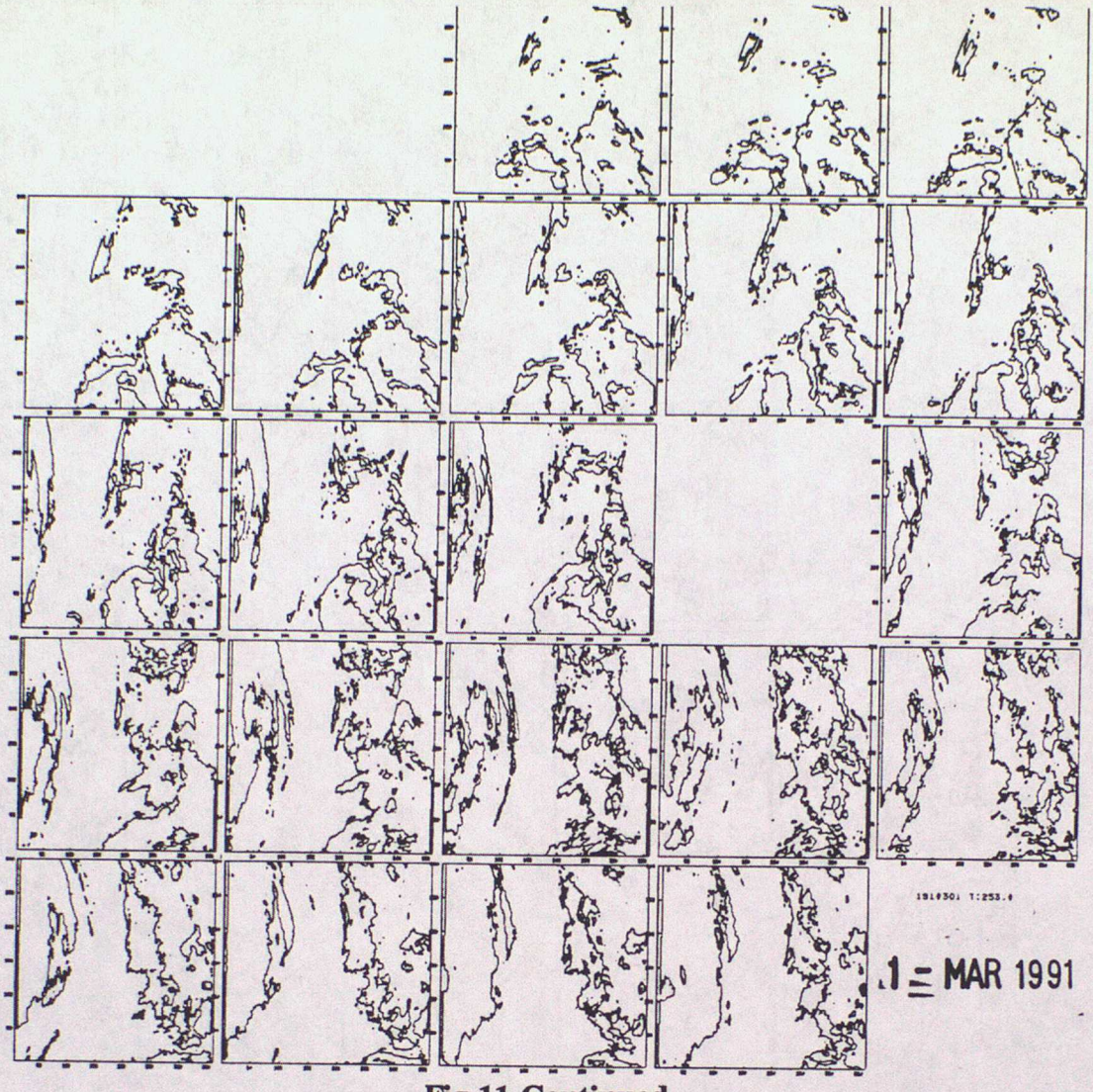


**Fig 11 Continued**

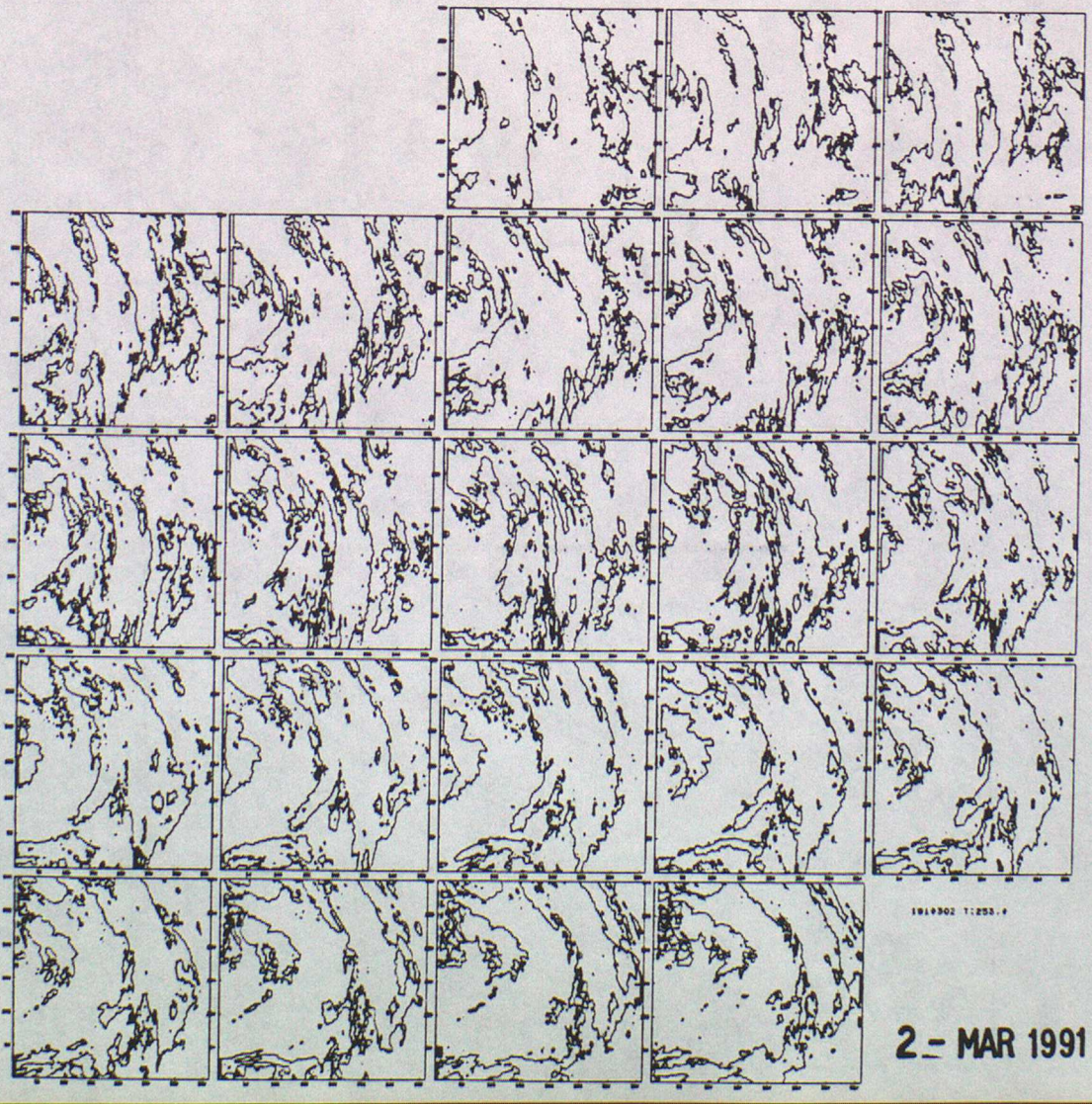

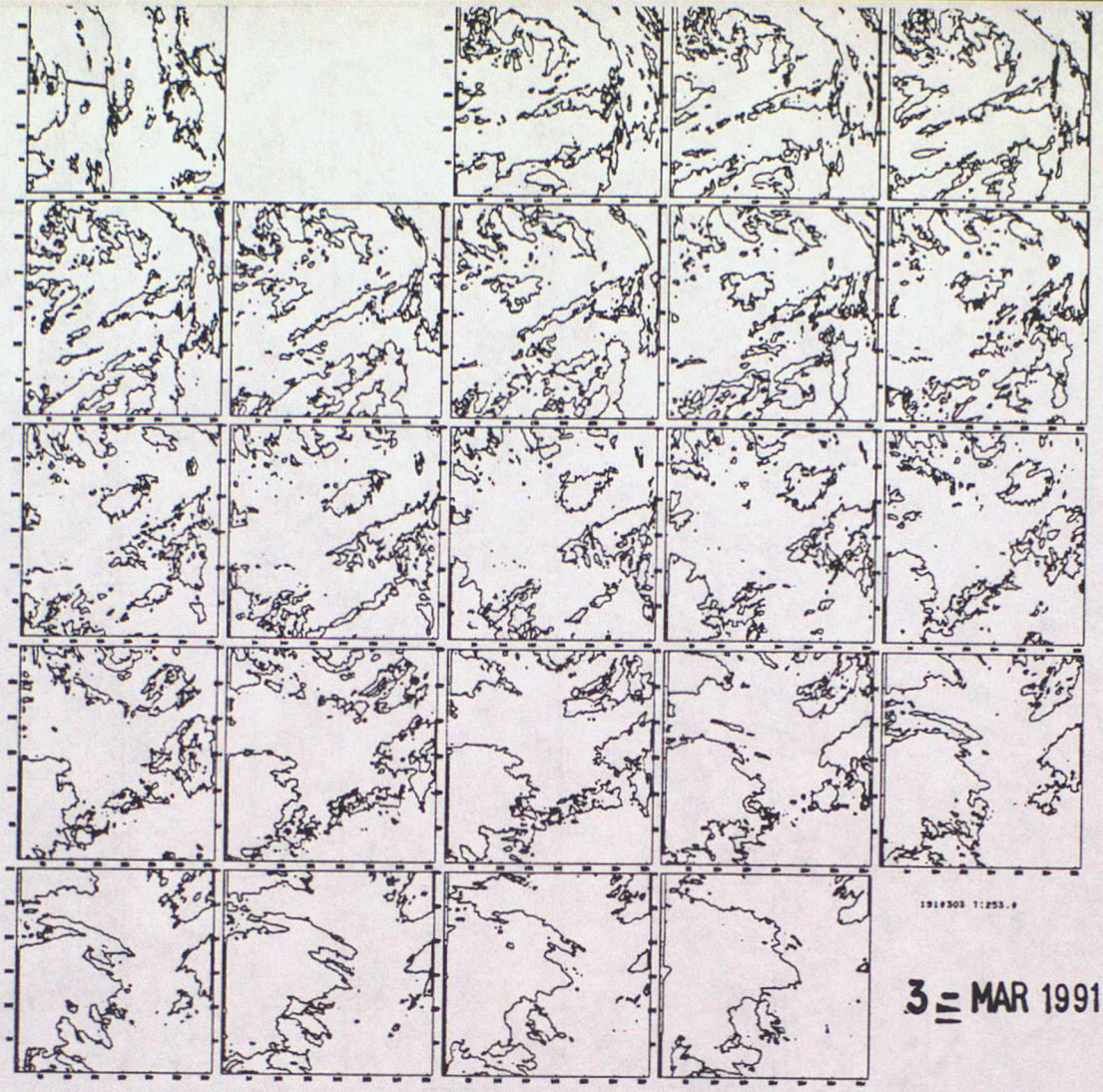


**Fig 11 Continued**

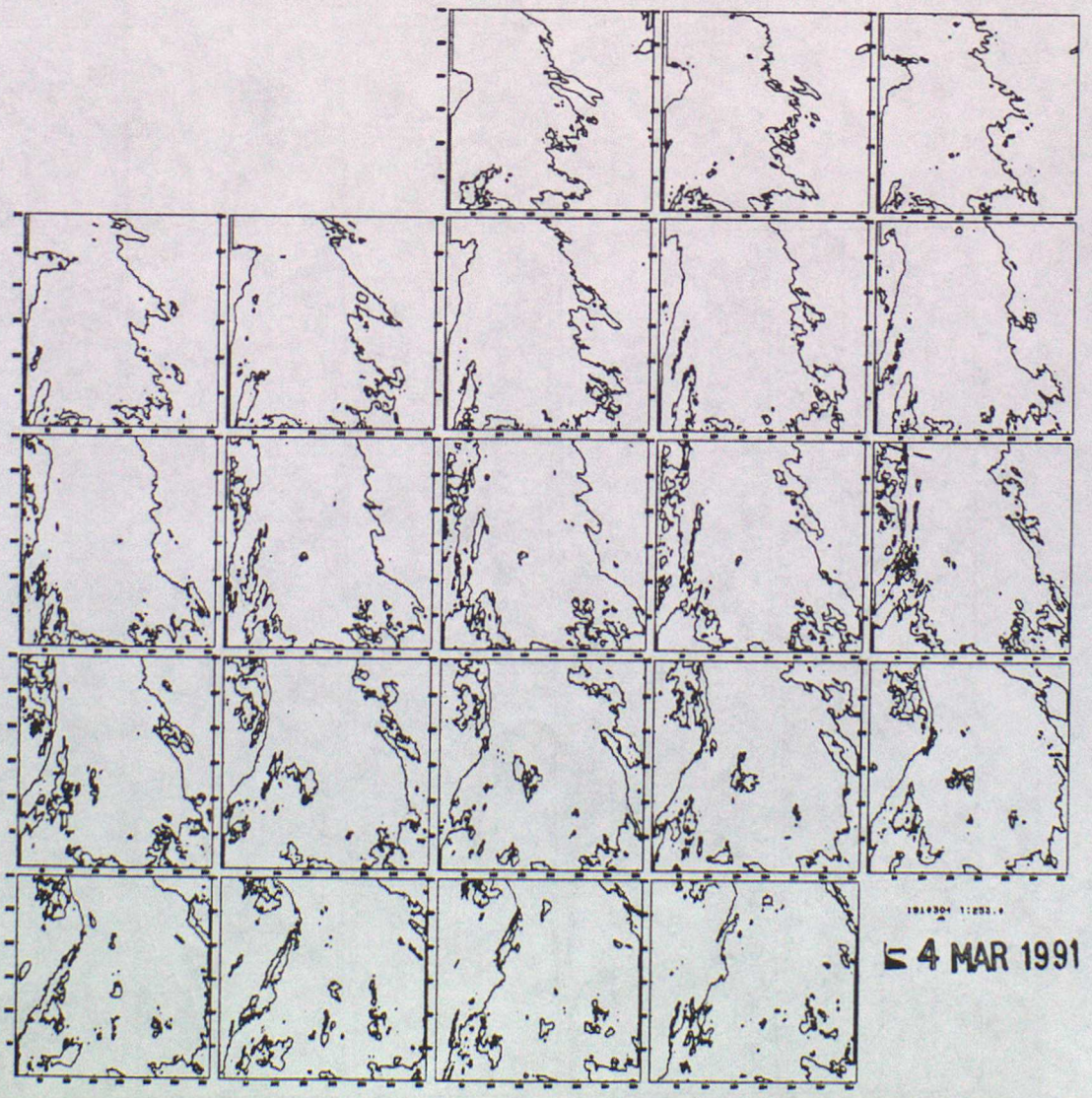

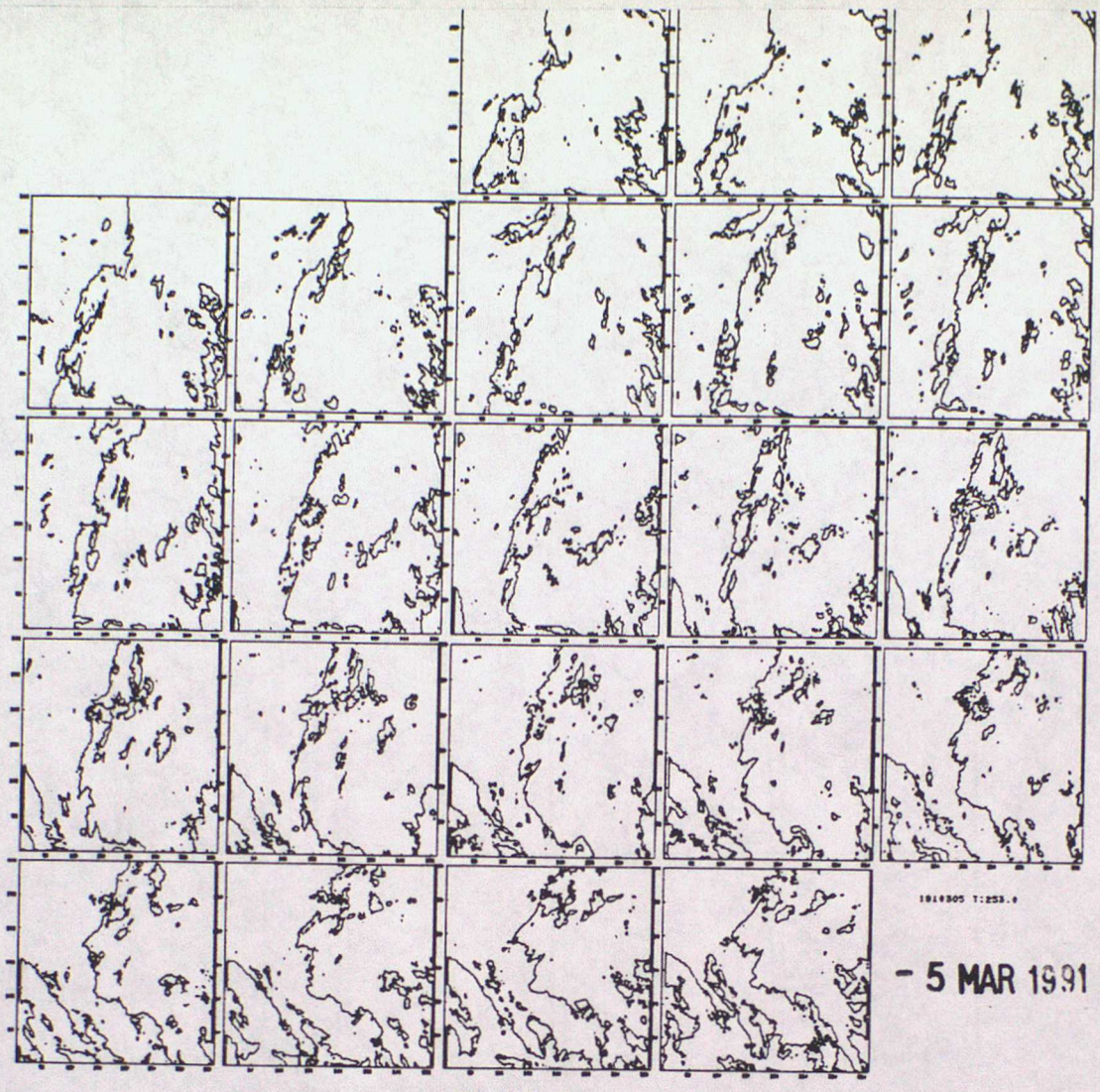


**Fig 11 Continued**

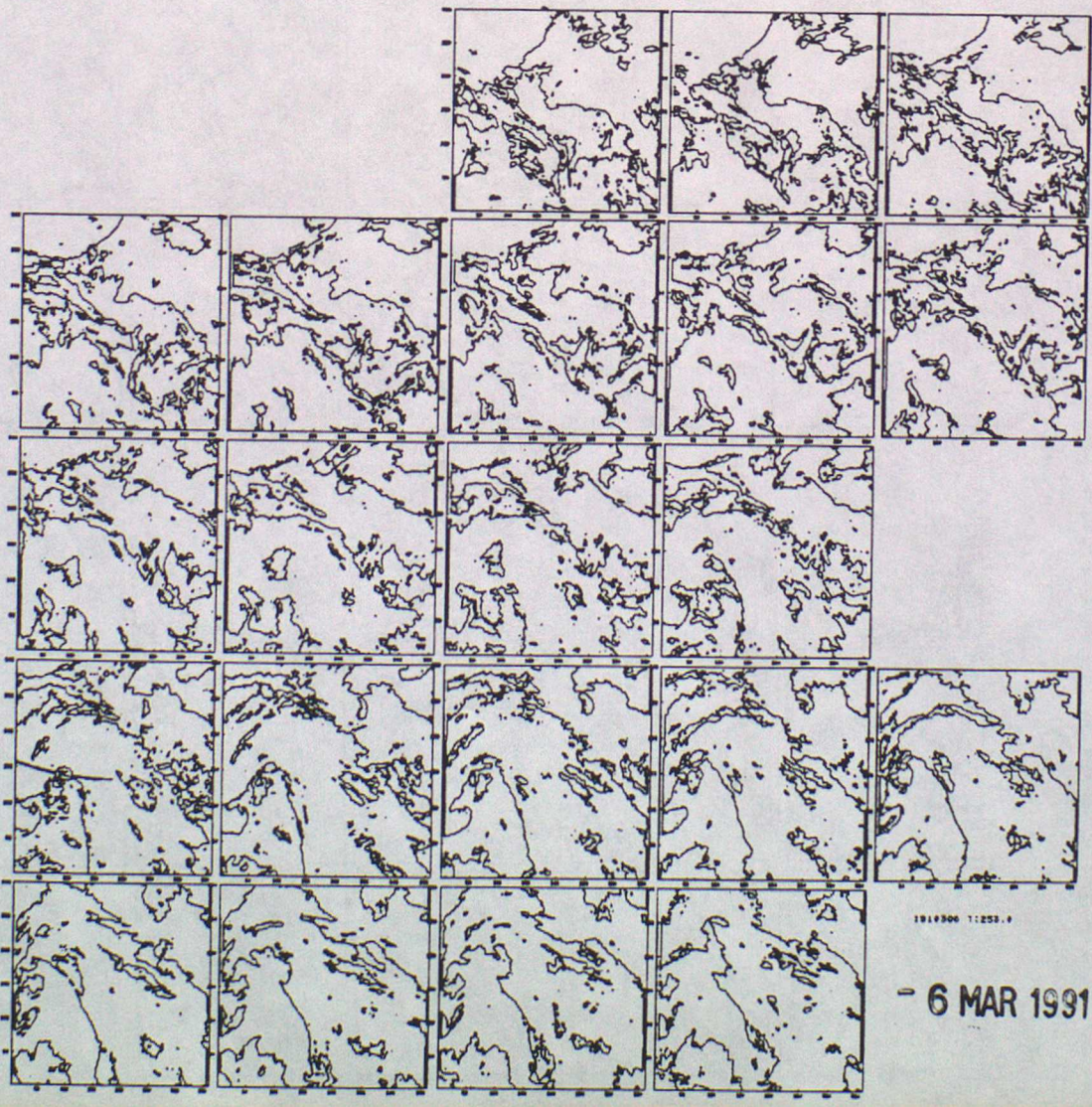

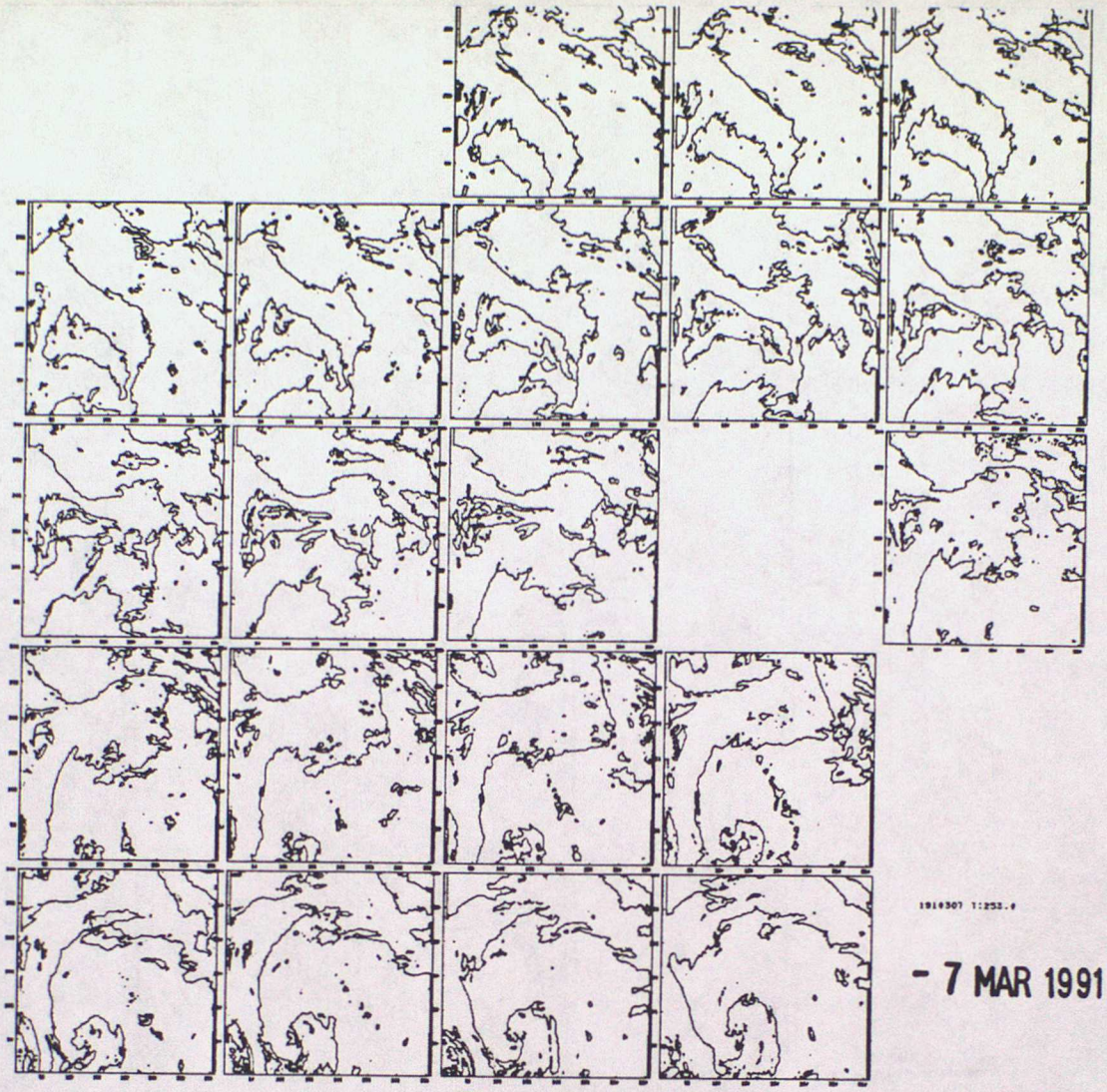


**Fig 11 Continued**

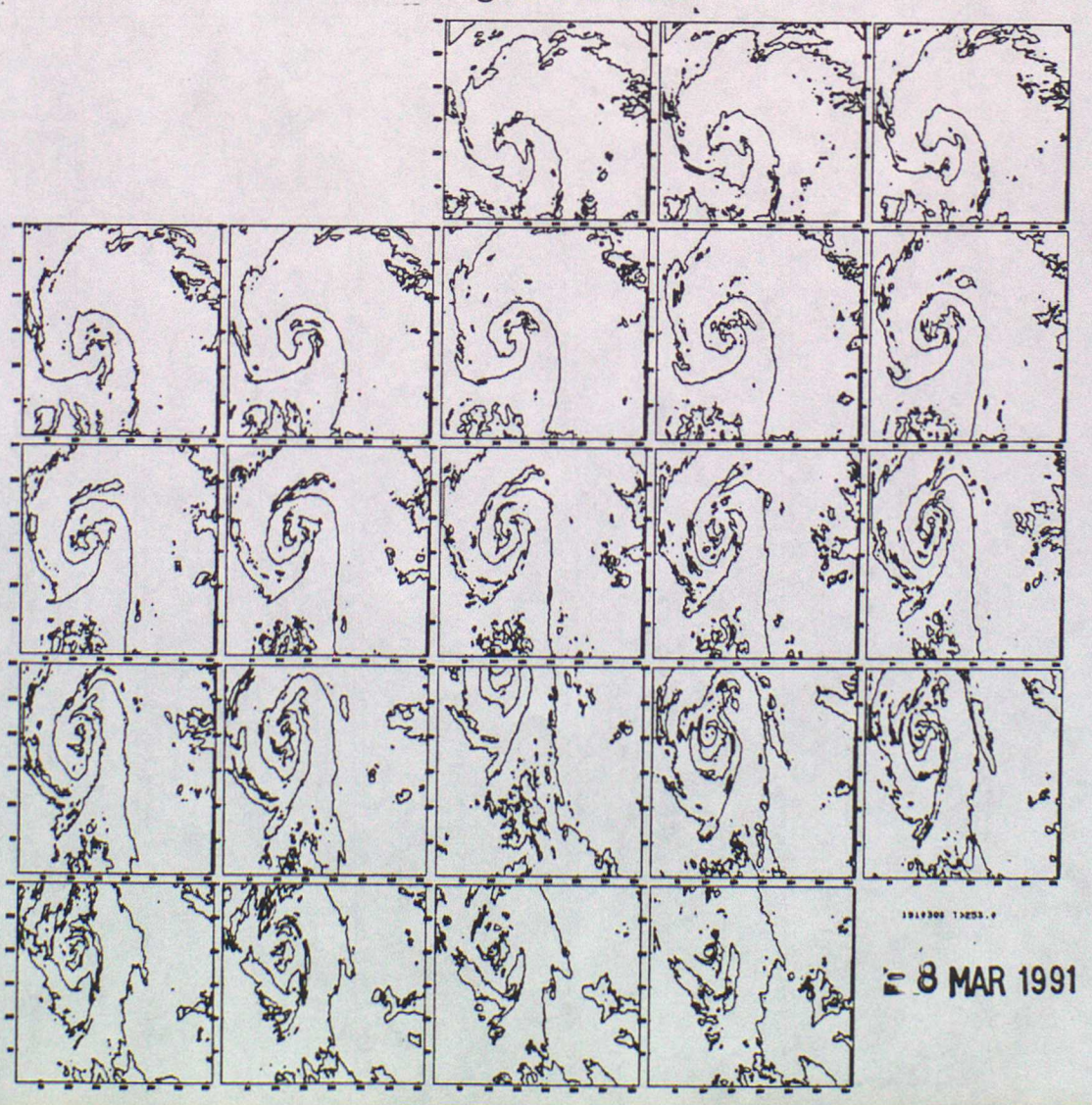

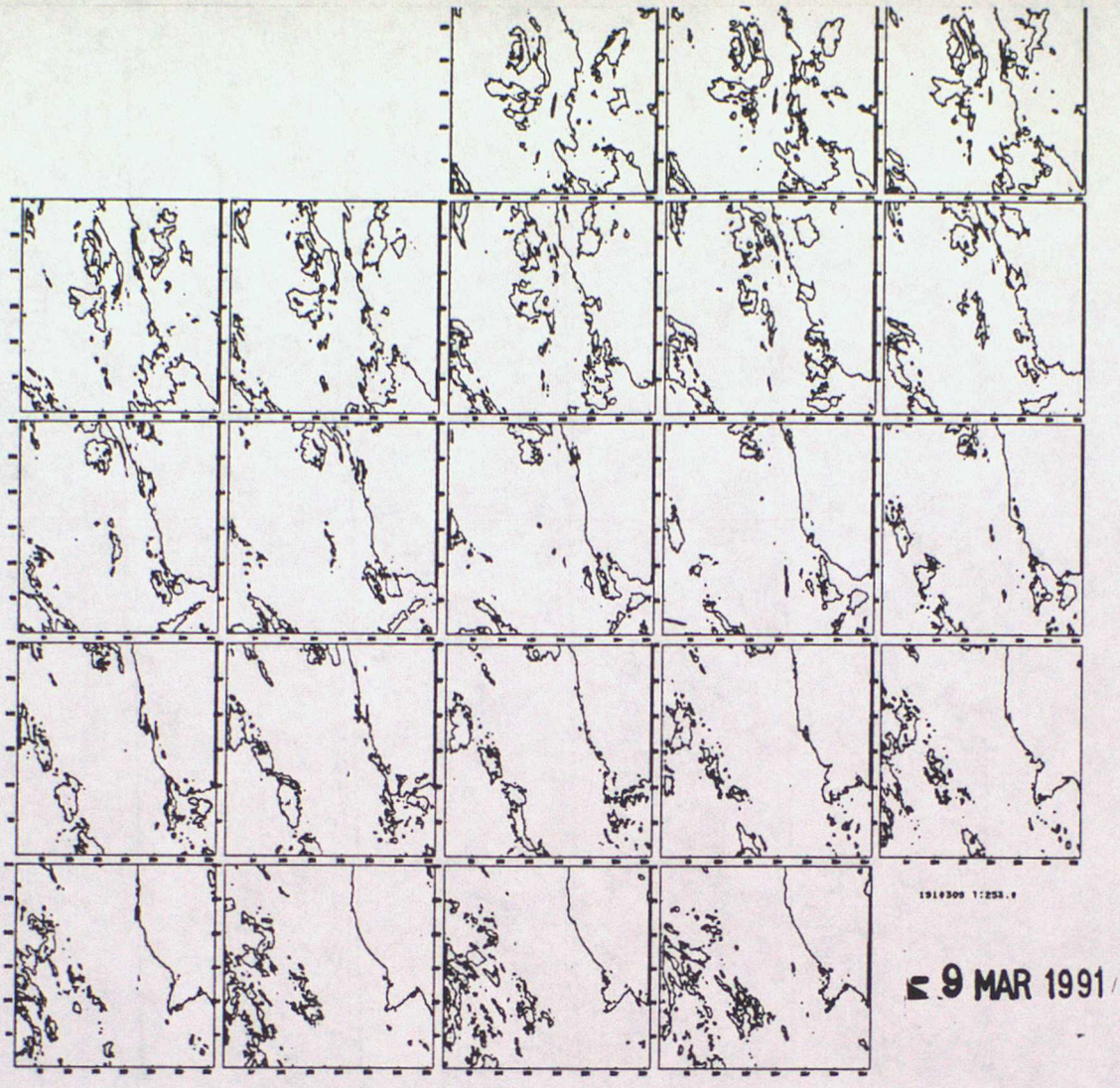


**Fig 11 Continued**

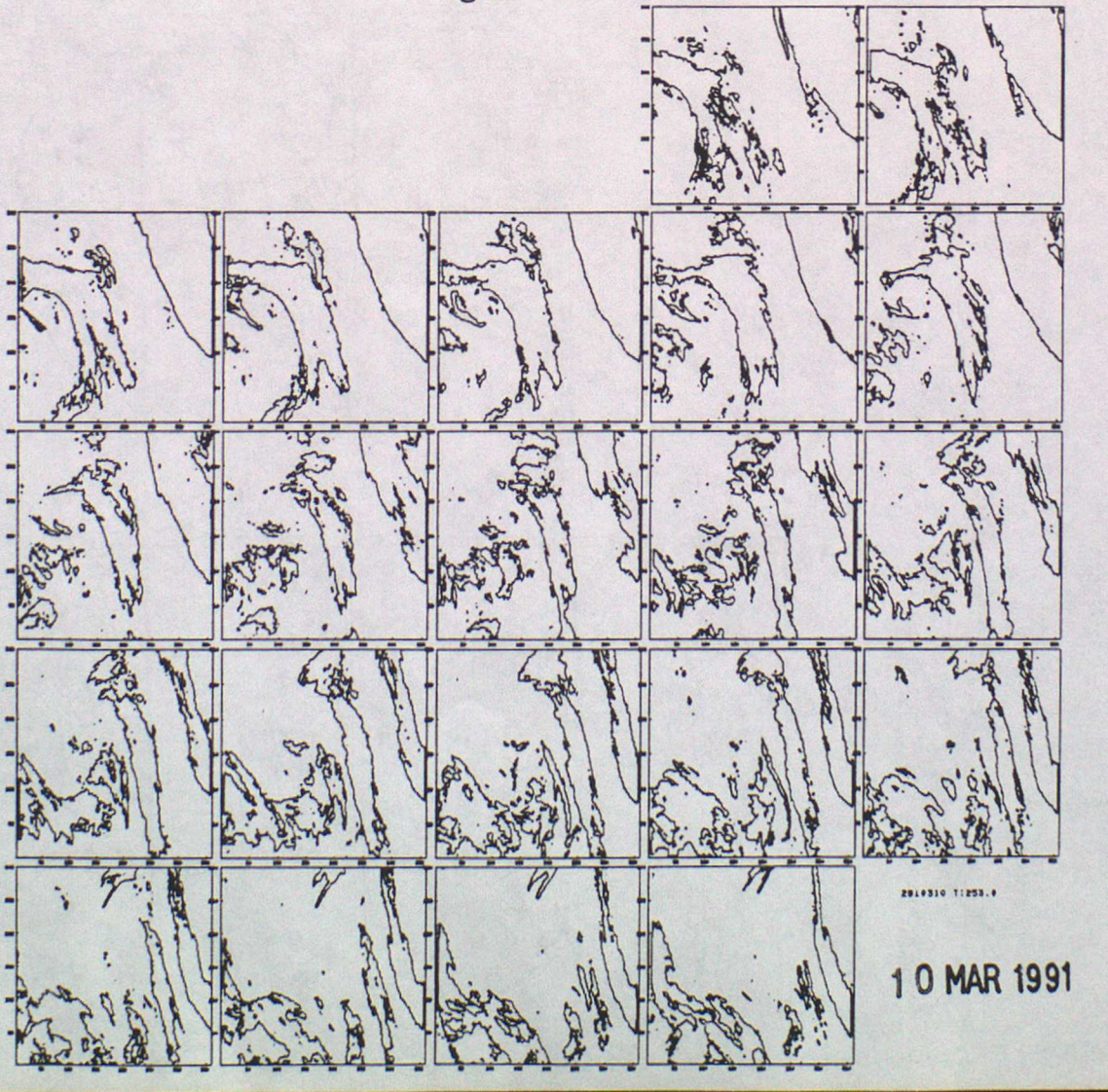

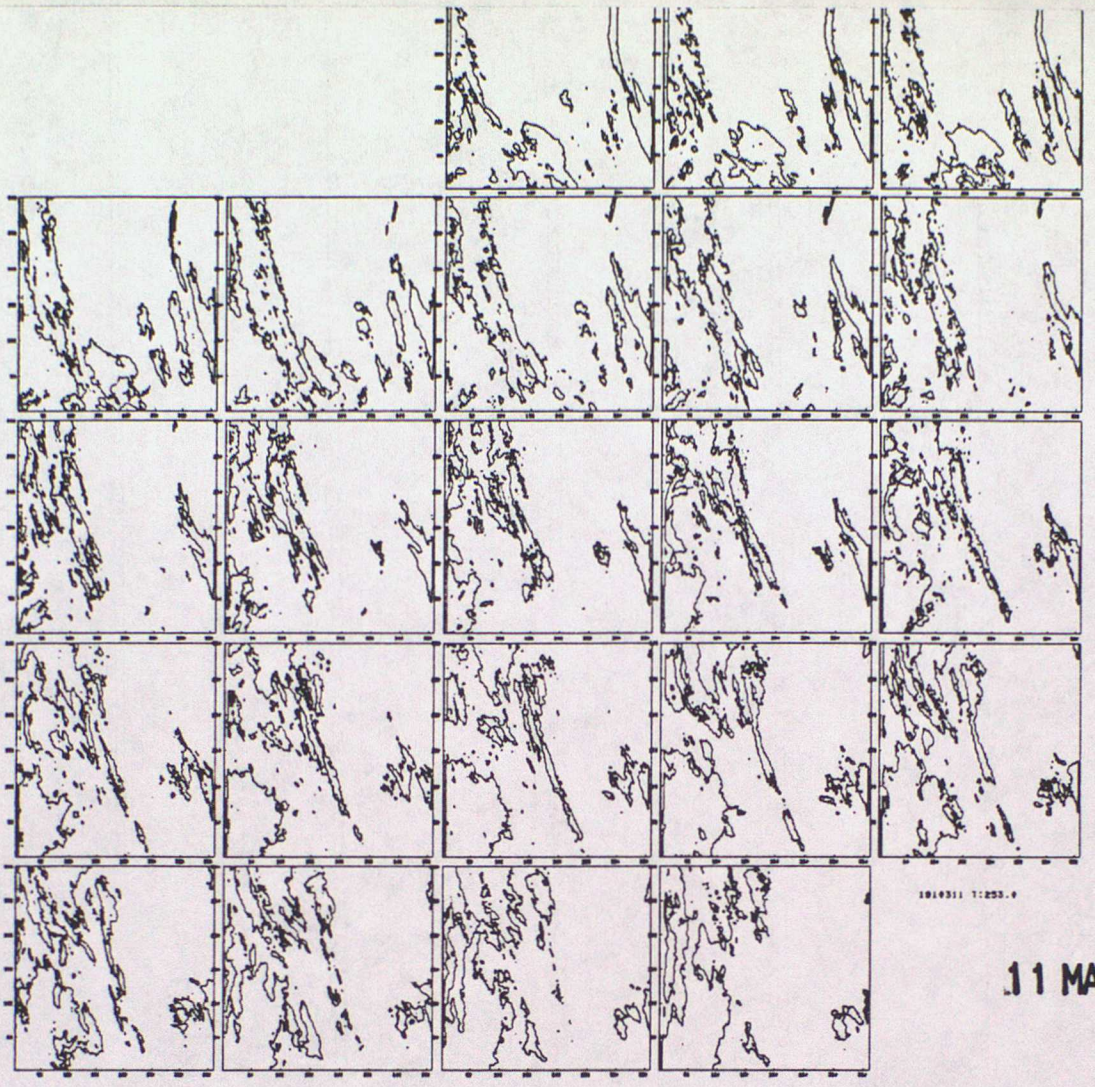


**Fig 11 Continued**

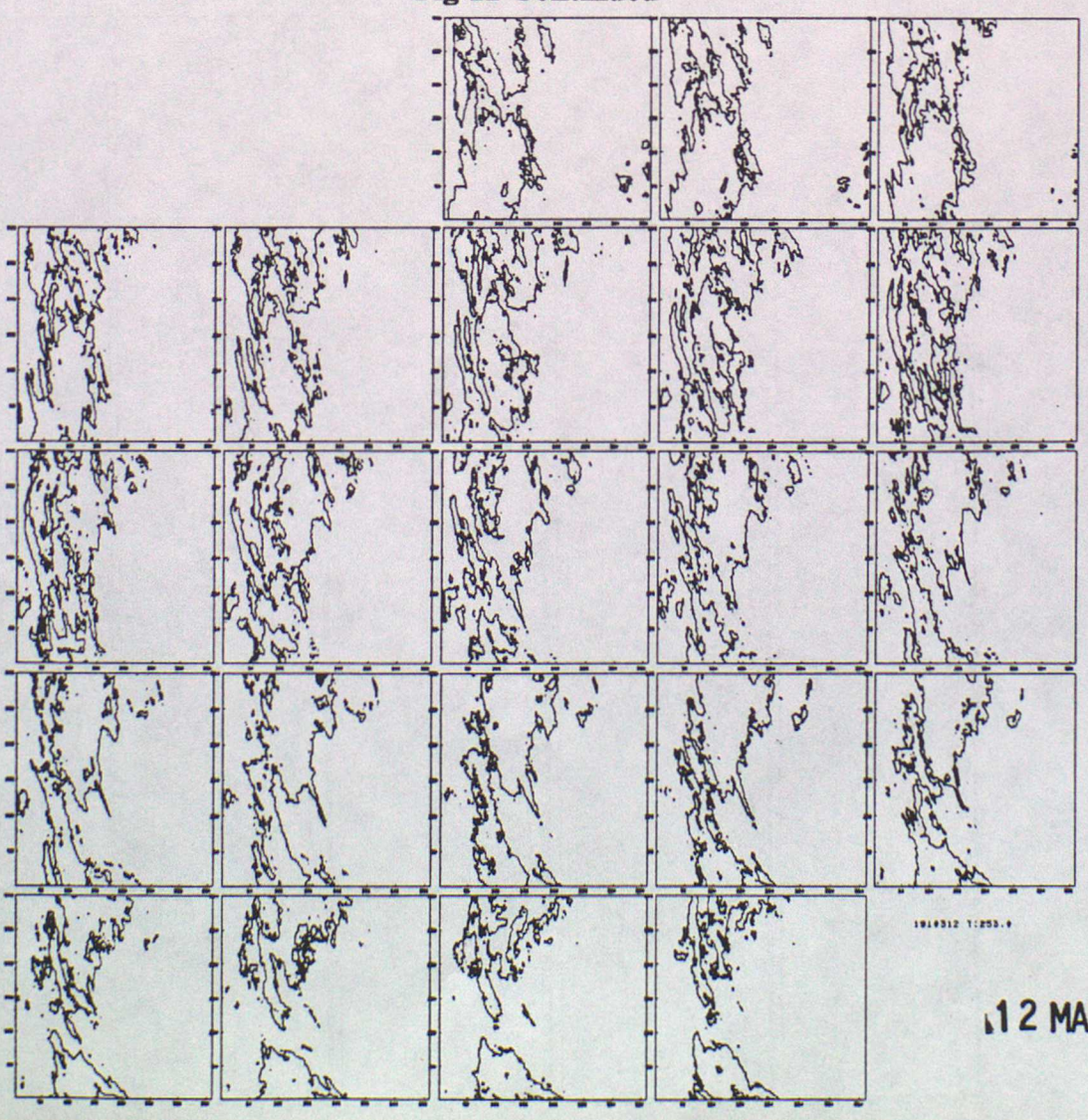

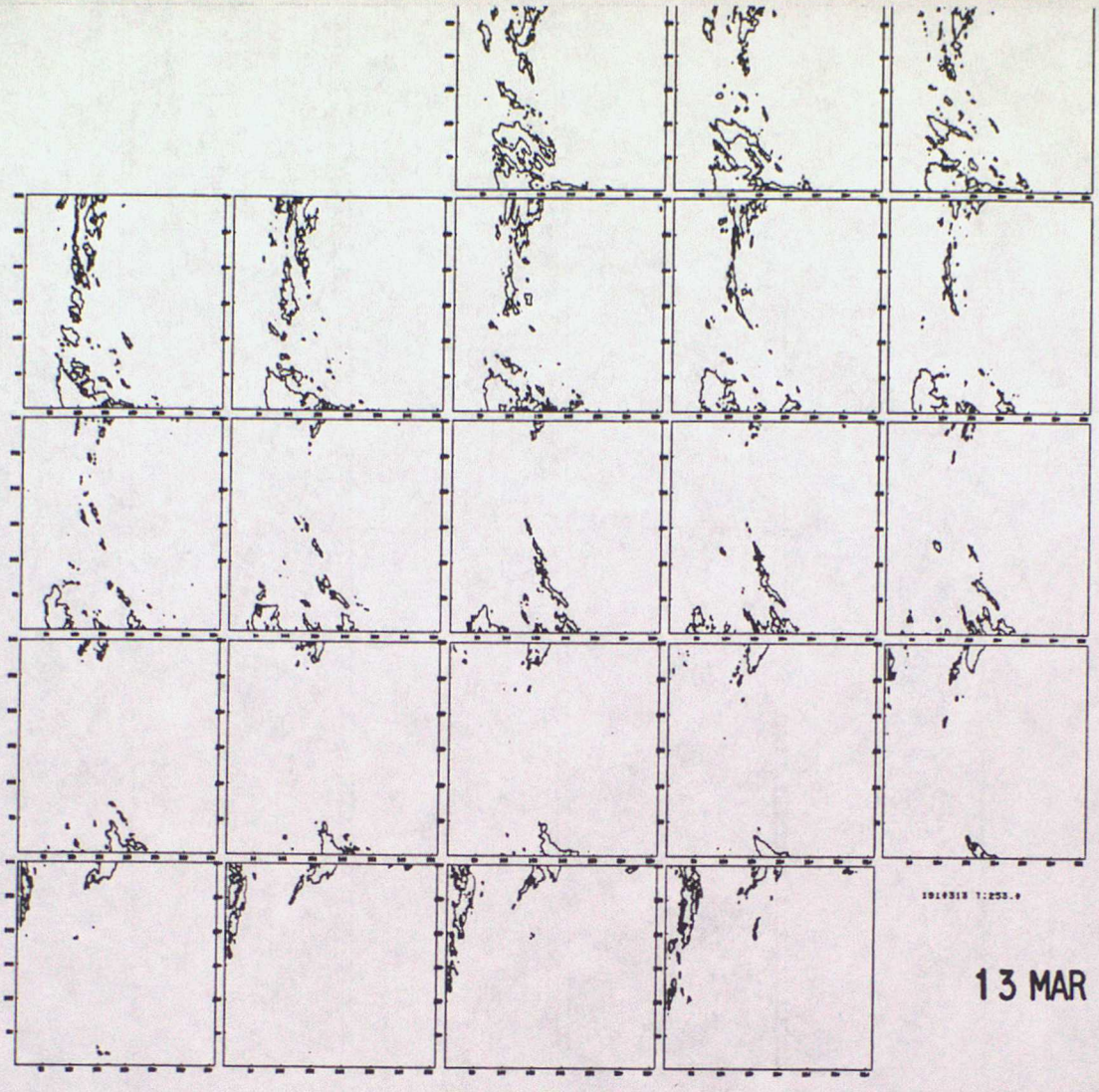

13 MAR 1991

**Fig 11 Continued**

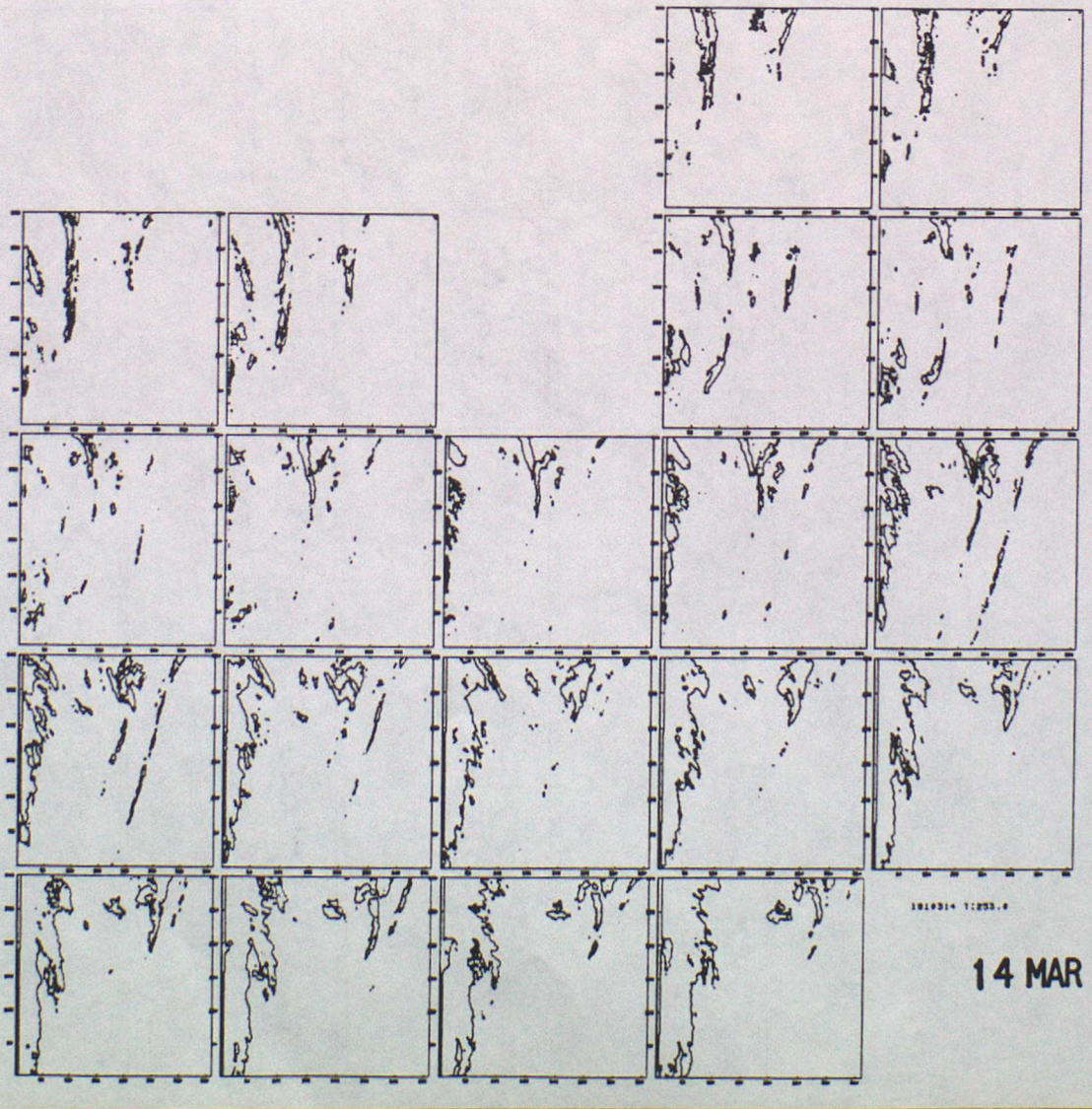

14 MAR 1991

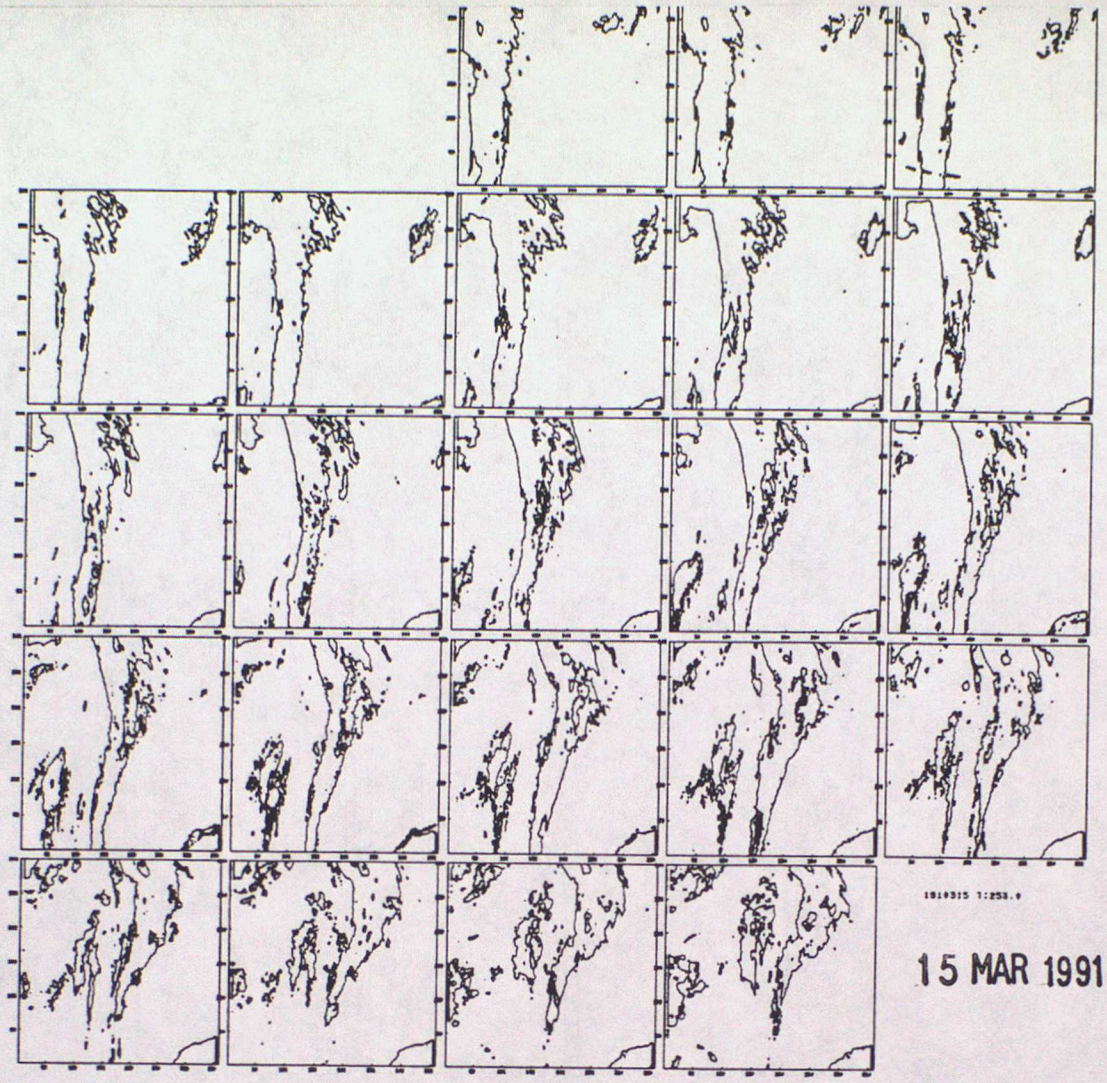


**Fig 11 Continued**

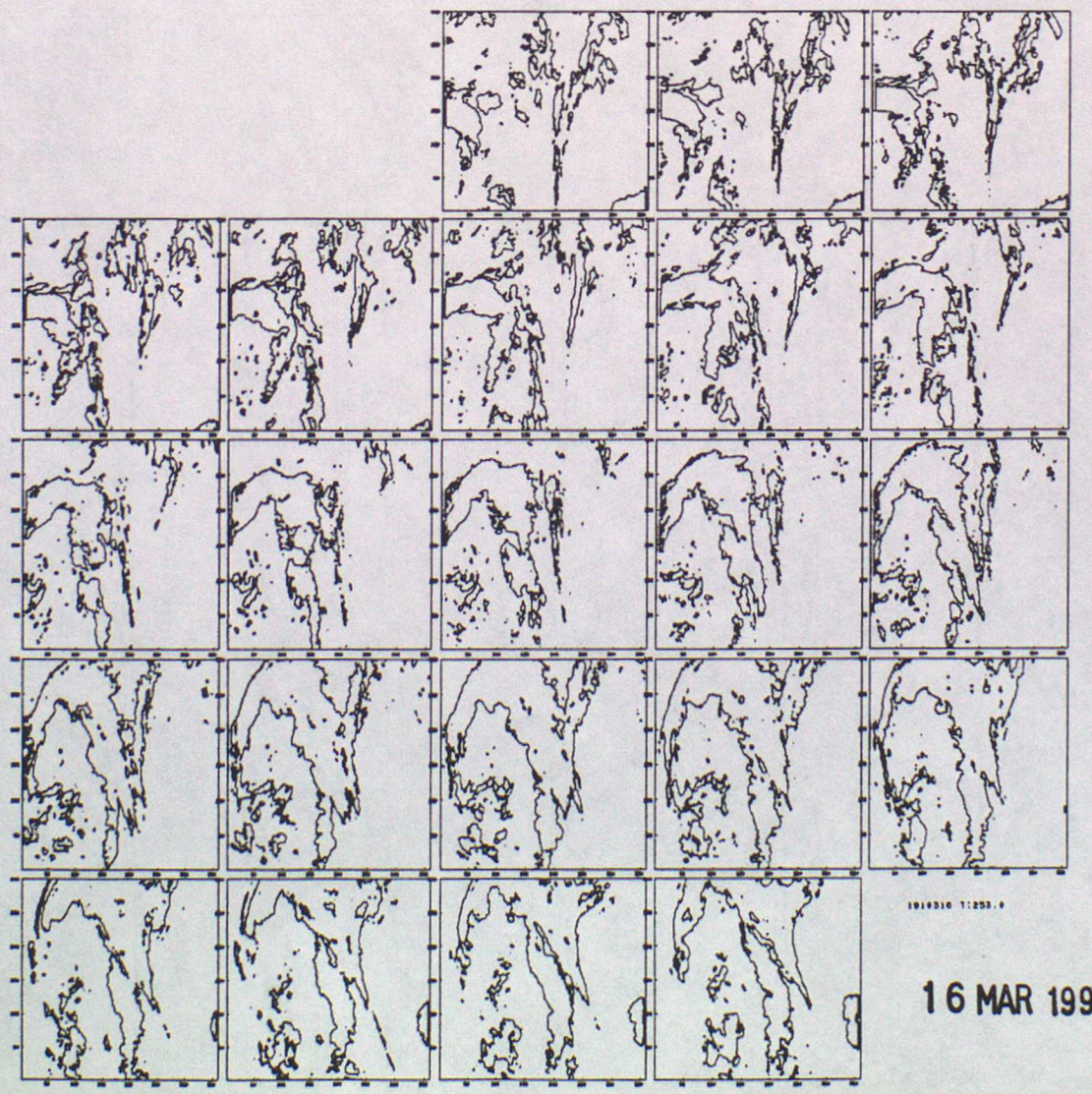

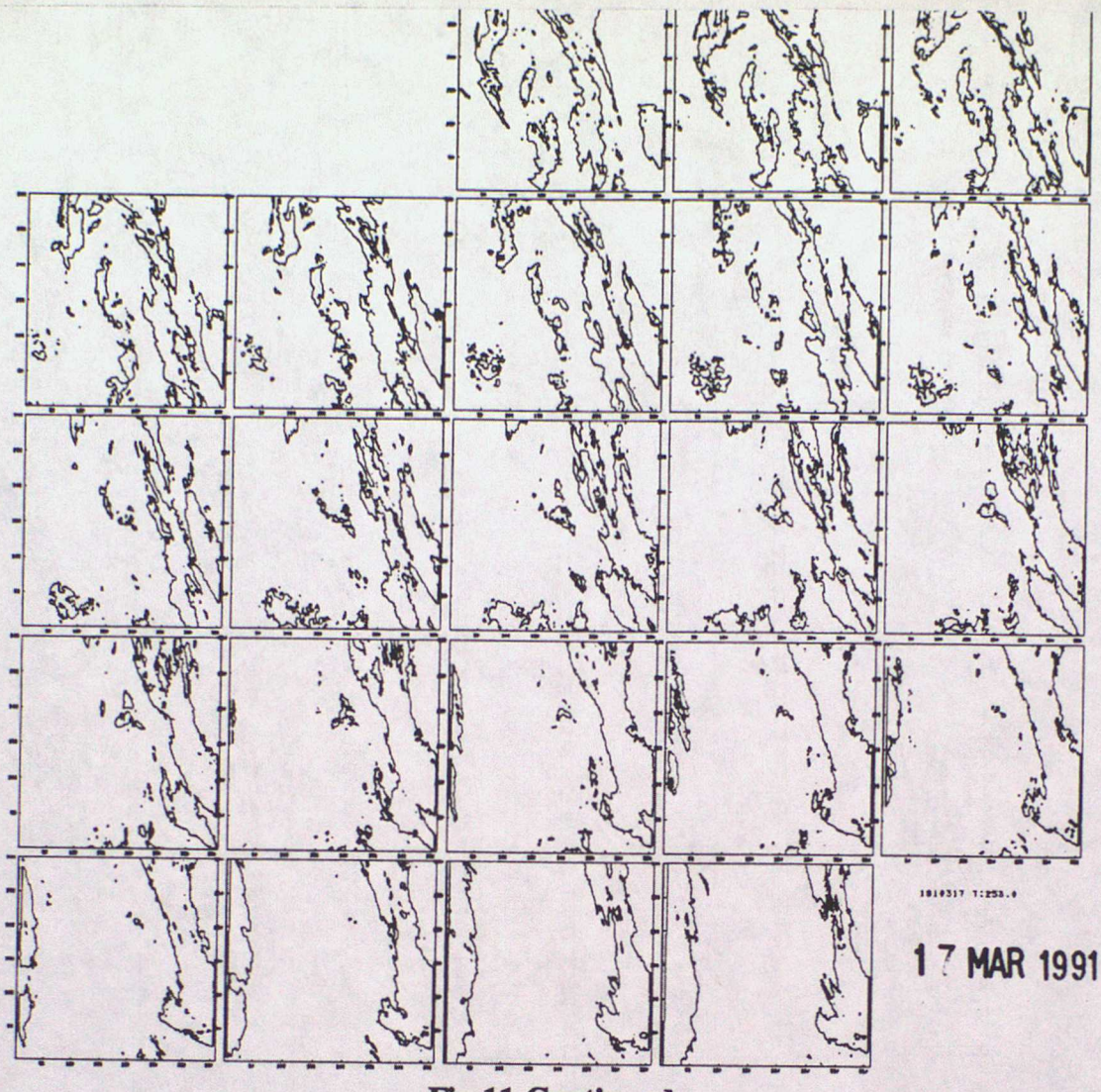


**Fig 11 Continued**

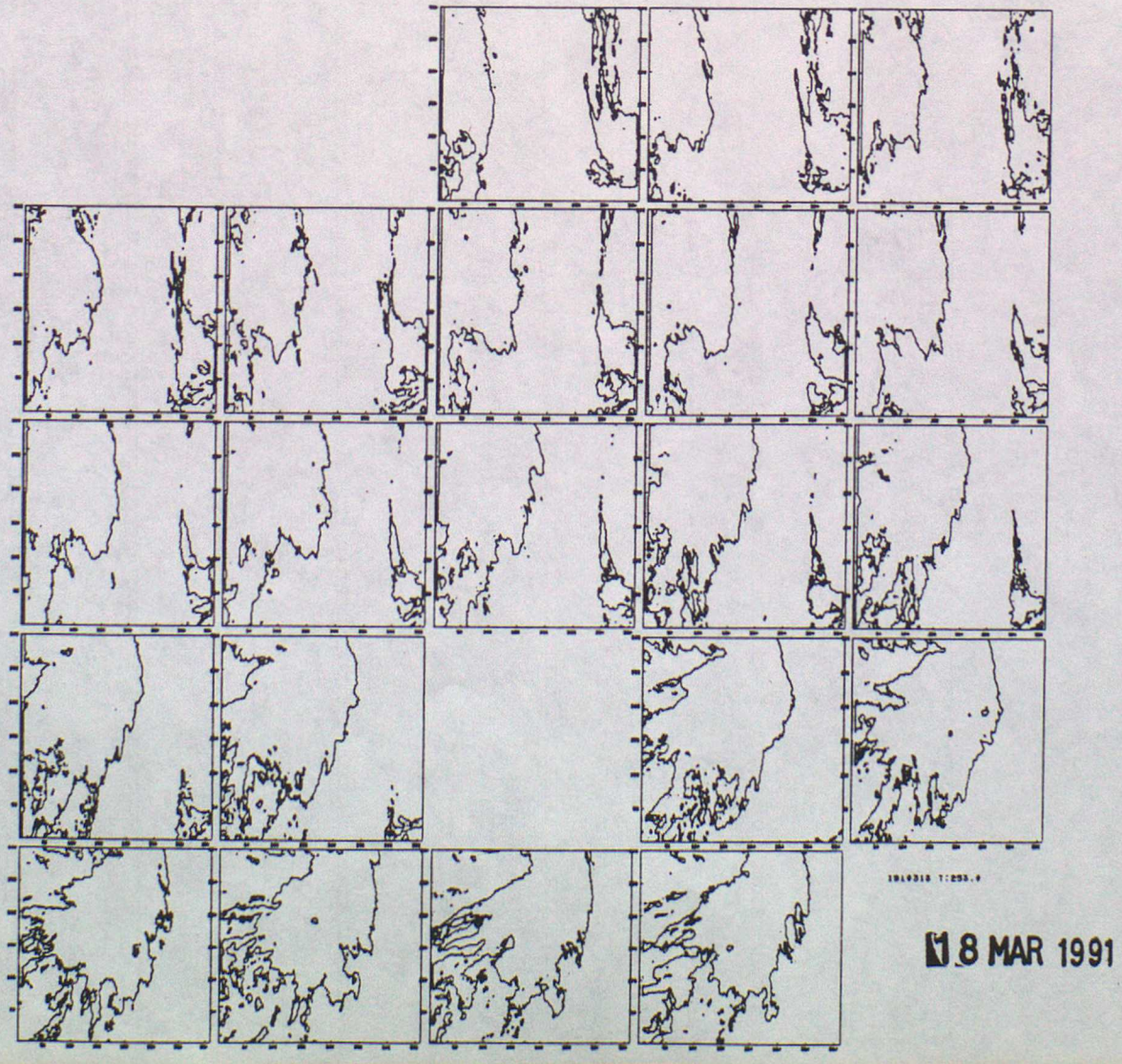

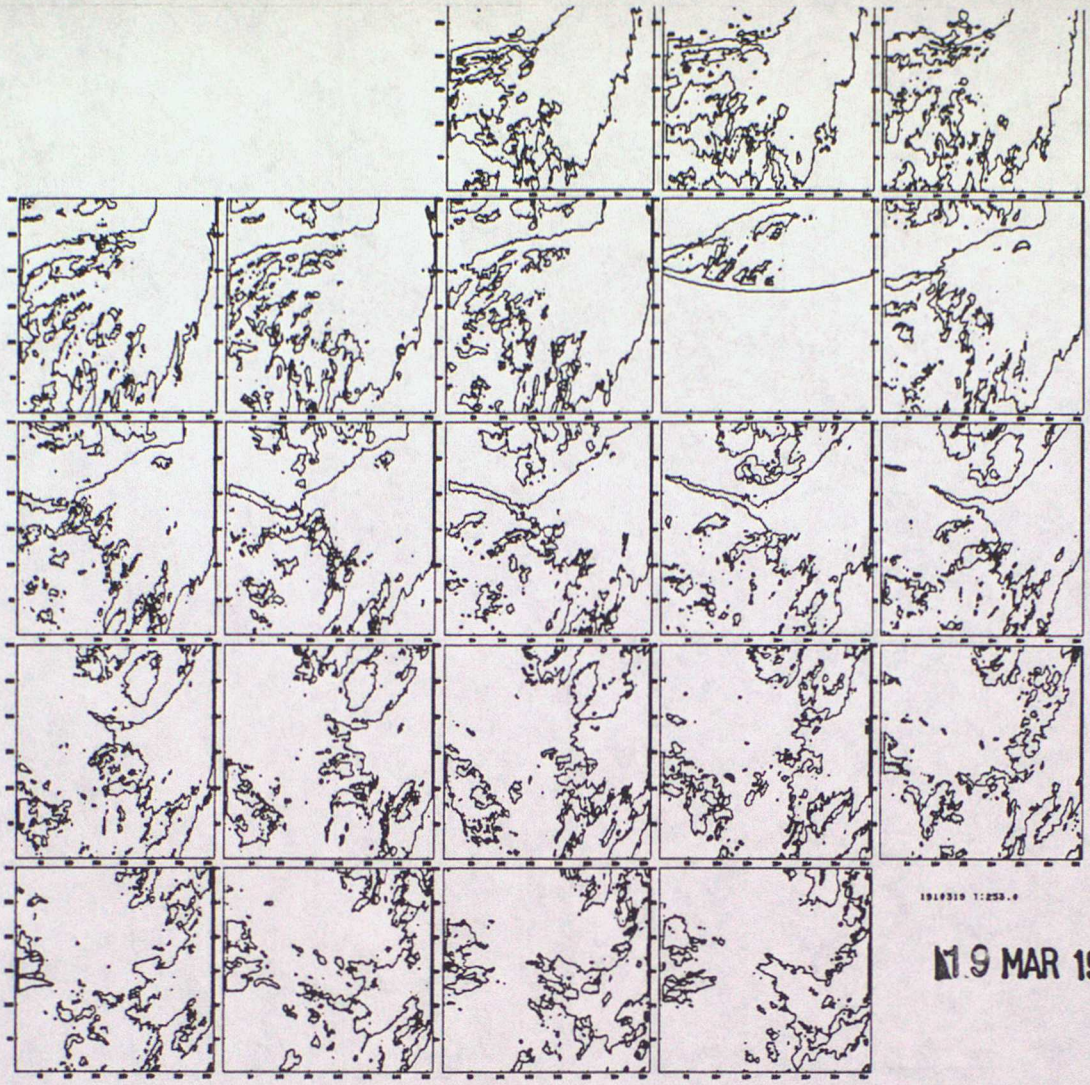


**Fig 11 Continued**

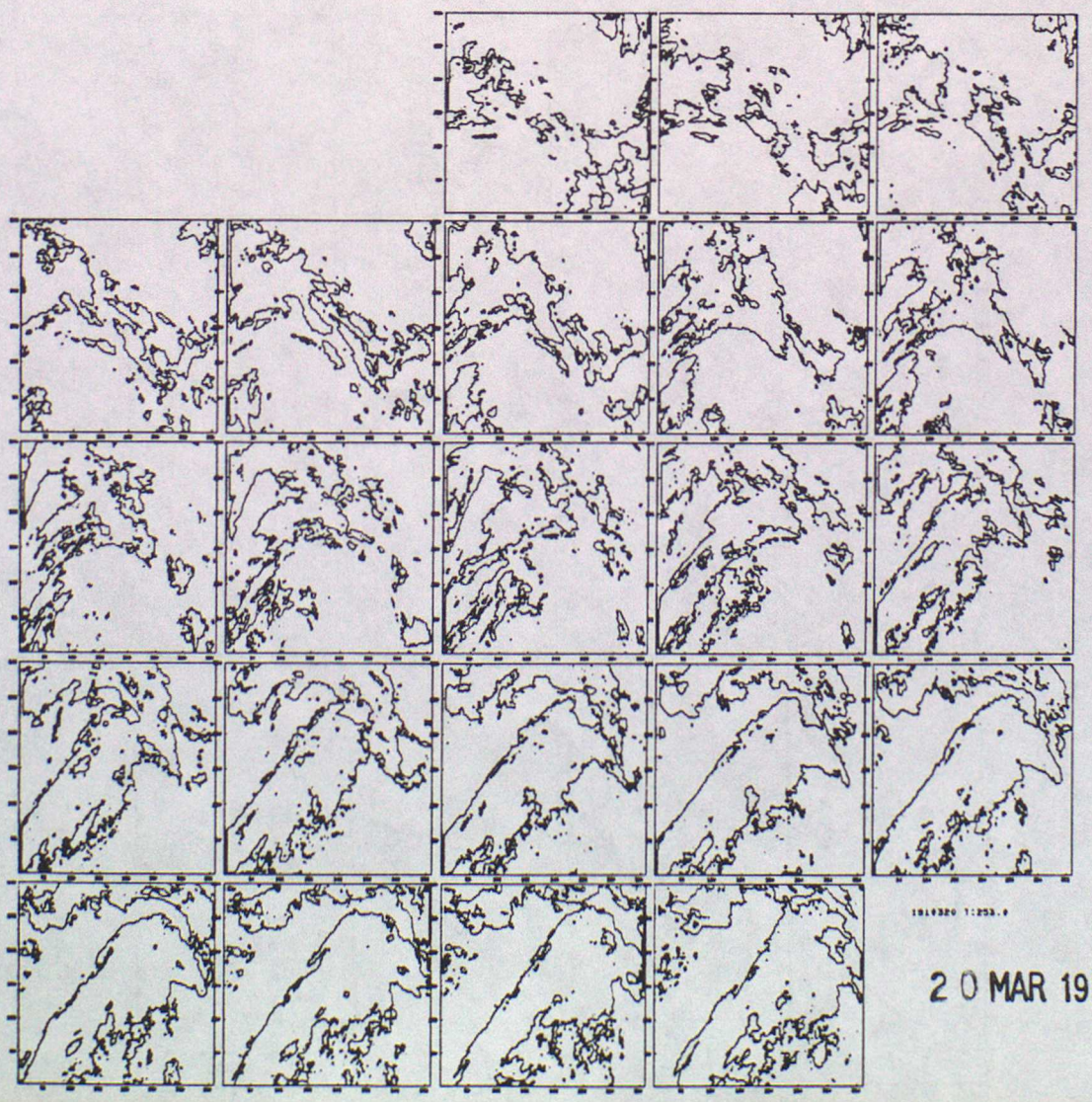

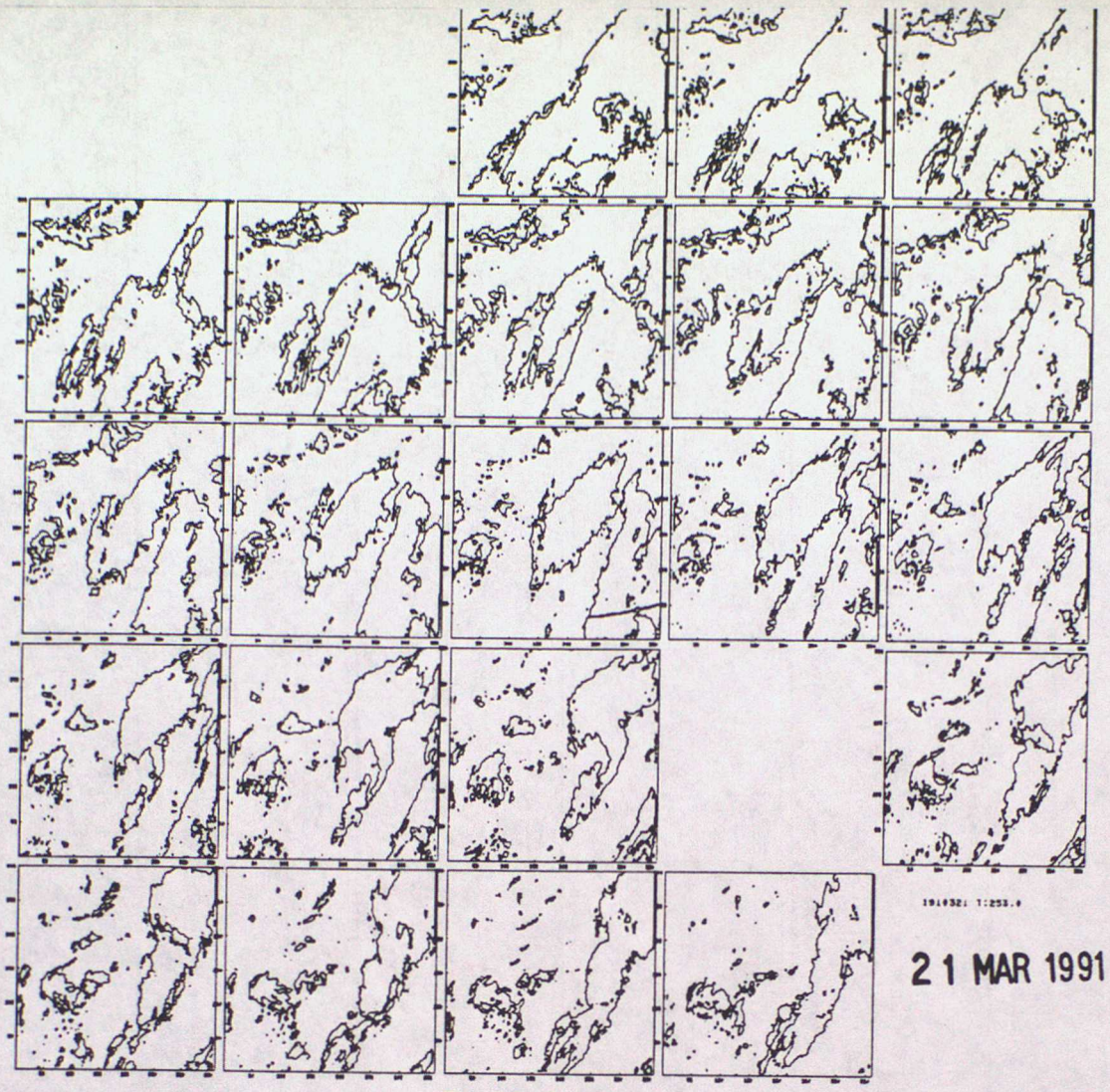


**Fig 11 Continued**

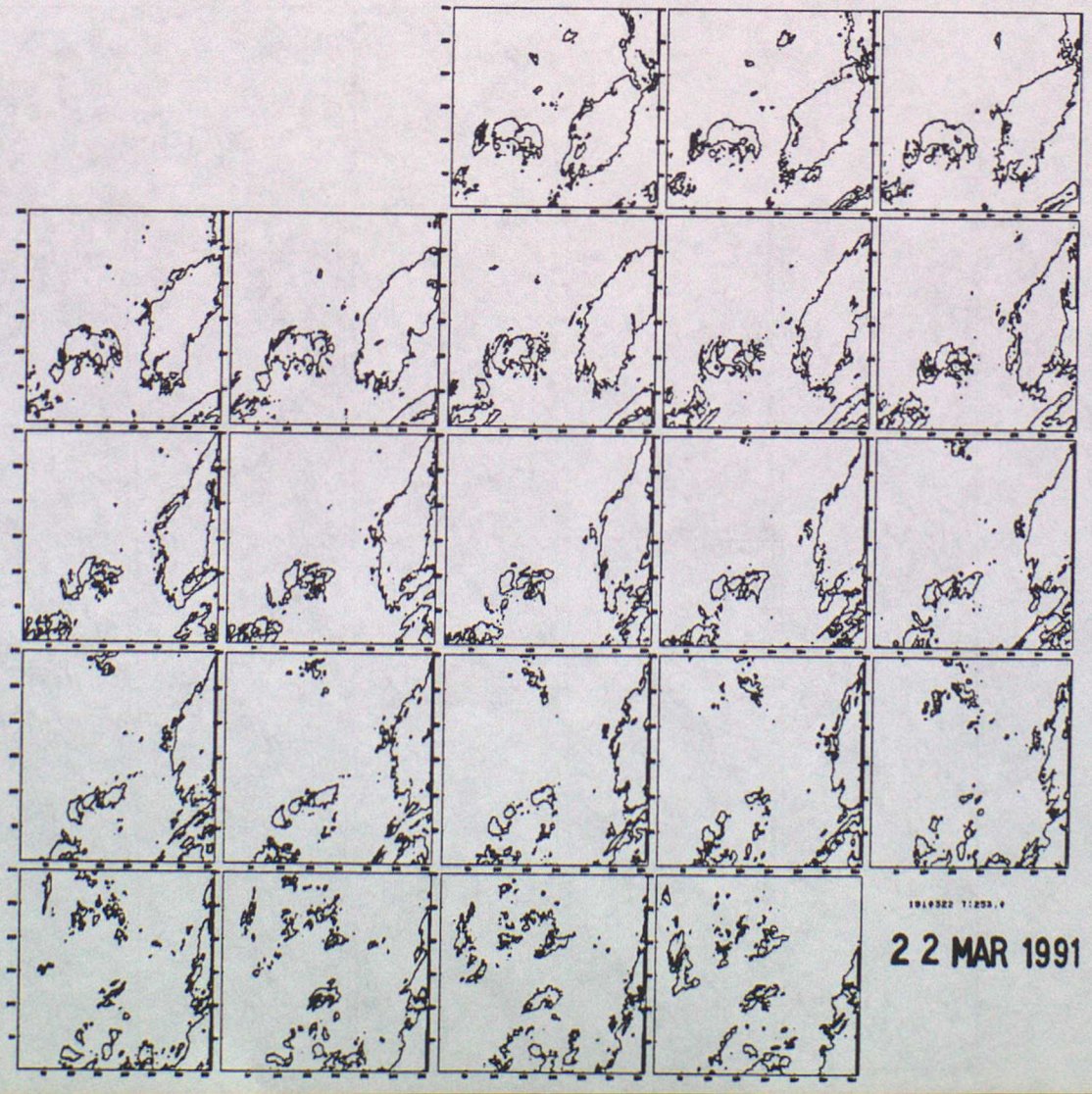

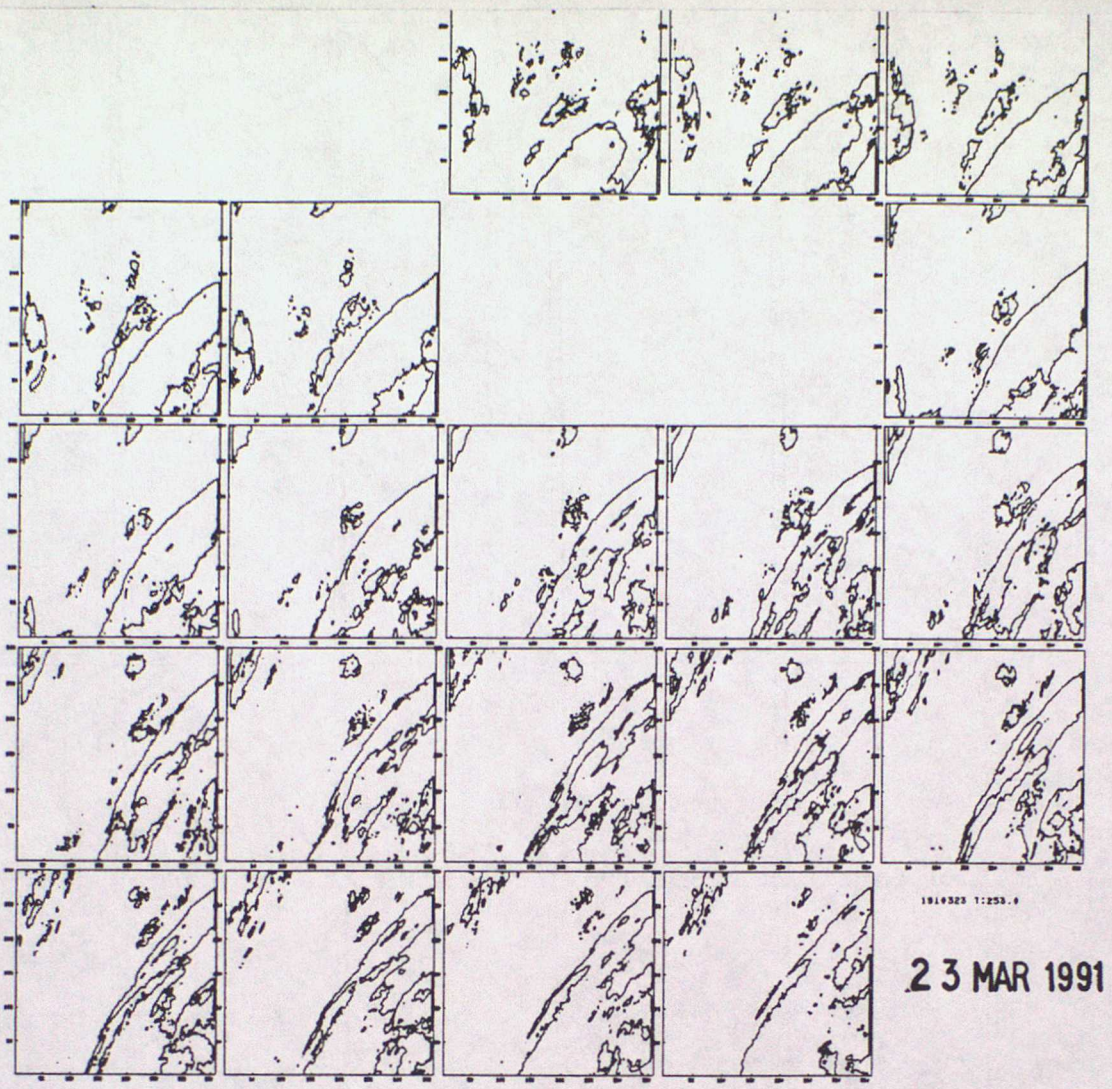


**Fig 11 Continued**

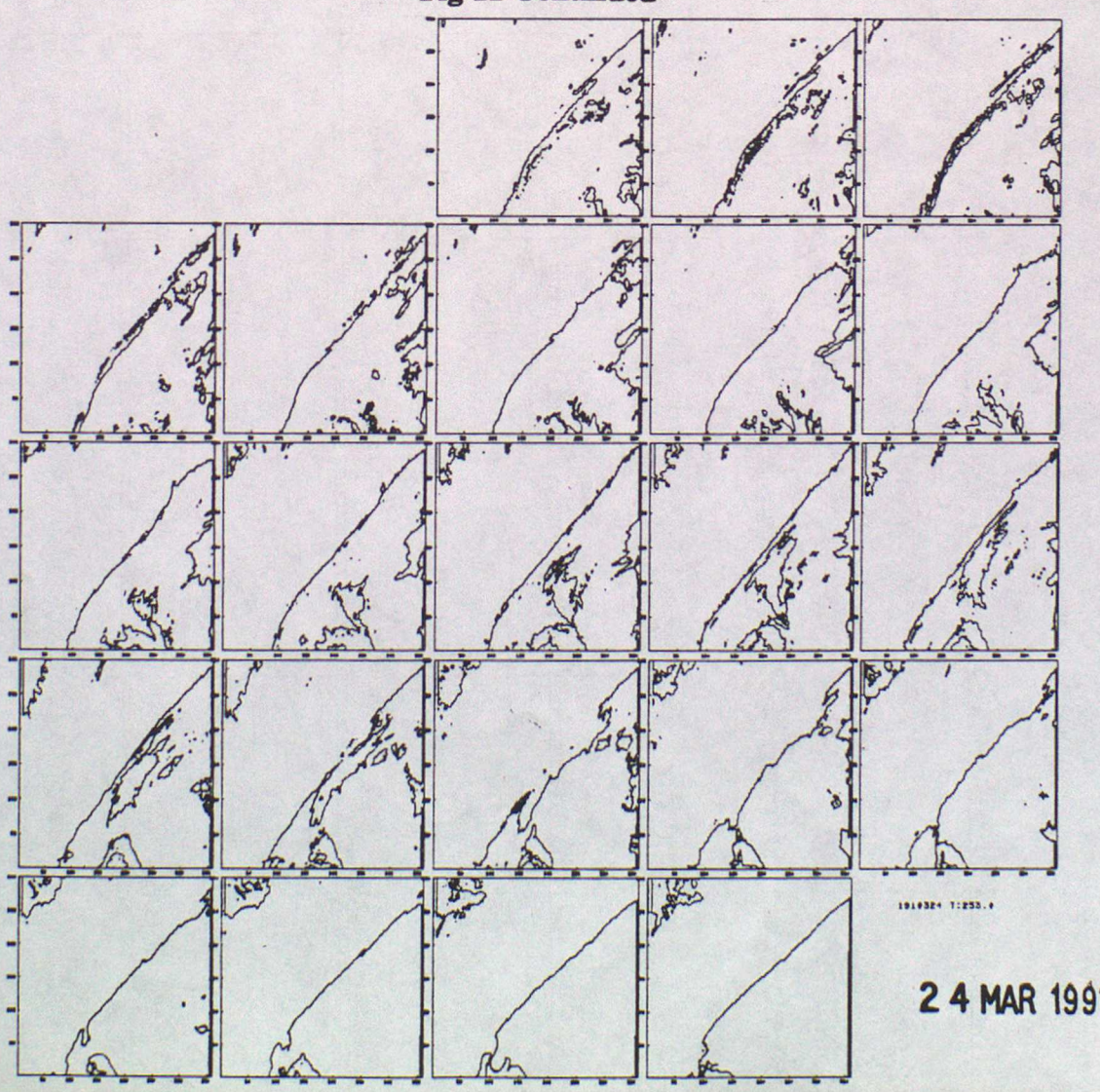

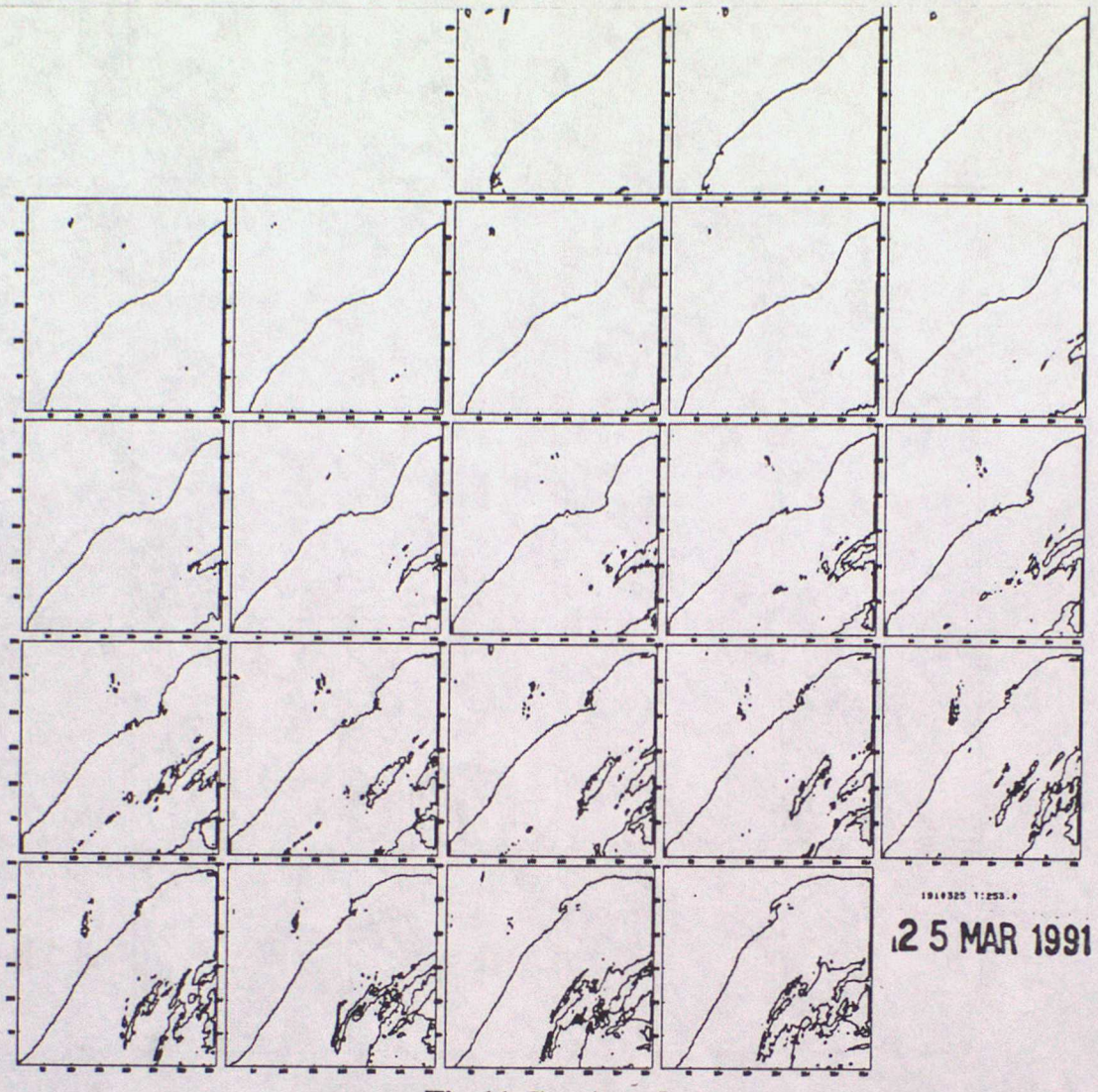


**Fig 11 Continued**

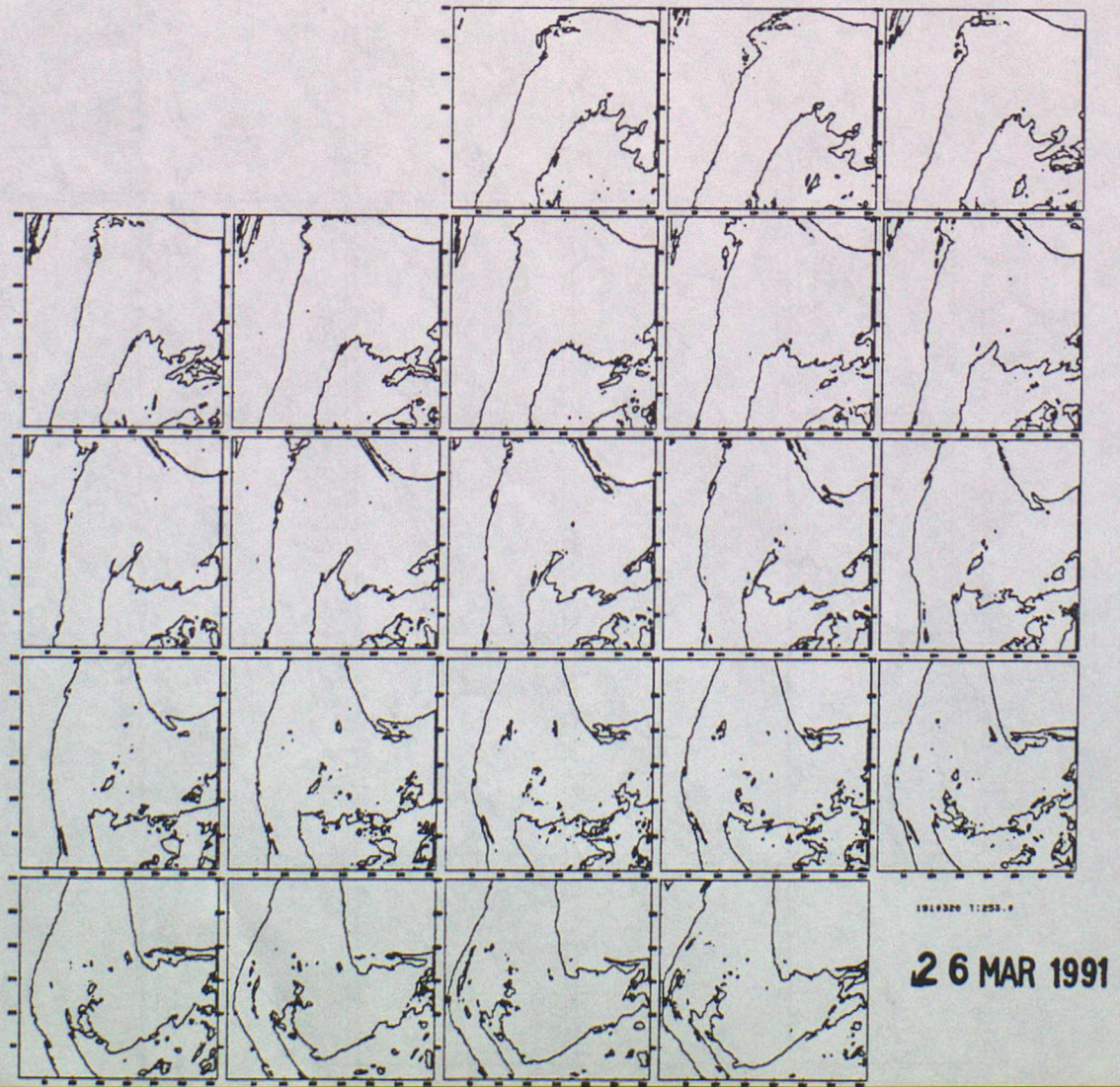

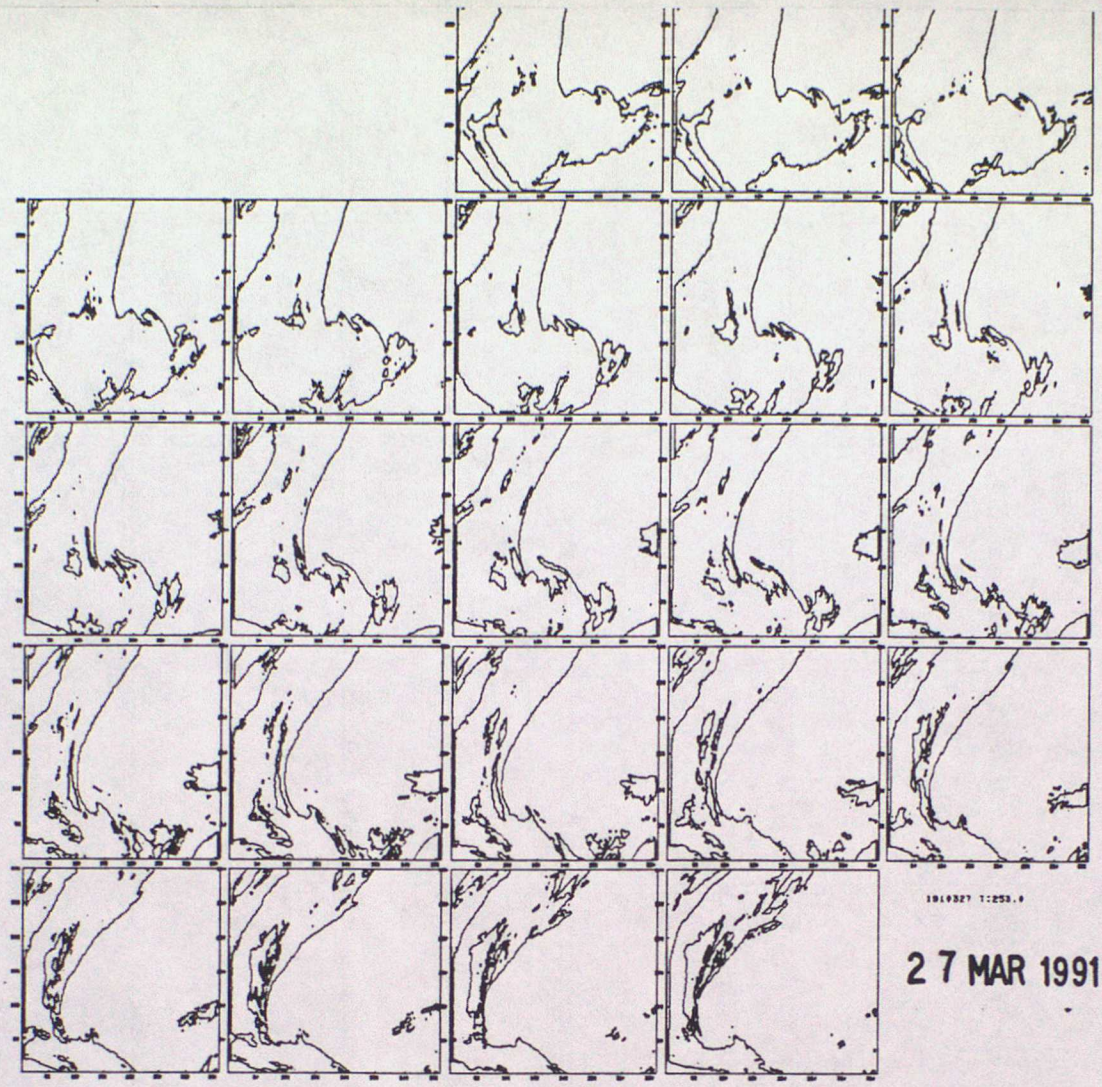


**Fig 11 Continued**

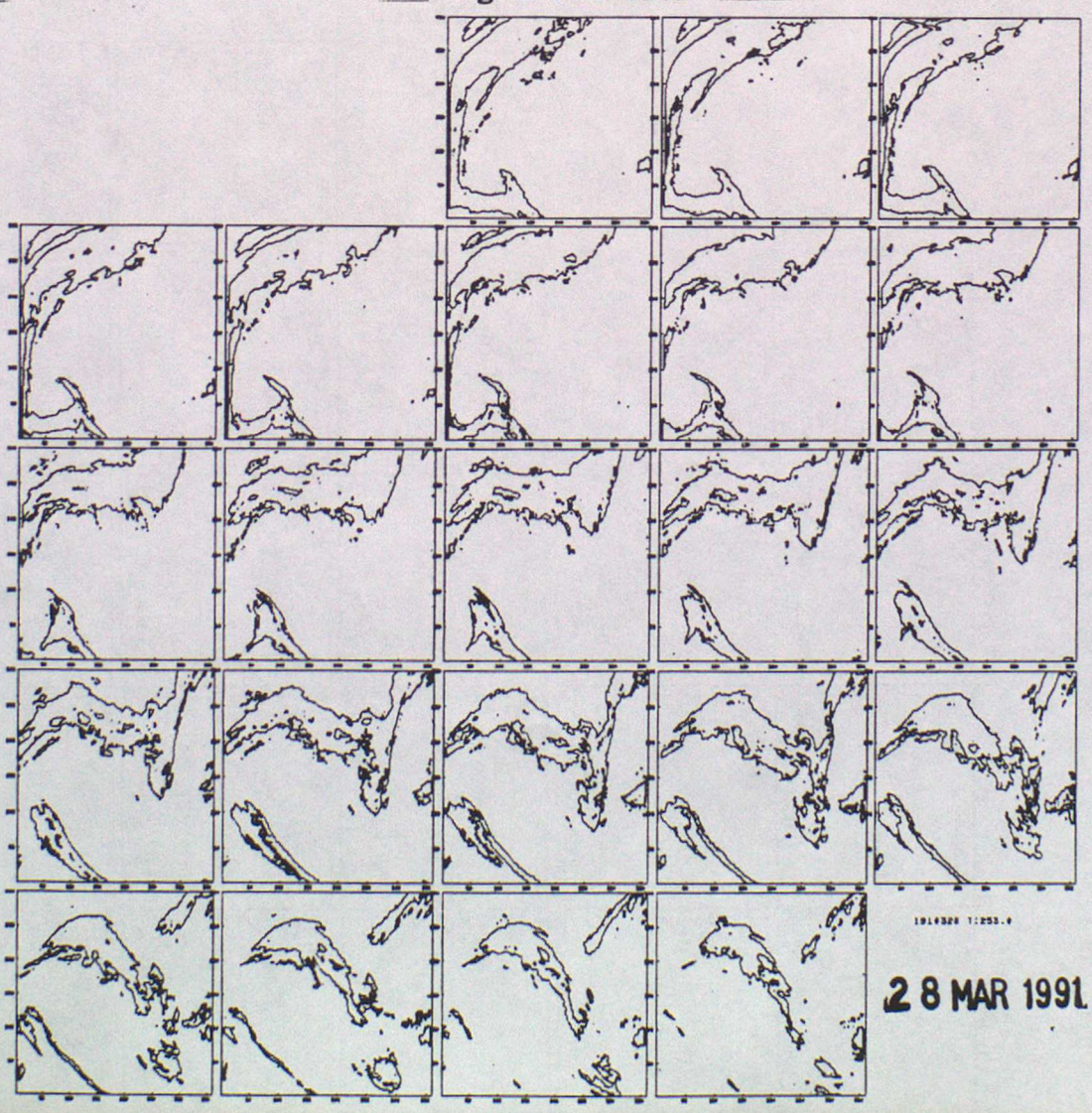

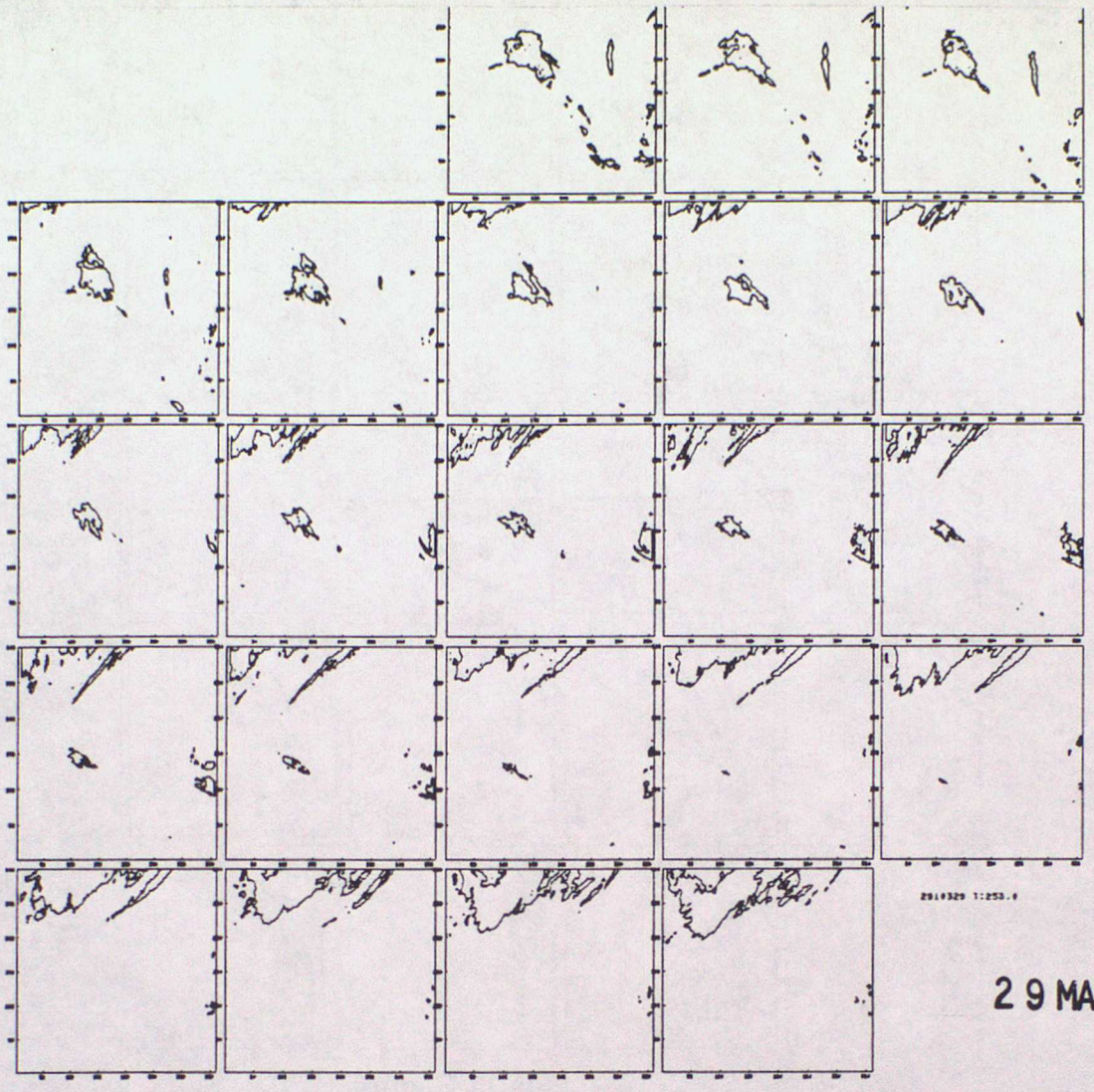


**Fig 11 Continued**

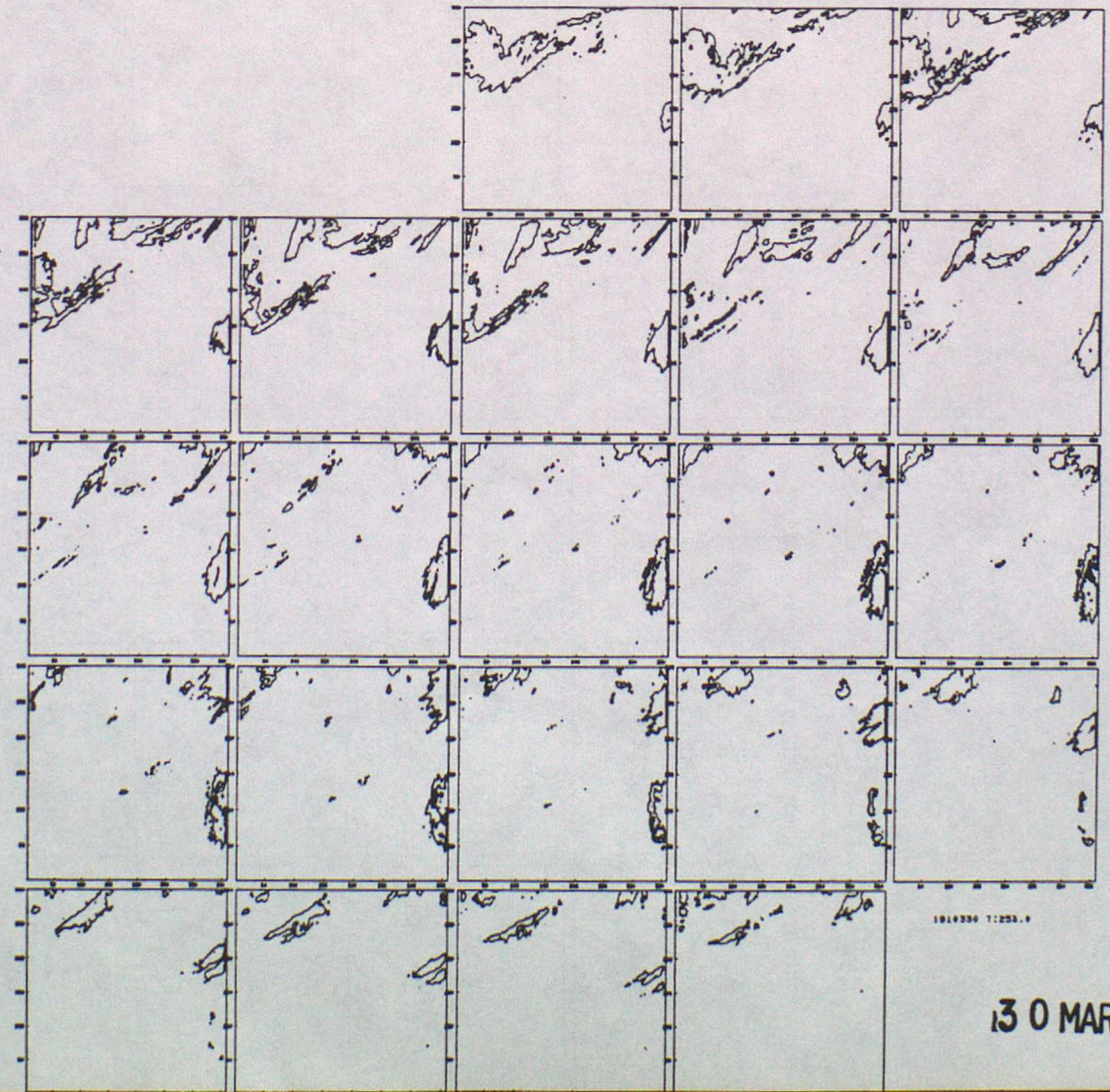

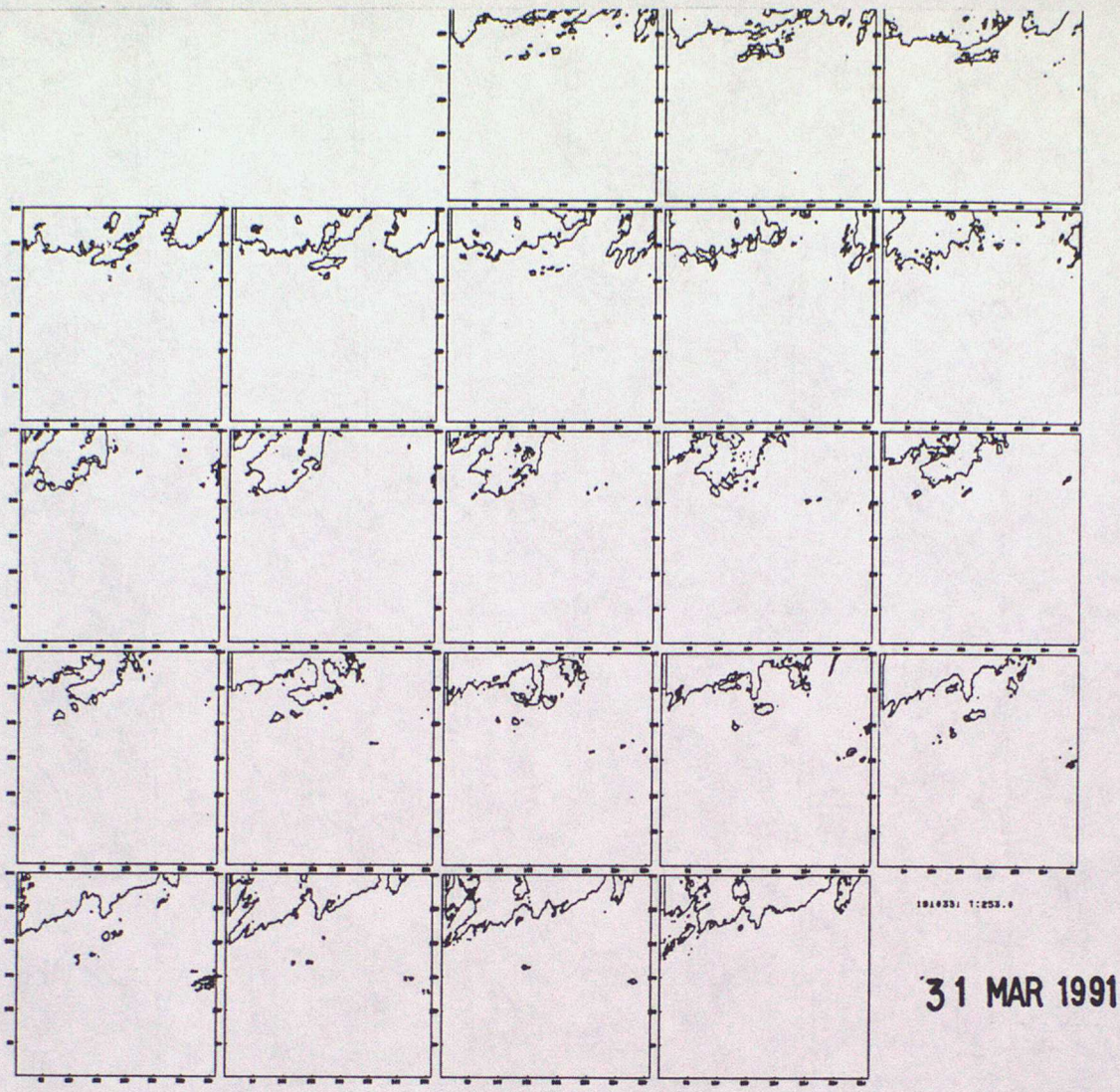


**Fig 11 Continued**

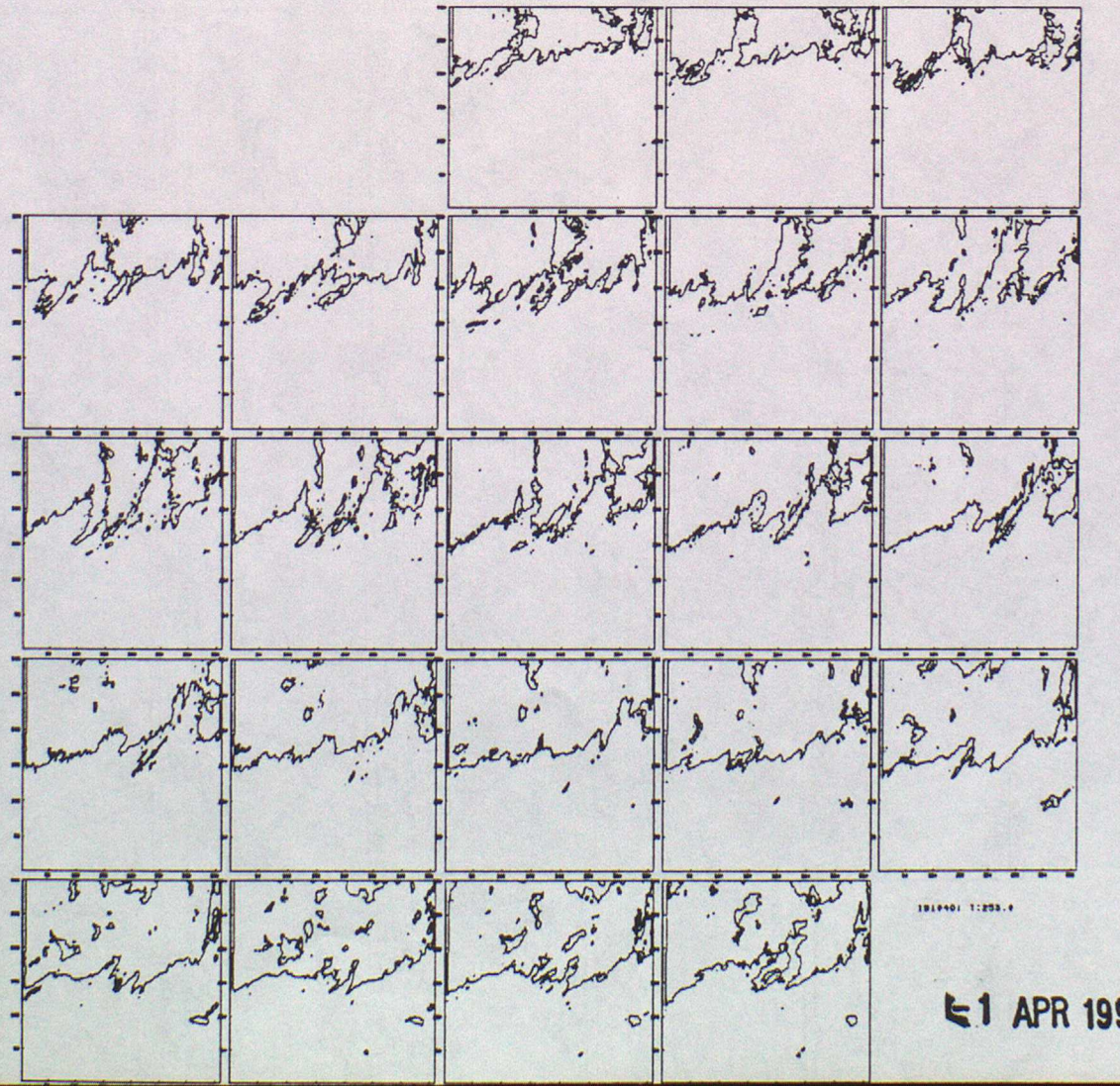

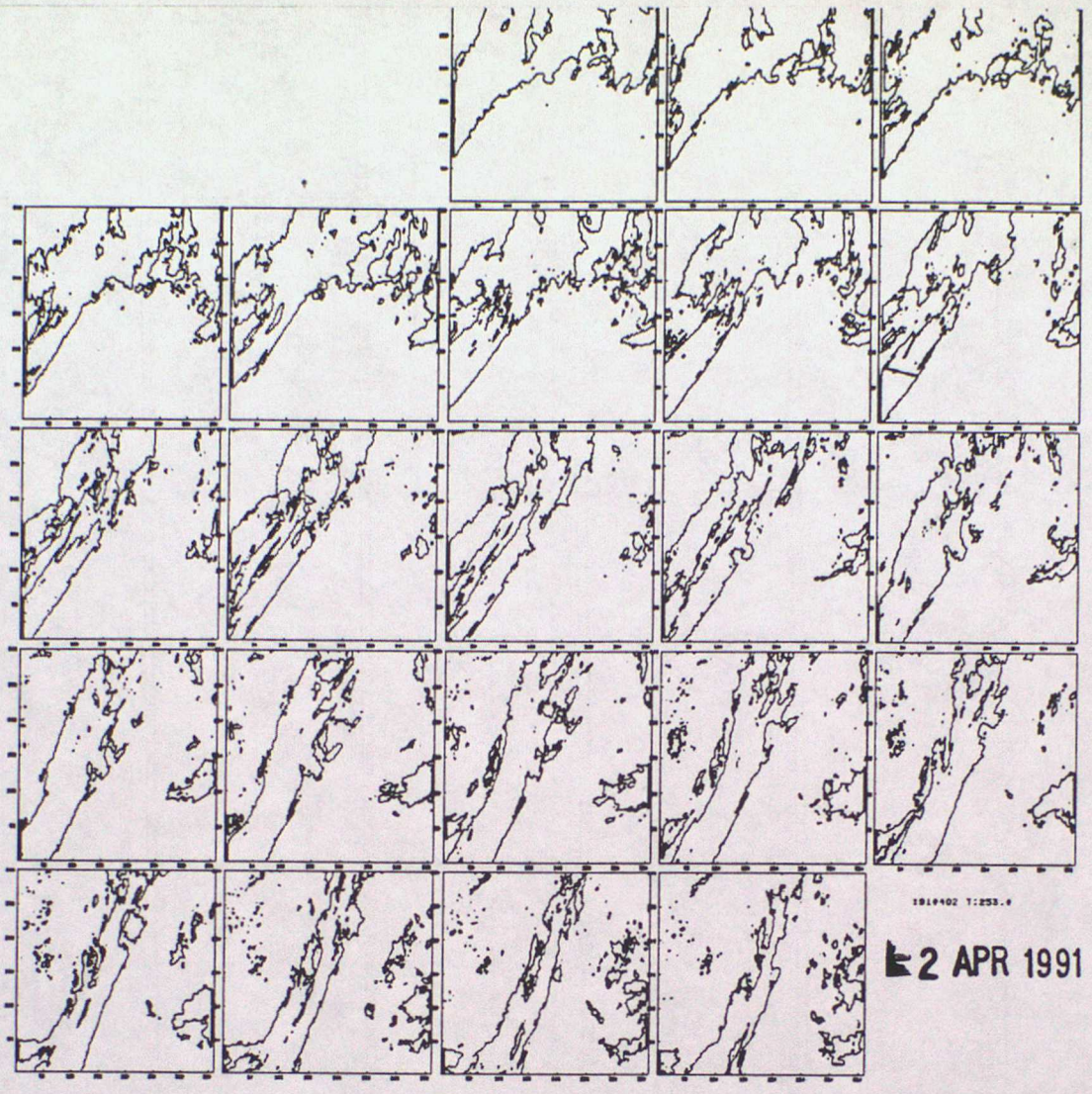


**Fig 11 Continued**

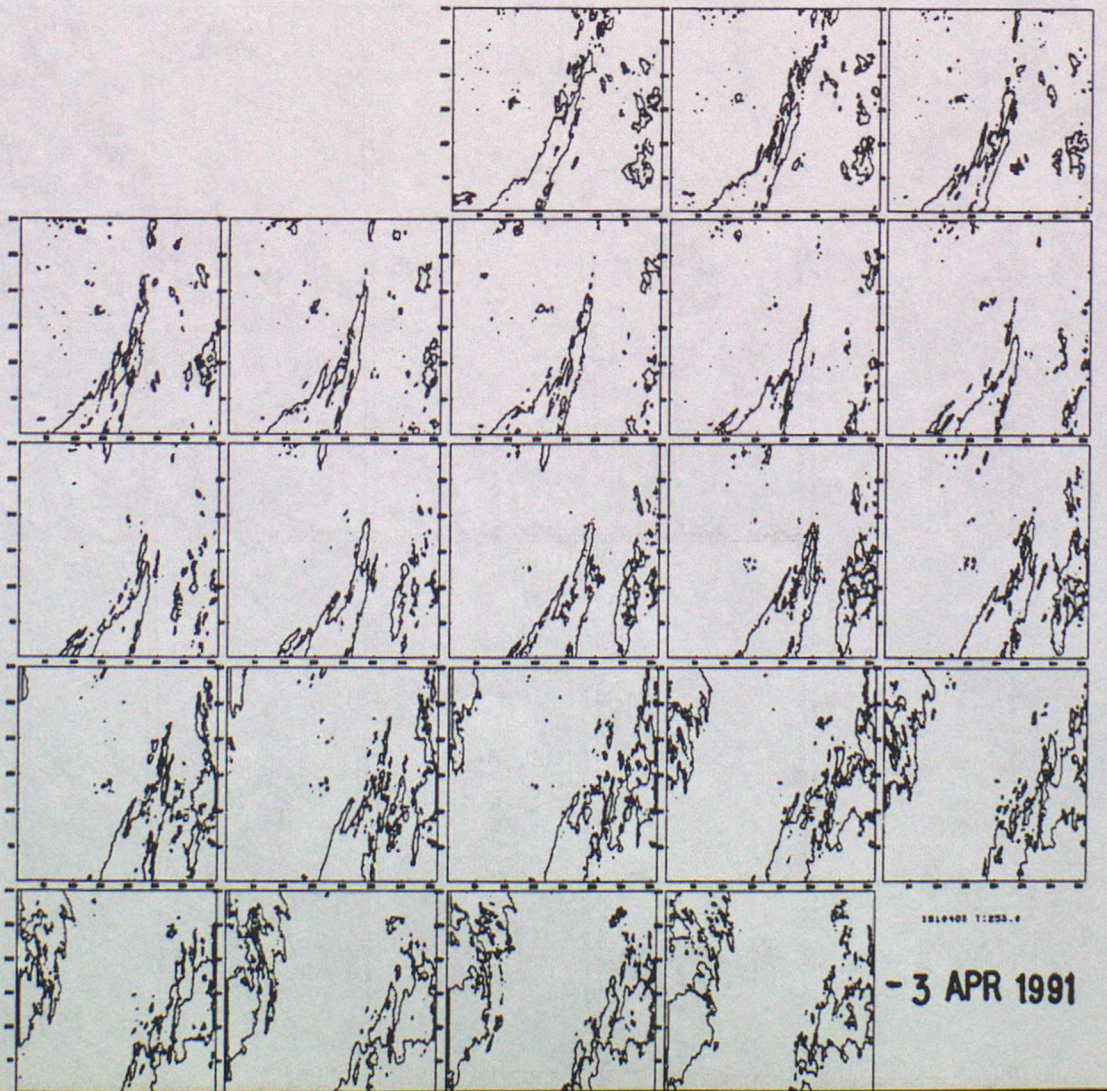

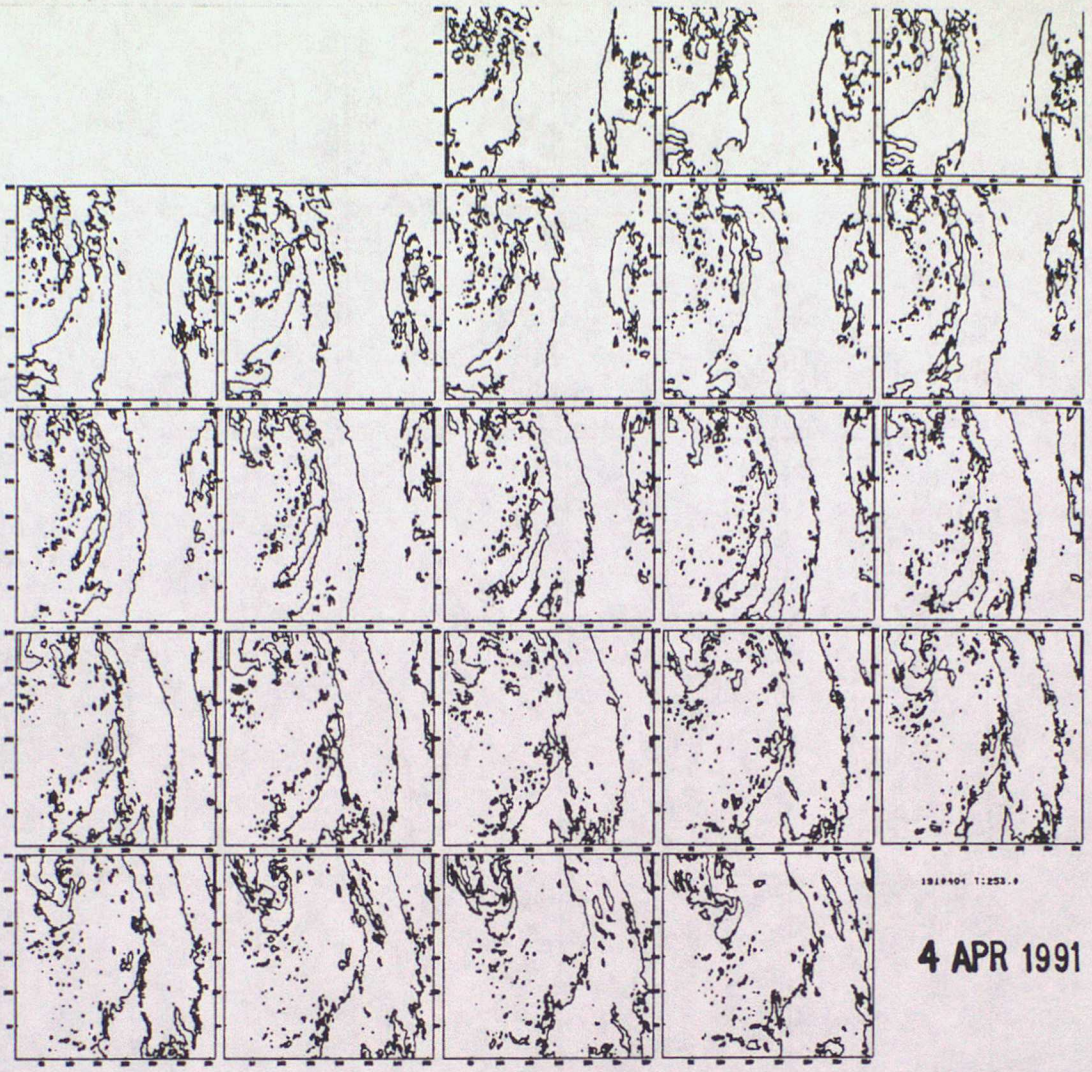


**Fig 11 Continued**

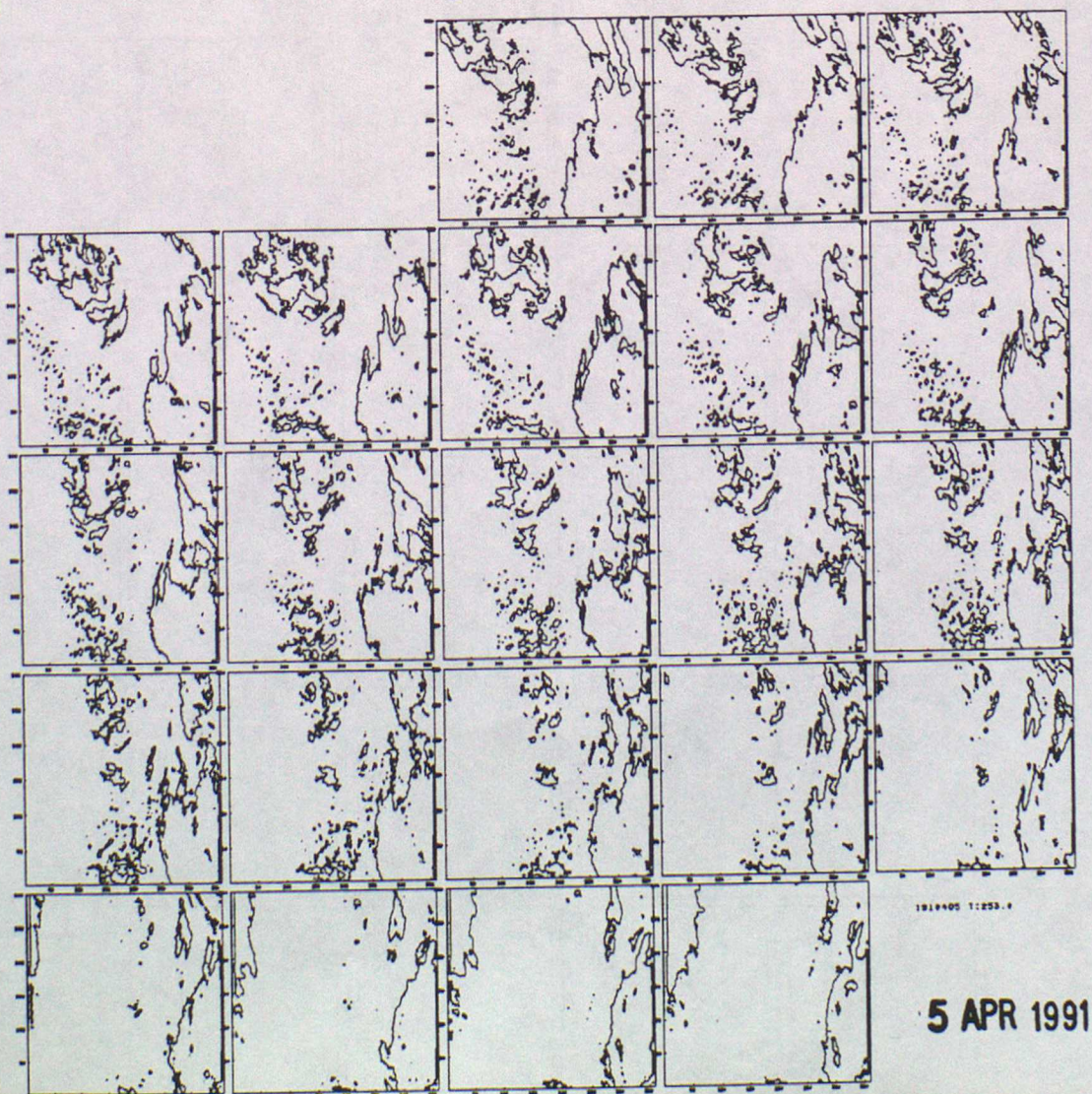

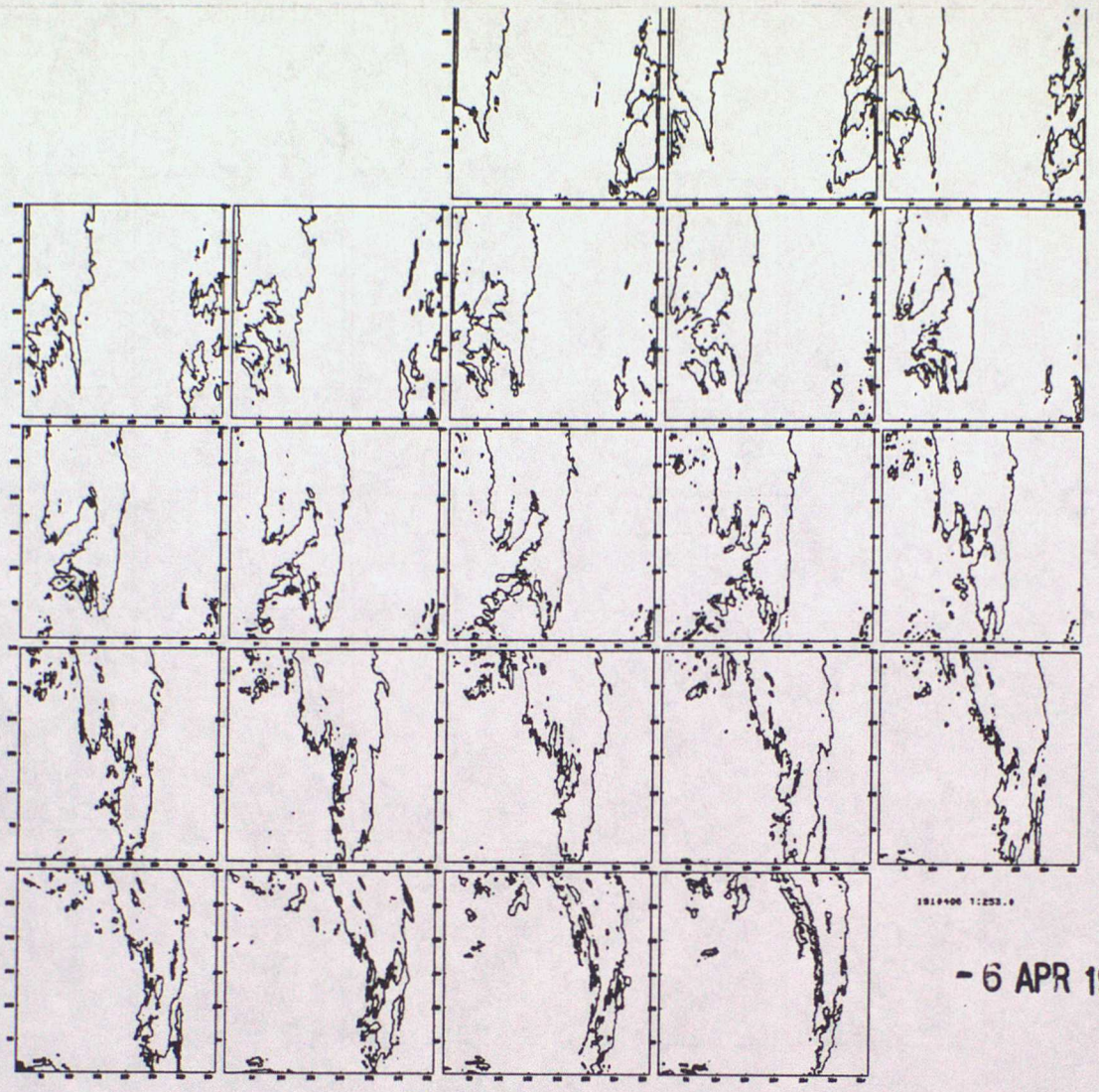


**Fig 11 Continued**

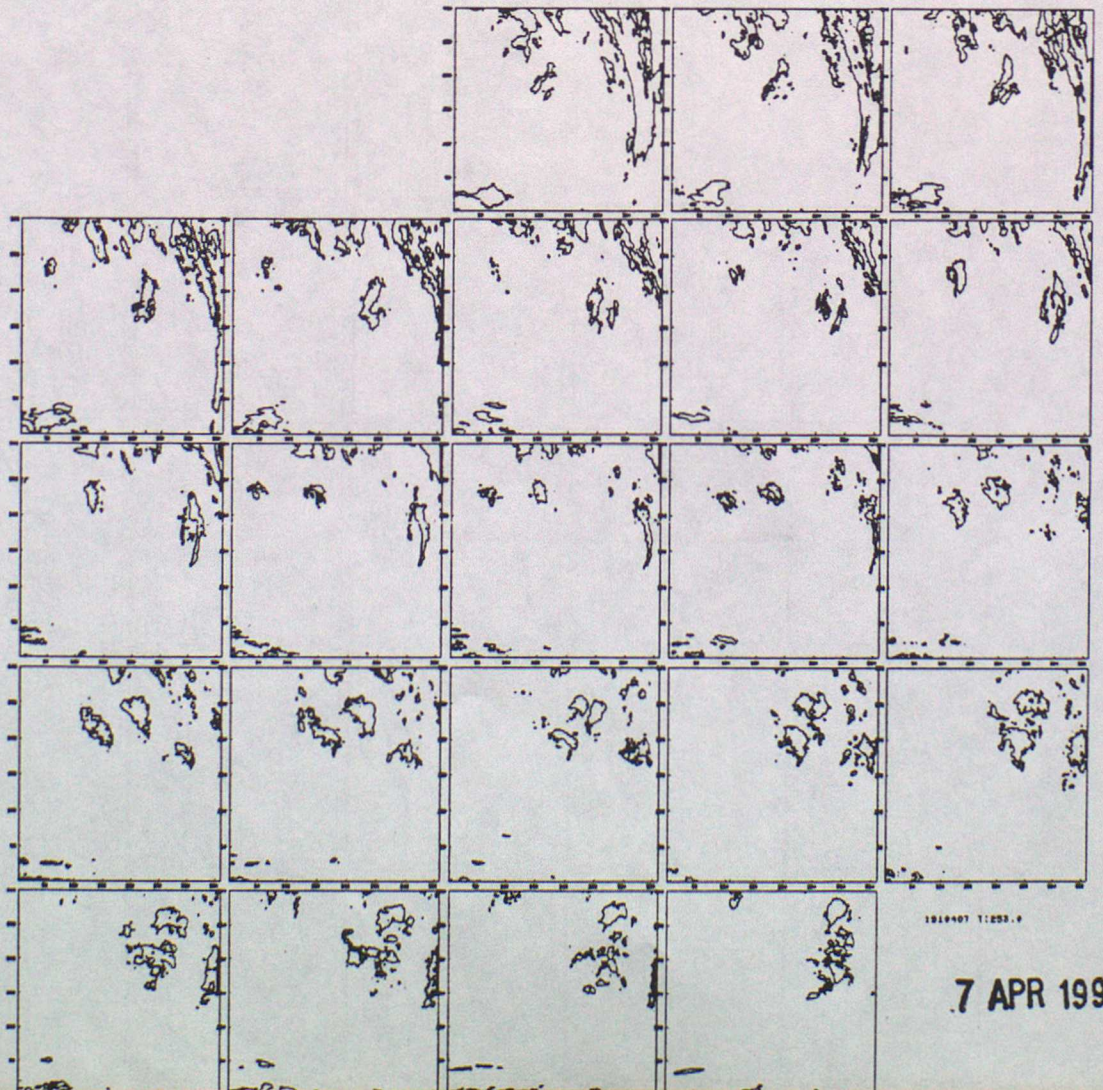

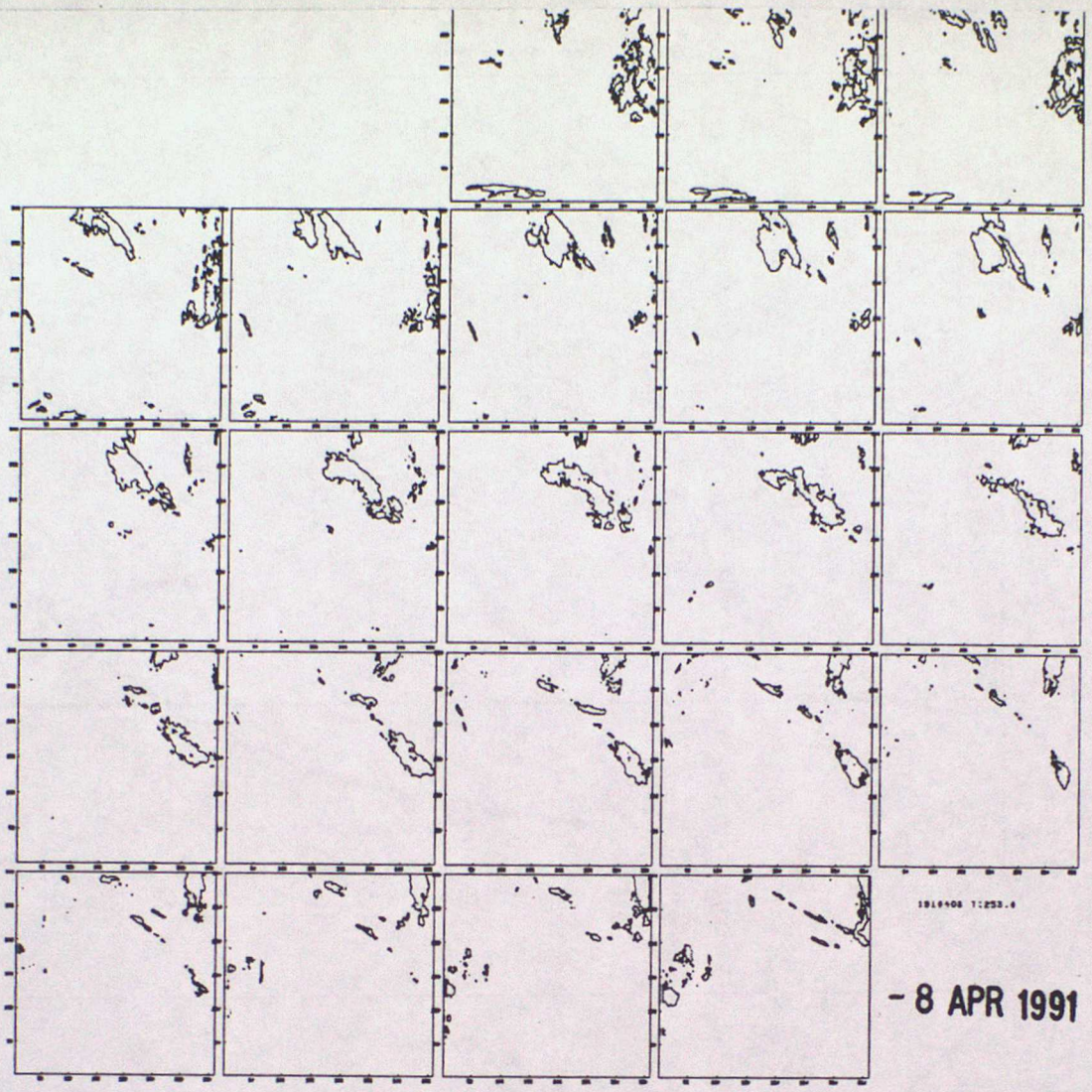


**Fig 11 Continued**

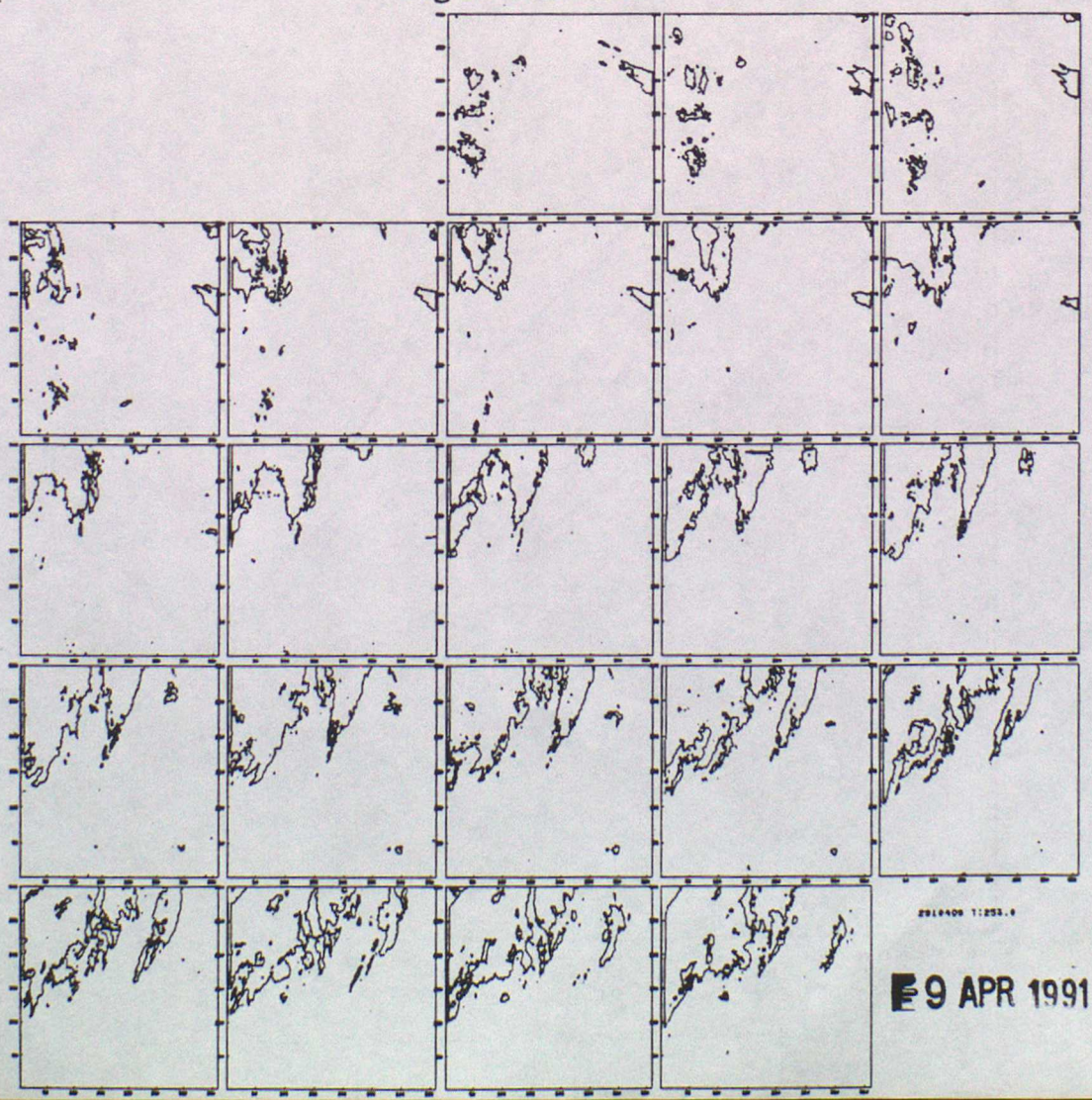

12. IR AND WV CALIBRATION.

A) Correspondence between digital count and brightness temperature for original IR (x), original WV (o) and GPCP-AIP/2 product (+). The IR and WV values were computed using for the MIEC calibration factor respectively a value 0.07 and 0.007; and for the space count respectively 4 and 6.

B) Difference in K (DT) between each digital level for original IR (x), original WV (o) and GPCP-AIP/2 product (+) using the data of panel A.

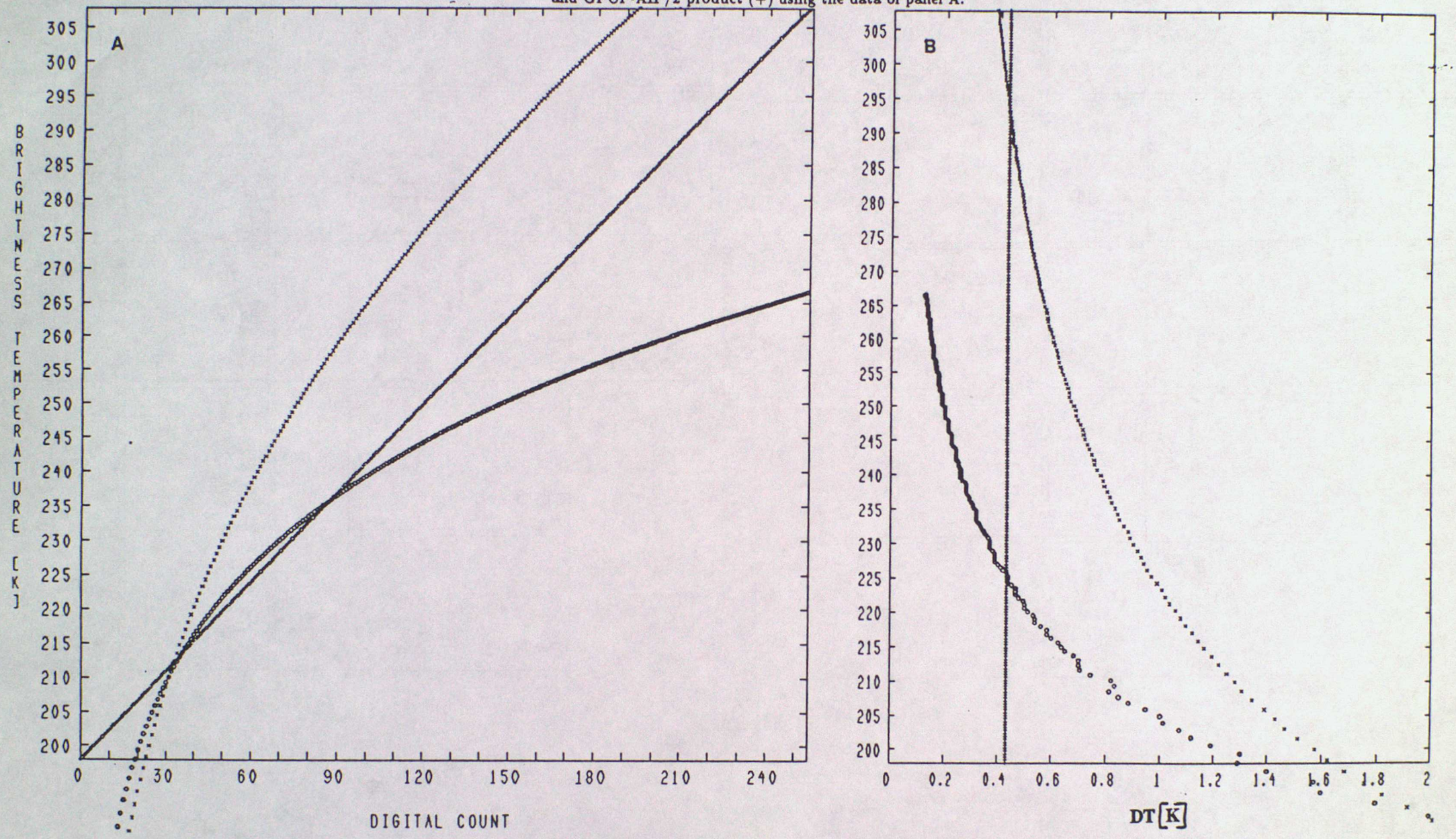

Fig 13. EXAMPLE OF SINGLE LEVEL HISTOGRAM FOR THE DAY 25/03/93. UPPER PANEL IR, LOWER PANEL WV. (The time correspondence is the same as in Fig.10) Note the image for 21:00 is not from Autosat-2. In abscissa are the digital count levels (0-254, thick mark every 50); in ordinate the number of pixels, for each level (0-135000 [12.5 % of total], thick mark every 2000).

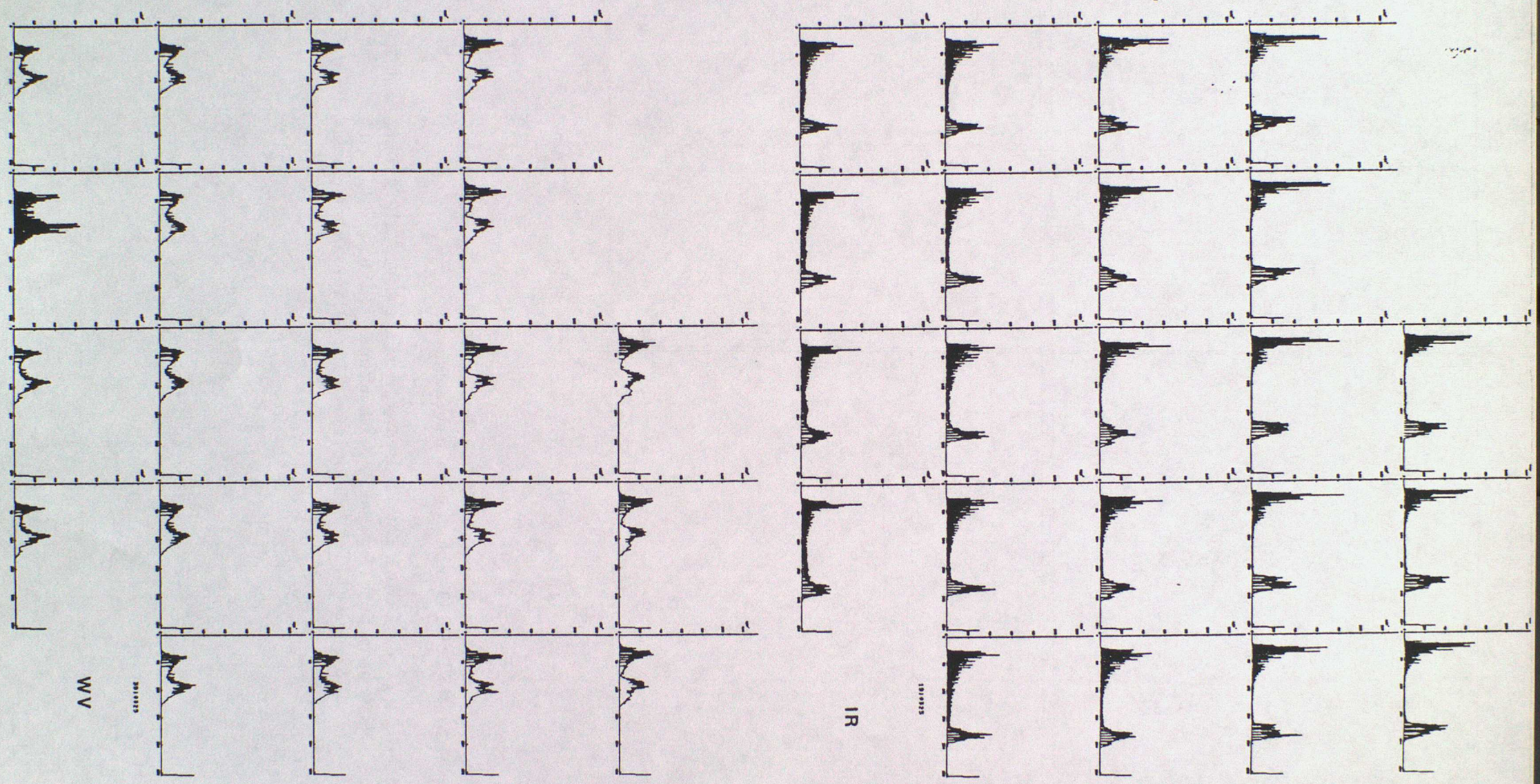

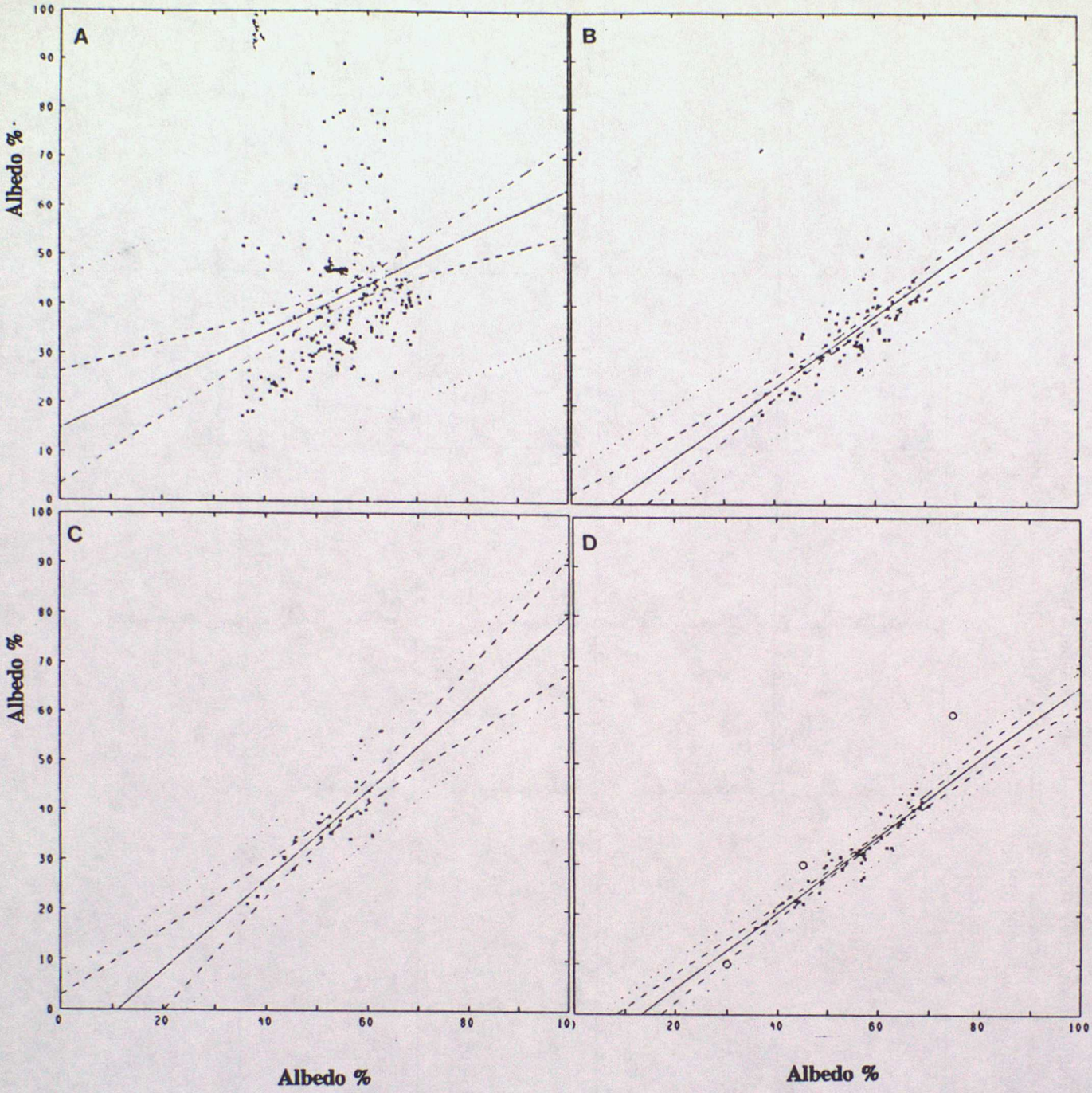


Fig 14. Correlation between AVHRR channel 1 Albedo measurement (ordinate) and "incorrect" METEOSAT VIS measurement (abscissa):
a) All the data;
b) Only AVHRR data with coverage of the GPCP-AIP/2 frame > 90%;
c) Same as (b) for $time \leq 9:00$ or $time \geq 16:00$;
d) Same as (b) for $9:00 < time < 16:00$, the circle represent climatological estimation (see text).